Univerzita Karlova v Praze, Přírodovědecká fakulta
Ústav geochemie, mineralogie a nerostných zdrojů

Charles University in Prague, Faculty of Science
Institute of Geochemistry, Mineralogy and Mineral Resources

Doktorský studijní program: Geologie
Ph.D. study program: Geology

Disertační práce
Ph.D. Thesis

PALEOFLUID CHEMISTRY OF OROGENIC GOLD DEPOSITS: NOVEL
ANALYTICAL METHODS AND CASE STUDIES FROM THE BOHEMIAN MASSIF

Chemismus paleofluid z ložisek typu "orogenic gold":
nové analytické přístupy a případové studie z Českého masívu

Mgr. Tomáš Hrstka

Školitel/Supervisor:

RNDr. Jiří Zachariáš, Ph.D. (Charles University in Prague)

Školitel-konzultant/Supervisor-consultant:

Prof. Jean Dubessy (Université Henri Poincaré, France)
Dr. Richard Harrington (The Natural History Museum, UK)
Dr. Jamie Wilkinson (Imperial College London, UK)

Prague, 2012

Acknowledgements

Statement of originality

The work presented in this thesis is the result of original research carried out by myself, in collaboration with my supervisor and other colleagues stated in text, while enrolled in the Faculty of Science at the Charles University in Prague as a candidate for Doctorate in Philosophy.

To the best of my knowledge and belief, the dissertation contains no material previously published or written by another person except where due reference is made in the dissertation itself. It has not been submitted for any other degree or award in any other university or educational institution.

Prague, 2012

Tomáš Hrstka, MSc.

Statement of co-authors

On behalf of the co-authors, I declare that Tomáš Hrstka was the principal investigator of the scientific study presented in this dissertation and performed majority of the work. The contribution of the co-authors was mainly supplying of the analytical data and critical comments on the final versions of the manuscripts.

Prague, 2012

RNDr. Jiří Zachariáš, Ph.D.

Supervisor

Jiří Zachariáš (Charles University in Prague, Faculty of Science, Institute of Geochemistry, Mineralogy and Mineral Resources, Albertov 6, Praha 2, CZ-128 43)

Consultants

Jean Dubessy (UMR 7566, Géologie et Gestion des Ressources, Minérales et Energétiques, Université Henri Poincaré BP 239, 54506 Vandoeuvre-lès-Nancy)

Richard Herrington (Department of Mineralogy, The Natural History Museum, Cromwell Road London SW75BD, UK)

Jamie Wilkinson (Department of Earth Science & Engineering, Imperial College London, SW7 2AZ, UK)

Funding

Abstract

Fluid inclusions represent a unique tool for understanding the processes leading to the formation of mineral deposits and fluid–rock interactions in general. Orogenic gold deposits in the central part of the Bohemian Massif (Libčice and Kasejovice deposits) were studied in order to provide a better understanding of their genesis. A multifaceted approach was adopted including a broad spectrum of micro-analytical methods.

While traditional methods were used as the basis of this study (e.g., microthermometry, SEM and optical microscopy), the application and improvement/development of modern analytical methods (e.g., LA-ICP-MS and Raman spectroscopy) or introduction of alternative innovative techniques (CLSM, Nano-tomography, QEMSCAN) constituted a significant part of this study.

This study reveals the importance of the HCO_3^- species in hydrothermal fluids (i.e., >100 °C to ~350 °C). Previously, the prevalence of Cl^- and other anions was reported for hydrothermal paleofluids and the majority of studies suggested acidic to neutral rather than the alkaline nature of fluids. This study shows that the presence of bicarbonate ions in some environments is potentially more important than it was previously thought.

Raman spectroscopy appeared to be a promising method for the identification of HCO_3^- species in paleofluids and for the estimation of pH in fluid inclusions containing bicarbonate. This is based on the pH-controlled equilibria of $(HCO_3^-)/(CO_3^{2-})$ where the concentration of the individual species can be deduced from their characteristic Raman peaks at about 1017 cm^{-1} and 1064 cm^{-1}, respectively. Our results suggest the estimated pH of paleofluids at the Libčice gold deposit at pH between 7 and 8.5. Bicarbonate-rich paleofluids were recorded for the first time by direct HCO_3^- measurement by Raman spectroscopy in an orogenic gold environment.

This thesis also stresses the role of post-entrapment modification of fluid inclusions properties due to thermal, pressure and chemical gradients associated with contact metamorphism. The role of H_2 diffusion into the inclusions was proved and the dependence of diffusion processes duration on temperature was modeled. The diffusion of H_2 through the quartz host was demonstrated as a key factor for the observed intra-grain CO_2/CH_4 zoning in fluid inclusions from the Libčice gold deposit.

It was found that the complex interaction of local lithologies and paleofluids played an important role in the formation of unusually bicarbonate-rich paleofluids containing nahcolite, H_2 (up to 6 mol%) and ethane (up to 0.2 mol%). The presence of organic matter-bearing sediments in combination with the thermal impact of the intrusion of granitoids of the Central Bohemian Plutonic Complex are considered key factors in the formation of the observed variability in paleofluid composition.

Finally, it is demonstrated that fluid chemistry can be reliably determined by the combination of analytical methods and thermodynamic modeling. CLSM and X-ray nano-tomography were shown to be promising techniques for future efforts in single fluid inclusion volume and 3D shape reconstructions. QEMSCAN technology was proved to provide invaluable automated quantitative mineralogical and petrological data.

Abstrakt

Fluidní inkluze představují jedinečný nástroj pro pochopení procesů, které vedou ke vzniku ložisek nerostných surovin, a interakcí mezi horninovým prostředím a fluidy obecně. Ložiska typu „Orogenic Gold" v centrální části Českého masívu byla studována za účelem lépšího porozumění jejich genezi. Byl použit mnohostranný přístup zahrnující široké spektrum mikro-analytických metod. Zatímco běžné metody byly použity jako základ v této studii (např. mikrotermometrie, SEM a optická mikroskopie), zlepšení či rozvoj moderních analytických metod (např. LA-ICP-MS a Ramanova spektroskopie) a zavedení nových alternativních technik (CLSM, Nano-tomografie, QEMSCAN) tvoří významnou část této studie.

Tato práce ukázala na význam HCO_3^- v hydrotermálních fluidech (tj. >100 °C až ~350 °C). Až do teď, převaha Cl^- či výskyt dalších podobných aniontů byly zaznamenány v hydrotermálních paleofluidech. Stejně tak většina předchozích studií prokázala kyselou až neutrální spíše než zásaditou povahu paleofluid. Přítomnost iontů bikarbonátu v některých prostředích je tudíž potenciálně mnohem významnější, než se dříve předpokládalo.

Ramanova spektroskopie se ukázala jako slibná metoda pro stanovení HCO_3^- v paleofluidech a pro odhad pH ve fluidních inkluzích, které obsahují hydrogenuhličitan. Toto stanovení je založeno na pH-kontrolované rovnováze mezi $(HCO_3^-)/(CO_3^{2-})$, kde koncentrace jednotlivých iontů mohou být odvozeny z jejich charakteristických Ramanových pásů (1017 cm^{-1} a 1064 cm^{-1}). Naše výsledky ukazují na hodnoty pH paleofluid na ložisku zlata Libčice mezi pH 7 až pH 8,5. Bikarbonátem bohatá přírodní paleofluida byla identifikována přímým stanovením HCO_3^- pomocí Ramanovy spektroskopie ve fluidních inkluzích. Jedná se o prvou identifikaci tohoto aniontu v prostředí odpovídajícím tvorbě ložisek typu Orogenic Gold.

Tato práce zdůraznila také úlohu procesů probíhajících po zachycení inkluzí při modifikaci jejich vlastností vlivem tepelných, tlakových a chemických gradientů spojených s kontaktní metamorfózou. Byla prokázána úloha difúze H_2 směrem dovnitř inkluzí a zároveň byla modelována závislost trvání tohoto difúzního procesů na teplotě. Difúze H_2 v křemeni byla prokázána jako klíčový faktor ovlivnující zonalitu poměrů CO_2/CH_4 pozorovanou ve fluidních inkluzích uvnitř jednotlivých zrn křemene na ložisku Libčice.

Komplexní interakce místních lithologií a paleofluid hrála důležitou roli při formování neobvykle bikarbonátem bohatých paleofluid s nahcolitem, H_2 (až 6 mol%) a ethanem (0-0,2 mol%). Přítomnost organických látek v okolních sedimentech v kombinaci s tepelným vlivem intruze granitoidů středočeského plutonického komplexu jsou považovány za klíčové faktory při vzniku zjištěných variací ve složení paleofluid.

V neposlední řadě bylo prokázáno, že je možné spolehlivě určit chemizmus paleofluid za použití kombinace analytických metod a termodynamického modelování. Naše výsledky ukazují na použitelnost konfokální mikroskopie a rentgenové nano-tomografie jako technologií umožnujících přesnou 3D rekonstrukci fluidních inkluzí a stanovení jejich objemu. Bylo prokázáno, že automatizované metody jako QEMSCAN poskytují neocenitelná data pro kvantitativní mineralogii a petrologii.

Table of Contents

List of Tables

List of Figures

1. INTRODUCTION

Our current effort towards a better understanding of fluid–rock interaction and the genesis of ore deposits goes hand in hand with the frontier development of analytical techniques and instruments. This study presents the results of combined multidisciplinary approach on understanding of paleofluid evolution at selected Czech gold deposits. It also focuses on the application and development of novel micro-analytical techniques applied in fluid inclusion research. Quantitative and qualitative Raman spectroscopy, Confocal Laser Scanning Microscopy (CLSM), 3D Nano-tomography, various electron scanning microscope-based techniques (CL-SEM, SEM-EDS, QEMSCAN), LA-ICP-MS, optical microscopy and microthermometry were all integrated to provide a better understanding of the complex history of paleofluids at several gold deposits in the central part of the Bohemian Massif (the Libčice, Kasejovice and Roudný deposits). This work contains numerous novel observations and interpretations and provides an example of thermal overprinting of an orogenic gold deposit system with attendant mobilization of wall-rock components and chemical modification of pre-existing fluid inclusions. This study is of relevance not only to geochemists who study orogenic gold deposits but to everyone interested in water–rock interactions at elevated temperatures.

1.1 Gold Deposits in Metamorphic Terrenes - An Introduction

Gold deposits in metamorphic terrains (most of them are classified as orogenic gold deposits) represent an important source of gold metal. Globally they include well known examples from Precambrian shields (~24 000t Au) as well as Neoproterozoic and younger Cordillieran-style orogens (~22 000t load and ~15 500 t placer Au). Ore formation has a time span of 2.8 to 2.55 Ga, 2.1 to 1.8 Ga, and 600 to 50 Ma, respectively (e.g., Goldfarb et al., 2005; Goldfarb et al., 2001; Groves et al., 1998; Phillips, 2009). Most of these deposits are believed to formed synchronously with the late stage of orogeny and that is why they became classified as "orogenic gold deposits". Based on the pressure and temperature conditions in which they have formed they can be further subdivided into epizonal (<6 km), mesozonal (6-12 km), and hypozonal (>12 km) subtypes. A second important type of gold deposits in metamorphic terrains is termed intrusion-related gold deposits. These are characterized by intimate genetic association with mostly granite intrusions (e.g., Goldfarb et al., 2005; Lang and Baker, 2001 and reference therein).

Orogenic gold deposits are located on, or adjacent to, deep-crustal faults which extend over large distances (100 km) having widths of as much as a few thousand meters. Subduction-related thermal events are expected to rise the thermal gradient and drive the relatively huge hydrothermal cells (e.g., 100 km by 10 km in area and 30 km in depths for the French Massif Central; Bouchot et al., 2005) for a long periosd of time. Also the pressure fluctuation and fluid migration along fault zones related to major seismic events played an important part in the formation of ore as a vein fill

in the second and third-order deep-crustal fault zone. Depending on the geological settings, the mineralization styles vary significantly from breccias and stockworks in shallow regimes through laminated crack-seal veins in brittle–ductile crustal regions, to replacement- and disseminated-type deposits in deeper ductile settings. While the dominant portion of orogenic style deposits are hosted in the greenschist facies, examples of lower and higher degree of metamorphism have been also encountered.

From the viewpoint of paleofluid chemistry these deposits are usually associated with CO_2 -rich or H_2O-CO_2 -rich fluids with relatively low salinities. Examples with significant admixture of N_2 or CH_4 have been also reported in the literature (Goldfarb et al., 2005). The exact origin of such compositional variations is still controversial as well as the exact origin of fluids responsible for metal transport and precipitation of gold in orogenic gold deposits. Different origins including metamorphic, magmatic and meteoric fluids have been widely discussed in the literature (Figure 1.1).
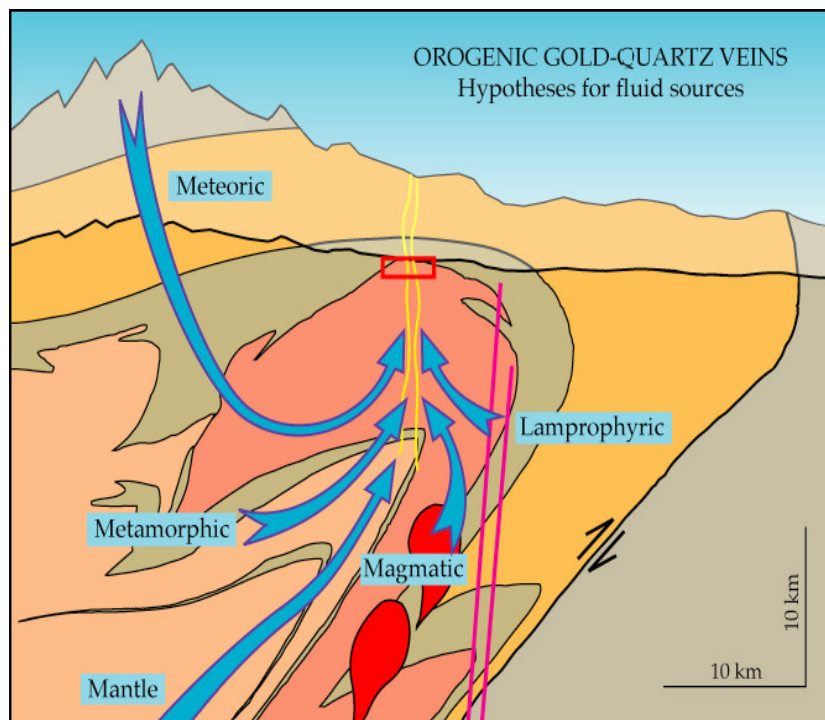
Figure 1.1: Schematic presentation of various types of fluids involved in the genesis of orogenic gold deposits (Pettke et al., 2000).

Mineralogies of orogenic and intrusion-related gold deposits are similar, being usually represented by low amounts of base metal sulfides (<2-5 and <15 vol. percent of sulfides for intrusion-related and orogenic gold deposits, respectively). Arsenopyrite and pyrite are the most common sulfides. For deposits formed at higher temperatures, pyrrhotite is more important. Bi, Bi-Te and W-bearing

phases can be often found associated with relatively sulfide-poor (intrusion-related) gold deposits. The alteration assemblages vary with the host rock but usually include carbonates, sulfides, chlorite, micas, albite, K-feldspar and tourmaline.

1.2   Gold Deposits in the Central Part of the Bohemian Massif

Orogenic gold deposits are a typical feature of the Variscan Europe. They are known from Massif Central, Armorican, Iberian and Bohemian Massifs. Based on mineralogical criteria (Bernard and Pouba, 1983), three major groups of hydrothermal quartz vein-stockwork gold deposits can be distinguished in the central part of the Bohemian Massif: (1) deposits with gold of high fineness (> 900), commonly accompanied by scheelite, minor molybdenite and accessory Bi-Te-S phases (e.g., Jílové, Mokrsko, Kasejovice, Kašperské Hory deposits); (2) deposits of high-fineness gold (> 900), accompanied by abundant Sb-mineralization (stibnite, aurostibite, Pb-Sb-sulphosalts; the Krásná Hora deposit); (3) deposits with gold of lower fineness (< 700, i.e., electrum) and lacking W-Mo-Bi-Te-S phases (e.g. Roudný and Dobrá Voda deps., Zachariáš et al., 2009a).

Most deposits/mineralizations along the northwestern margin of the CBPC belong to the first group and can be classified as typical orogenic gold deposits (e.g. Goldfarb et al., 2001), of which the Kašperské Hory deposit (Ďurišová – et al., 1995) and the studied Jílové deposit (e.g. Morávek, 1971; Morávek, 1995c) are the best examples. Few other deposits (the Mokrsko dep., Boiron et al., 2001 and the Petráčkova Hora dep., Zachariáš et al., 2001) can be classified as a reduced-type of intrusion-related gold deposits, or as an intermediate type between orogenic and intrusion-related gold types. Dating of some of the group (1) gold-deposits by Re-Os method (molybdenite; Zachariáš and Stein, 2001; Zachariáš et al., 2001) documented formation of gold mineralization within a narrow span of 10 Ma, from 349 to 339 Ma. Gold mineralization thus significantly overlaps with intrusive ages obtained for the CBPC (355–335 Ma for main phases).

The Jílové, Kasejovice, Libčice and the Krásná Hora deposits were mined extensively in the 13th – 14th centuries; and intermittently until the end of the 20th century. The Mokrsko and Čelina deposits (Morávek et al., 1989) and Petráčkova hora deposit (Zachariáš et al., 2001) were discovered and explored during 1980–1990. Total resources of the CBMZ are estimated at ~180 t of gold, of which Mokrsko and Čelina deposit contain ~ 130 t, Jílové deposit 10 t and Petráčkova hora 30 t.

1.3   Introduction to Fluid Inclusions Studies

Fluid inclusions as relicts of paleofluids trapped inside minerals during their formation/growth (primary inclusions) or during later events postdating the mineral crystallization (secondary inclusions) represent a unique insight to the conditions which ruled the formation of individual mineral assemblages. Their understanding can give us detailed information on P-T-X conditions

and on processes responsible for the formation of different ore deposits (e.g., Samson et al., eds. 2003; De Vivo and Frezzotti, 1995; Roedder, 1984; Wilkinson, 2001).

During the past decade a significant progress in the development of experimental and analytical methods has been made in order to help such effort (e.g., Timofeeff, M.N., 2000; Samson et al., eds. 2003; Kurosawa et al., 2003[a,b]; Hanley et al., 2005; Azbej et al., 2007 and Kurosawa et al., 2008).

Before the study of the inclusions by advanced analytical techniques, careful microthermometric and microscopic studies are necessary. Three different classification approaches are usually combined: genetic classification (e.g., Roedder, 1984; based on temporal relationships between inclusions and hosting mineral), descriptive classification (based on the number and volume relationship of the phases present; e.g. Shepherd et al., 1985) and a concept of fluid inclusion assemblages (FIA; Goldstein and Raynolds, 1994).

The concept of FIA provides excellent means to classify inclusions where the temporal classification proves difficult. FIA represents a group of inclusions which were trapped at the same time and thus in the approximately same temperature and pressure. The individual FIA can be discriminated based on petrography (Goldstein, 2003) and represent individual "fluid events"

There are three basic assumptions necessary in the interpretation of fluid inclusions. These are known as "Roedder's Rules" and state that: 1) the inclusion trapped a single, homogeneous phase; 2) the inclusions represent a constant volume (isochoric) system; and 3) after entrapment, nothing has been added or removed from the inclusions. These assumptions might be tested by petrographic and microthermometic observations.

These conditions are not always met, but where any exceptions are recognized, data can be also interpreted and important information is obtained on the processes of paleofluid circulation and evolution.

1.4   Paleofluids in Orogenic Gold Deposit Systems

Many publications/researchers have almost universally identified mixed aqueous carbonic fluids in gold-bearing quartz, generally of low salinity, which, in most cases, are the suggested ore-bearing fluids (Groves, 1993; Goldfarb et al., 2005; Goldfarb 2000 in Hedenquist eds; Ridley and Diamond, 2000). Variable contents of H_2O and CO_2 have been reported among different provinces and even within the same ore district. Most of the deposits show a mixed signature ranging between 4 to 30 mol percent CO_2. In many cases where the CO_2 concentration is higher (up to > 95 mol. %), the possibility of fluid un-mixing has been quoted as a potential mechanism of the generation of CO_2 -rich fluids. Fluid un-mixing represents also potential mechanism for gold precipitation (Goldfarb et al., 1993). Deposits with lower CO_2 content generally correspond to the

lower temperature examples / members of the group (250–350 °C) while CO_2 -rich fluids are more typical for higher temperatures (325–400 °C). Fluids more rich in CO_2 have been also reported from higher-grade metamorphic terrains.

Gases as CH_4, N_2 and H_2S are often reported as additional volatile species in fluid inclusions from gold-bearing veins. Their concentrations range widely from a few percent to 50 %, although the concentrations of combined N_2 and CH_4 are below 5 mol. percent in most Phanerozoic gold deposits in metamorphic terranes. The presence of these gases has been attributed to the interaction of the fluids with the surrounding rocks.

Approximate equilibrium with the host rock sequence but not with the immediate wall rock is typical. Evidence has been found that the fluid composition evolved both in time and space in many orogenic gold deposits. Based on the current knowledge, both granitoid magmatic and metamorphic devolatization models are available as a fluid source (Ridley and Diamond, 2000).

Precipitation of gold is attributed to the fluid–wall-rock reaction, changes in pH and/or fo_2 . Pressure fluctuations, especially for quartz vein-hosted orebodies, provide another important control on gold deposition (Sibson et al., 1988; Loucks and Mavrogenes, 1999). Fluid unmixing of a parental CO_2-H_2O fluid might be also an important factor in localizing high-grade ore shoots (Groves and Foster, 1991).

1.5   Volume Reconstruction for Complex Fluid Inclusions

Chemical composition and V-x properities of paleofluids provide a unique insight into the Earth interior (Wilkinson, 2001). Chemical composition and molar volume of aqueous-electrolyte fluid inclusions and gas-bearing inclusions can be calculated based on the microthermometric and other analytical data. However, for the complex multi-volatile salt-bearing systems with appreciable amount of CO_2, CH_4, H_2S, N_2 or other gases, the input of volume-fractions (φ) is necessary. This is because the available equations of state for elevated P-T conditions are unable to link accurately high-T microthermometric data with low-temperature observations. Due to this fact the calculation of bulk properties of complex fluids still relies on *inaccurate estimates of* volume-fractions (φ) of phases present within the inclusions based on optical microscopy (Bakker and Diamond, 2006; Diamond, 2003a; Diamond, 2003b).

The use of a spindle stage has been investigated (Anderson and Bodnar, 1993; Bakker and Diamond, 2006) to improve the accuracy of (φ) values. This method provides good success with regular inclusions but the accuracy on the volume fraction calculations is still limited for irregularly shaped inclusions even with the labor intensive spindle-stage method. Although the application of the CLSM fluorescent mode has been tested for the oil-bearing ("fluorescent") inclusions (e.g., Aplin et al., 1999; Thiery et al., 2000), the application of this technique in a reflected mode or nikopf configuration has not been reported in the literature in detail. As a part of

this project the application of CLSM in 3D volume reconstruction and volume estimates in aqueous paleofluids were tested and our results are presented in Chapter 2.6, and Appendix A.3. Inclusion volume can be also visualized *via* X-ray based methods, like nano-CT or CT techniques. The application of the nano-CT in 3D inclusion volume reconstruction was demonstrated by the author of this thesis and is presented in Chapter 2.7 and Chapter 7 .

1.6   Processes Responsible for Paleofluid Compositional Variations

Significant variations in paleofluid composition (e.g., presence of aqueous-carbonic and/or carbonic inclusions, or variations in the CH_4/CO_2 ratio) at the individual orogenic gold deposit were already quoted at many localities/terrains worldwide.

Such variations, if interpreted correctly, could provide us with the understanding of fluid–rock interaction as well as processes leading to ore genesis in a broader sense. They can reflect primary processes in a fluid phase before its entrapment in fluid inclusions, or secondary processes after its entrapment.

Potential primary processes responsible for these variations include: 1) complex hydrothermal history where different fluids passed through the vein under different condition (e.g., Mernagh et al., 2004); 2) large fluctuations of pressure (e.g., Robert et al., 1995; Zachariáš, 2002); 3) generation of CH_4 *via* interaction of aqueous fluids with graphite-bearing rocks at high temperatures (e.g., Huff and Nabelek, 2007); 4) partitioning of CH_4 into gaseous phase during boiling of a parent H_2O-CO_2-CH_4 fluid (e.g., Klein et al., 2000; Mernagh and Witt, 1994); and 5) fluid mixing between two or more fluids accompanied by fluid immiscibility (e.g., Diamond, 2001; Jia et al., 2000; Loucks, 2000; Yao et al., 2001; Zoheir et al., 2008).

Apart from the primary processes, significant compositional variations can also be produced by post-entrapment re-equilibration/modification of the original inclusions (e.g., Mavrogenes and Bodnar, 1994; Morgan et al., 1993; Ridley and Hagemann, 1999). Re-equilibration is a phenomenon which can occur either naturally or can be induced during an experimental procedure (e.g., Diamond et al., 2010; Tarantola et al., 2010; Bakker, 2009). Changing of geological conditions like burial of a geological sequence or its uplift is an example of the natural causes while sample preparation or interaction of fluid inclusions with sources of visible and invisible radiation is an example of artificial changes in fluid inclusions volume and/or chemistry caused. Under re-equilibration, we generally understand changes in the original chemical composition, speciation or density.

As a result of numerous studies of both synthetic and natural samples containing fluid and melt inclusions (e.g., Morgan et al., 1993; Mavrogenes and Bodnar, 1994; and Sterner, 1995; Bakker and Jansen, 1991, 1994; Sterner et al., 1995) we now have a relatively good understanding of different ways of re-equilibration processes. These processes can be generalized as:

- Stretching (involving a change in volume of fluid inclusion void)

- Leakage/partial decrepitation (manifested by escape of some components from fluid inclusion *via* microcracks)

- Diffusion (movement of compounds in, or out of, the inclusions when the host mineral does not fulfill its role as an impermeable barrier)

Systematic variations in CO_2/CH_4 ratio have been reported from the Libčice gold deposit (Zachariáš et al., 1997; Zachariáš, 2002). The author of this thesis continued in this research with the application of modern analytical techniques. The observed compositional variations and processes responsible for their occurrence are thoroughly discussed in the Chapter 3 (article 1).

1.7   Analytical Methods in Fluid Inclusion Research

Understanding the paleofluid composition and prosperities is a crucial prerequisite to interpret the formation of many types of ore deposits and fluid–rock interaction processes in general. There is a huge number of analytical techniques available to fluid inclusion research (e.g., reviews of Boiron and Dubessy, 1995).

The principal method used in the fluid inclusion research which should be used together with any "advanced" microanalytical techniques is microthermometry. This basic technique provides data on fluid composition (bulk salinity, fluid density, presence/absence of gases), and also constrains on the temperature and pressure of entrapment of the individual fluids. It is based on observation of phase equilibria at various temperatures using the heating/freezeing microscopic stage (usually in the interval of -180 to +600 °C). The limitation of this technique is mainly the inability to provide data on trace elements in fluid inclusions and interpretation of complex (multivolatile salt-bearing aqueous systems) paleofluid systems. Methods, principals and applications of microthermometry has been described in detail in many publications (e.g., Roedder, 1984; de Vivio and Frezzotti eds., 1995; Samson et al., eds 2003 and others).

For trace element information or for advanced thermodynamic modeling of the complex systems, a combination of microthermometric data with other techniques is necessary.

Analytical techniques used in fluid inclusion research can be divided to "bulk analysis" and "single analysis" methods. The "single analysis" methods can be further divided/grouped as destructive and nondestructive.

The "single analysis" methods focus on analyzing of individual fluid inclusion. These include for instance: Fluorescence spectroscopy (cit); Raman spectroscopy (Burke 2001); MICRO FTIR; SEM/Kryo-EDS (CIT); PIXE (Proton Induced X-ray Emission); PIGE (Proton Induced Gamma-

ray Emission); SXRF (Synchrotron X-ray Fluorescence); LA-ICP-MS (Laser Ablation Inductively Coupled Plasma Mass Spectrometry)

 The "bulk analysis" methods use crash-leach approach from high number of inclusions. They relay on extracting sufficient volume of the fluid phase from a high number of inclusions. This can be performed either by milling in a vacuum mill or by thermal decrepitation of a sample containing a high population of fluid inclusions. Such sample (analyte) can be used in many common analytical techniques including mass spectroscopy (MS), chromatography (GC) and other methods. The drawback of these techniques is the inability to separate the individual fluid inclusion assemblages present within the sample, leading thus to the production of mixed data (representing all the populations of paleofluids present within the sample).

The methods applied in this study are described in detail in Chapter 2. Novel techniques and their developments forming a part of the original research by the author are presented separately in Chapters 4 and 7.

1.8   Thesis Outline

The presented thesis is intended to a) provide data on genesis of selected gold deposits in the Bohemian Massif; and b) develop methods applicable to the study of complex paleofluids in general.

In order to accomplish the aims, the project focused on compositional variations in early quartz-sulfide-bearing fluids associated with gold mineralization at deposits where the genetic models and P-T-X conditions were still missing or were poorly defined (Libčice, Roudný and Kasejovice deposits).

As we were facing an extremely complex fluid chemistry, we also focused on the development and improvements in the analytical techniques used for fluid inclusion research in general. These included original research and development in:

1. Qualitative and quantitative Raman spectroscopy of bicarbonate-rich inclusions and strategies for potential pH calculation of HCO_3^--bearing paleofluids.
2. QEMSCAN analysis for fast automated search for low-density phases in fine-grained rocks.
3. CLSM and 3D Nano-tomography for exact volume calculation and 3D reconstructions of fluid inclusions.
4. LA-ICP-MS analysis of single inclusions (ExLAM software development).

The majority of our attention was focused on Libčice gold deposit which represents an unique system with preserved relationships between the mineralization and thermal aureola of CBPC.

Using fluid inclusion microthermometry and micro-Raman spectroscopy we managed to decipher compositional variations (namely CO_2/CH_4 and H_2O/CO_2 ratios) in the early vein-forming fluids (i.e. associated with quartz and early sulfides). In contrast to previous studies, where mostly the central parts of the deposit were studied only, we have focused on complete sampling profiles that has contained both the peripheral and core zones of the gold deposit as well as the most out-laying manifestations of quartz-gold mineralization in this region.

The orientation of sampling profiles – perpendicularly to the strike of the CBPC – has allowed us to decipher the role of local fluids/processes (host rock lithology, contact-metamorphic processes, organic matter) from that of large-scale provenience (deep metamorphic or magmatic fluids). This strategy was based on our preliminary sampling that indicated that significant variations in CO_2/CH_4 ratios exist both on deposit and on regional scales. No similar study has been done in this area yet.

2. METHODS AND INSTRUMENTATION

This section provides an overview of analytical methods and procedures used in this thesis. Apart from techniques which nowadays become more and more common in the analysis of complex paleofluids and are addressed only as brief introductions, several new methods and optimization strategies has been developed and tested as a part of this work. Some of these developments were published and are presented separately (Chapters 4 and 7) in more detail.

2.1 Microthermometry

Microthermometry represents the main technique available the fluid inclusion research. It is based on the observation of phase transition in these closed systems during cooling and heating runs in specially equipped petrographic microscope. From the phase equilibria and thermodynamic modeling we are able to obtain information about expected minimal temperature of entrapment as well constraints on pressure during formation and paleofluid chemical composition. The detail of information depends highly on the complexity of the studied system and the availability of experimental data. For detail information on this well established technique the reader is referred to excellent reviews by (e.g. Roedder, 1984; Diamond, 1994 and 2001; Samson et al., eds. 2003 and others). Microthermometry was performed on samples from the selected gold deposits and the detail methodology and instrumentation is presented in individual chapters.

2.2 Raman Spectroscopy

A brief introduction to the application of Raman spectroscopy for the study of fluid inclusions is given. This includes the proposed instrument parameters for the successful measurements based on the experience performed by the author at Nancy G2R Lab France, Kingston University London and Charles University in Prague. This chapter is intended also as a guide to fluid inclusion Raman analysis for our department at Charles University in Prague or other laboratories starting on the field of fluid inclusion Raman analysis. Spectra descriptions for most abundant phases found in fluid inclusions and the equations and constants such as (Sigma, Efficiency) necessary for quantitative Raman gas measurements are also provided and discussed briefly. For more detailed information on the Raman spectroscopy in fluid inclusion research reader is referred to some of the brilliant reviews (e.g. by Burke, 2001 and Burruss, 2003) and references therein.

Raman spectroscopy is one of the most important analytical methods used in fluid inclusion research (Burke, 2001; Burruss, 2003; Bakker, 2004; Chen et al., 2004). One of its main advantages is the ability to analyze non-destructively the structural and chemical nature of the sample on a very small scale (~1μm). Its application is in the identification of solid phases within fluid inclusions, qualitative and quantitative determination of gas content (Dubessy et al., 1989;

Wopenka and Pasteris, 1986), for identification of gas hydrates and salinity determinations in low temperature measurements (e.g. Mernagh and Wilde, 1989; Dubessy et al., 2002; Baumgartner and Bakker, 2009), for study of polyatomic ions in solutions (Boiron et al., 1999; Dubessy et al., 1983; Rosasco and Roedder, 1979) or for determination of homogenization temperatures in gass-rich inclusions with thin water film on the inclusion wall (Burke, 2001; Burruss, 2003; Bakker, 2004; Chen et al., 2004).

Quantitative calculations of the concentration of Raman active ions such as: CO_3^{2-}; HCO_3^-; SO_4^{2-}; PO_4^{3-}; HS^-, can lead us to important information about pH, fO_2, fS_2 fugacity as well as other parameters of the paleofluid (Dubessy et al., 1989, Dubessy et al., 1983).

2.2.1 Instrumentation and basic concepts

Instrument parameters for fluid inclusion analysis

Qualitative and quantitative Laser Raman microspectrometry (LRM) analysis was performed mainly at G2R Laboratory Nancy using a Labram Dilor Jobin Yvon (300 mm focal length; 1800 groove/mm grating) model, while excitation radiation provided by the Ar^+ spectral physic laser was 514,532nm. High temperature LRM measurements were carried out by accompanying the instrument with LINKAM heating-freezing stage. The spectra treatment as baseline correction, peak picking, subtraction and curve fitting was conducted by WiRE2 software and Thermo Galactic software package.

- Laser 514,53nm; 200mW
- Pin hole 300-400
- Slit 250-300um
- Grating 1800
- Time 60-300s (expected signal intensities 5000-50000 (2/3 of instrument magnitude potential)
- Accumulations 2-6
- Objective 40-60-80-100x long working (potentially with cover glass corrected)

Spectrum acquisition

Usually two modes are possible for the spectrum acquisition; "spectral windows" or "continuous spectrum" (whole spectrum acquisition). In our measurements, the first option is more common where we select the spectral window of our interest which could be imagined at once (typically about 1600 cm^{-1} width). Potential windows are for example: in gas (CO_2 - 930-2530 cm^{-1}) (CH_4 2000-2600 cm^{-1}), N_2 and Air (940-2500 cm^{-1}) H_2O (2520-3850 cm^{-1}) etc. The exact extent and number of windows selection depends on the peaks of our interest and the available time. This type

of measurements is also useful if the intensities at different regions are very variable. Then we can select the longer time and more accumulations (ac) for minor compounds and shorter time and ac for major species avoiding the saturation of detector.

Focusing on inclusion

Focusing on inclusion is usually done by measuring the spectral window of liquid water with a few sec acquisition time while we are trying to obtain the best signal to noise ratio. Then we can move around the inclusion inspecting the different phases at the approximately same depth.

Visual focusing by imaging of the laser beam on the phase boundaries inside the inclusion is also possible but with difficulties.

Note that the reference matrix spectra of quartz (for subtraction of peaks) and the spectra for N_2 contribution from air need to be taken from exactly the same depth as the spectra of interest (N_2 gas in inclusion etc.). The same acquisition time is required as well. Extreme care needs to be taken when obtaining quartz matrix spectra because there is a reported high variation in Raman intensity peak ratios dependent on crystal orientation and possibly also the deformation and other defects in the quartz crystals (e.g. Chapter 4 and reference therein) . It is recommended to collect more than one spectra from a close vicinity (must be within the same grain!) of a studied inclusion if any quantitative work in this region of interest is expected.

Spectral processing (baseline correction and spectral math)

There are no strict rules on the baseline correction and background subtraction which could be applied to all Raman spectra. The spectral processing depends on the spectra quality and the questions asked/purpose of analysis. Generally speaking, each correction includes some assumptions which could introduce errors to spectra interpretation.

For matrix subtraction a peak which is present only in the matrix could be used to establish a coefficient of subtraction but a small artifacts (negative Raman intensity values) are often formed (due to the difference in background noise and other factors). If the shape of the spectral curve follows the same trend it is advisable to subtract the spectra before baseline correction (Němec, 2009; personal communication).

In an ideal case, matrix spectra should be obtained from exactly the same depth within the samples and with exactly the same instrument parameters (time/ac etc.).

As we are usually working with peak ratios rather than with absolute values, baseline correction is not always necessary in inclusion analysis. An exception is a subtraction of overlapping

components/matrix where baseline correction might be necessary. Care also needs to be taken if peak shapes/width are changing (e.g. temperature shift, composition shift or salt increase) while comparing results from multiple inclusion populations!

Automatic baseline correction could be easier if we are processing high number of spectra but this process requires manual crosscheck.

2.2.2   *Relative molar fraction calculations in mixtures of gases*

Characteristic Raman peaks of gaseous and liquid phases commonly occurring in inclusions are presented in Table 2.1 extended after Burke, 2001. Spectral windows for selected gas species are presented in Figure 2.1. Their quantitative analysis is discussed in this section.

To determine the relative molar proportions of the components based on Raman data the techniques described in e.g. Burke, 2001; Dubessy et al., 1989; Wopenka and Pasteris, 1987 can be used. The peak areas for gas species are proportional to the number of molecules present in the irradiated volume of the sample. Therefore, the comparison of the relative peak areas of the gases permits their relative proportions to be determined. Molar fractions can be derived using the following simplified formula based on the ratio method of Placzek, 1934:

$$Xa = [A_a/(\sigma_a \zeta_a)]/\sum[Ai/(\sigma i \zeta i)] \qquad\qquad (2.1)$$

where Xa, A_a, σ_a and ζa represent the molar fraction, peak area, Raman cross-section and instrumental efficiency for species a, respectively. Index "i" represents the values for all species present in the inclusion and $\sum$ is their sum (Burke, 2001).
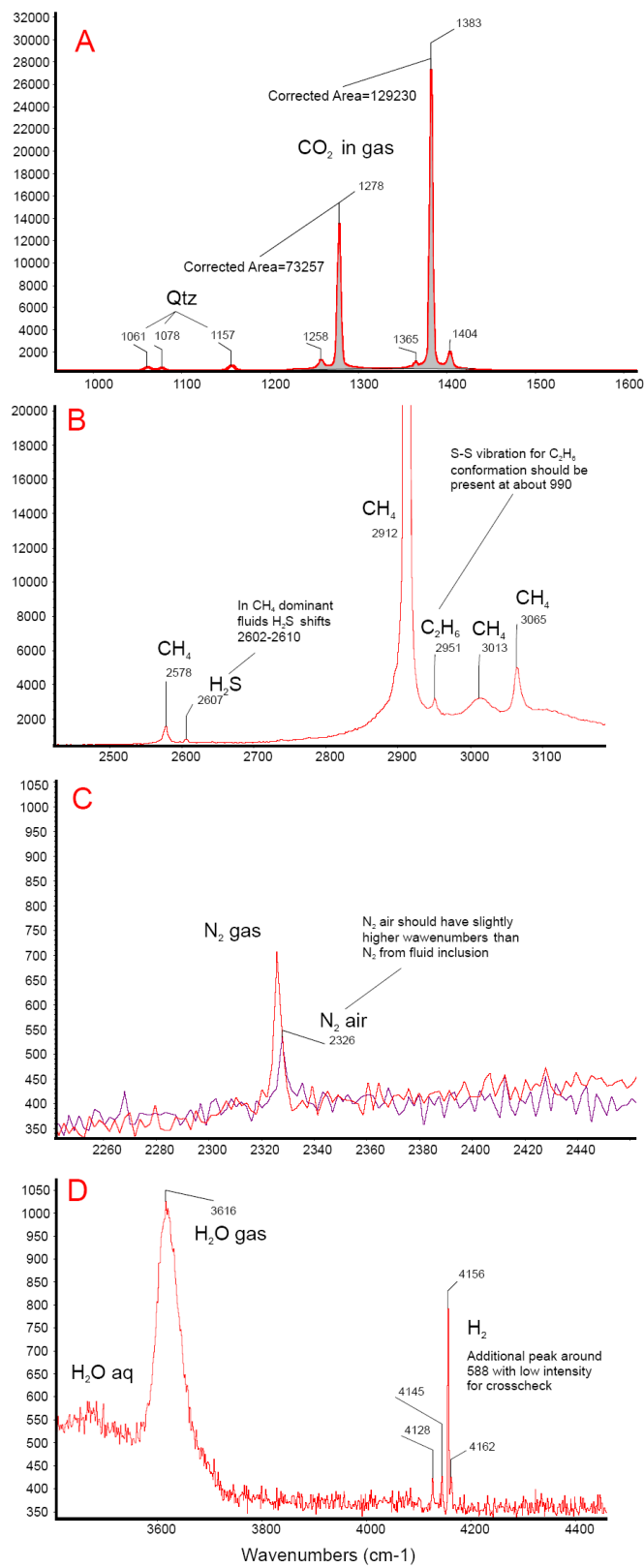
Figure 2.1: Examples of Raman spectra of common gasses

Table 2.1: Important peaks in gas phase together with Sigma and efficiency values for quantitative gas analysis used in our study.

Species	Wavenumber cm⁻¹			Sigma (σ 514nm)	Efficiency
COS	857				
SO_4^{2-}	983				
HSO_4^-	1050				
SO_2	1151		SO_2	5.51	0.6
12 CO_2	1285	1336.5	CO_2+CO_2	2.45	0.7
13 CO_2	1388				
13 CO_2	1370				
CO_3^{2-}		1060			
HCO_3^-	1360	1017			
O_2	1555		O_2	1.19	0.75
CO	2143		CO	0.95	0.9
N_2air			N_2	1	1
N_2	2331		N_2	1	1
HS^-	2574				
H_2S liquid	2580				
H_2S in water	2590				
H_2S	2611		H_2S	6.4	1.2
C_3H_8	2890				
CH_4	2917		CH_4	7.6	1.17
CH_4 dissolved in water	2917				
C_2H_6	2954	990	C_2H_6	14	1.17
H_2O liquid	3219	1600			
NH_3	3336				
H_2O vapour	3657		H_2O(v)	2.3	2.3
H_2	4156		H_2	3.4	1.1

The calculation of individual gas specie is based on the relative comparison of intensities (corrected integrated area) of presented peaks (mole fraction). We are usually integrating the whole peak area and if possible we should rather eliminate peak fitting and deconvolution if the background permits.

The instrument in use needs to be calibrated first in order to obtain the *instrumental efficiency (ζa).* For this purpose spectra from two sets of gas mixtures in special cell CO_2, CO, N_2 and CH_4, N_2, H_2

all in both as 33.33% are collected. Also the relative Raman scattering cross-section (σ_a) of each species needs to be known for the given PT. A list of major gas species cross-sections for common lasers used in fluid inclusion Raman analysis is reported in Burke, 2001.

If the concentration of all the gases in the mixture is the same (33,33%) and the spectral acquisition parameters match, the absolute Raman peak area/high should be the same as well but that is not exactly truth. In reality, the peaks differ and the number quantifying their difference is efficiently, showing the instrument sensitivity to different species.

Please note that calibration could be also performed by use of synthetic fluid inclusions or other gases mixtures of known composition and pressure if required (e.g. for O_2 the measurement of atmosphere air kσ (O_2) can be used because air is a mixture of relatively well known composition).

All the calibration measurements should be made at 31°C (as they are dependent on temperature) and at about 10bar of internal gas pressure in the calibration cell. In other words, the measurements need to be taken after the homogenization of the gas phase of the inclusions and after daughter mineral/clathrate dissolution. If we intend to use different lasers (e.g. 514nm, 488nm) we need to collect calibration measurement to establish (ζa) for each wavelength. The acquisition parameters (time and AC) should be hold constant as much as possible.

In case there are no experimental and calibration data available for the instrumentation in use (ζa) "efficiency" could be inferred from the peaks in surrounding if similar character is expected (for instance C_2H_6 from CH_4).

Calculation of gas mol%

Once we have calibrated our system and obtained the SIGMA values for all the gases of our interest, the relative mol% fractions of e.g. CH_4 (X%(CH_4)) can be calculated according the equations below:

$$X_i=[(I_i/ \sigma_i* \zeta_i)]/SUMA[(I_i/ * \zeta_i)] \tag{2.2}$$

$$I(CH_4)= A(CH_4)/(\sigma_{CH4}* \zeta_{CH4}*t(sec)) \tag{2.3}$$

$$X\%(CH_4) = I(CH_4)/\underline{\Sigma} (ICH_4; ICO; ICO_2; IN_2; ......) \tag{2.4}$$

A= corrected integrated peak area
σ(SIGMA)= relative Raman scattering cross-section
I(CH_4)= Integrated Raman intensity of CH_4
X= mole fraction
Σ= Suma

ζ= "instrument efficiency" (Efficienc)

ζa= the instrumental efficiency for species a;

$$I_i = I_o * \sigma_i * N_i * \zeta_i \tag{2.5}$$

$$X_i = [(I_i / \sigma_i * \zeta_i)] / SUMA[(I_i / \sigma_i * \zeta_i)] \tag{2.6}$$

Please note if the ac (accumulations) are increasing the signal intensities and not just refining/smoothing/improving the spectrum (what is no common in Raman spectra acquisition software) their influence needs to be included in similar manner as for time. Also note that when CO_2 fluid is involved, the sum of the two bands forming the Fermi doublet (1278cm^{-1} and 1388cm^{-1}) should be used and a mixed σ applied:

$$I (CO_2) = (A1287 + A1388) / (2,45 * 0,7 * t) \tag{2.7}$$

$$X_i = I_i / ((SUMA(I_{CH_4}; I_{CO}; I_{CO_2}; I_{N_2}; ......)) \tag{2.8}$$

Measurement Procedure

The spectral windows for all the gases of interest are collected and the corrected area under peaks are used in equations from section 2.2.2

All the microthermometric parameters of the selected inclusions should be known in advance. The equations provided could be used for temperatures approximately around room temperature (10 – 40 °C) but for one set of measurements the match of temperatures is suitable. Please note that some analytical methods used on the same FIA could have the effect on the chemical composition as documented by Lambrecht et al., 2008.

2.2.3 *Aqueous fluids - Aqueous solution study*

The study of the aqueous phase includes the study of presence and/or concentration of polyatomic species like CO_3^{2-}; HCO_3^-; SO_4; PO_4^{3-}; HS^- which are Raman active and their presence/concentration in fluid phase could be detected has been quoted by many authors (e.g. Dubessy et al., 1989). Generally speaking, any Raman active polyatomic species whose concentration in the fluid is above detection limits could be identified. Some problems arise if mineral matrix effects the identification by peak overlaps or if quantification is required (Figure 2.2). To see the examples of possible approaches in quantification see Chapter 4. It should be noted that the constraint on the salinity of the whole system could be also dedicated from the water

stretching vibrations at about 3600 cm^{-1}. Usually the information about the main cations in the solution is not obtained directly from the aqueous solution measurements and low temperature measurements of their stoichiometric gas hydrates need to be taken (e.g. Baumgartner and Bakker, 2010).
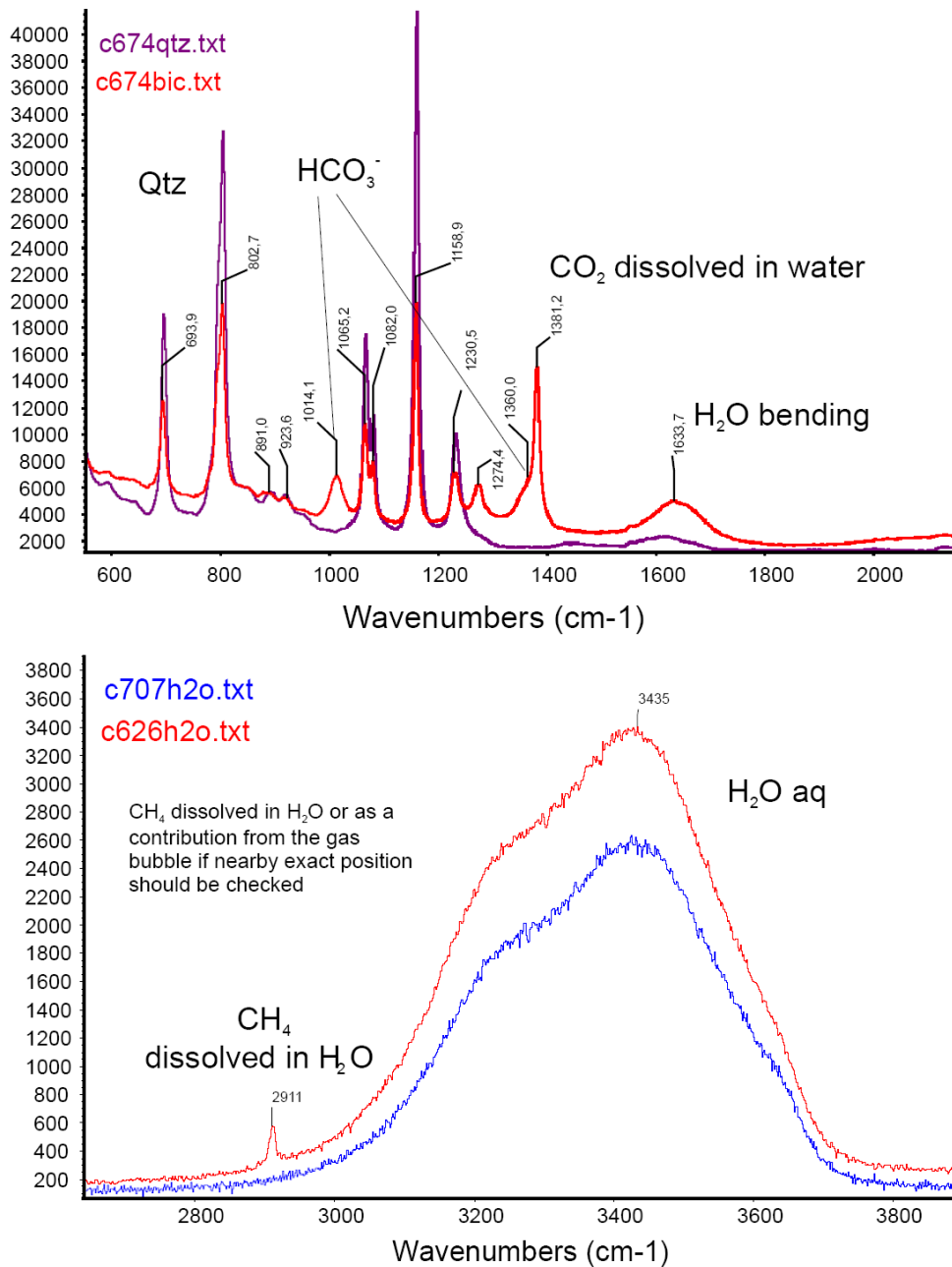
Figure 2.2: Examples of Raman spectra from aqueous solution.

2.2.4   High temperature measurements of homogenous fluids

High temperature (HT) measurements can give us the useful information about the overall chemistry of the paleofluid. The problem is the non-existence of the efficiency (ζi) and SIGMA (σi) values for HT conditions. New attempts were conducted by Azbej et al., 2007 using external standards as synthetic inclusions or their analogues for calibration of individual systems. Also there is an dependence of a SIGMA values on temperature, it was shown by Tsunogae and Dubessy, 2009 that for selected species the variation of the constant for selected temperature ranges is minimal and sometimes can be neglected.

2.2.5   Identification of solid phases by Raman

Solids can be easily identified by LRMS in fluid and/or melt inclusions (Burke, 2001). Some of the common phases and their main Raman peaks are presented below:

Carbonates
  Aragonite 152, 209, 710, 1089
  Calcite 156, 283, 711, 1085
  Mg-calcite 157, 284, 714, 1087
  Magnesite 329, 738, 1094
  Dolomite 176, 299, 725, 1097
  Nahcolite 684, 1046, 1266

Sulphates
  Anhydrite 515, 628, 674, 1015
  Gypsum 492, 623, 671, 1006, 3250, 3500
  Barite 460, 988

Phosphates
  Apatite 966

For C-O-H fluids also the presence of graphite which could coat the inclusion walls should be checked. The state of graphite crystallinity can be also analyzed. The spectra of fully ordered graphite show sharp peak at 1582 cm^{-1} and no peak at ~ 1355 cm^{-1}, whereas disordered graphite (carbonaceous matter) has a prominent peak at ~ 1355 cm^{-1} and a less intense peak at ~ 1600 cm^{-1}. The intensity ratio between the disordered and ordered peaks (D/O) could be used as an indicator of structure order of graphite (Wopenka and Pasteris, 1993; Huff and Nabelek, 2007).

2.3   LA-ICP-MS

LA-ICP-MS (Laser Ablation Inductively Coupled Plasma Mass Spectrometry) is a powerful analytical technique that enables direct microsampling of various materials. Its application in the field of fluid inclusions research allowed the measurements of elemental composition in individual fluid inclusions (Halter et al., 2002; Gunther, 2001; Wilkinson et al., 1984; Gunther et al., 1998). Due to the developments involving introduction of homogenized excimer lasers and optimization of the transport system and carrier gas composition (Günther and Heinrich, 1999), this technique now provides good detection capabilities for the trace element analysis of very small inclusions (Heinrich et al., 2003). Nevertheless, similarly to other micro-analytical techniques quantification of the elemental compositions is still difficult. Synthetic fluid inclusions where known concentrations of elements were added as internal standard were used to demonstrate the potential of the LA-ICP-MS (Loucks and Mavrogenes, 1999). Moissette et al., 1996; Shepherd and Chenery 1995 and others have reported qualitative data using LA-ICP-MS. The use of internal standard in natural fluid inclusions is bounded by the possibility of providing the concentration measurements for selected element within inclusions by other nondestructive analytical prior to laser ablation. Sodium concentration obtained by microthermometric measurements was shown to provide a suitable internal standard for certain inclusions (Longrich et al., 1996; Günther et al., 1998). Exact inclusion volume calculations (for techniques used consult Chapter 7) before laser ablation were tested as an alternative approache for quantification of element concentrations in fluid inclusions.

During this study, a LA-ICP-MS methodology and the software for interpretation of fluid inclusion analysis (ExLam 2011) was developed and tested at the Charles University in Prague. The developments follow up our earlier studies performed during MSc. project of the author (Hrstka, 2004). During this project, LA-ICP-MS measurements were performed at the Imperiall Colleague of London to validate results obtained at our facilities at Prague. The main problems we faced during the analysis of orogenic gold related paleofluids from our localities (Libčice, Roudný and Kasejovice) were related to the relatively low salinity (<4 wt% NaCl equivalent) and the relatively small size of all available inclusions (< 20 um). Even though the results of our tests are not presented in this thesis a development of software and hardware for quantitative analysis of low salinity fluid inclusions formed a part of our recent years effort (Hrstka et al., 2006) and are planed to be published separately.

2.4   Cathodoluminescence SEM-CL

Cathodoluminescence (SEM-CL) uses a visible light signal emitted by a beam of electrons impacting luminescent material. Its applications in geosciences has been reviewed in many publications (e.g. Habermann, 2002; Marshall, 1988; Pagel et al., 2000 (Eds.))

Cathodoluminescence (CL) designates the luminescence of UV to IR wavelengths induced by electron bombardment in minerals. SEM-CL can be caused either by intrinsic defects of the crystal lattice, such as non-stoichiometry (i.e., atomic vacancies) and structural imperfections (i.e., defects in the crystal structure) or to impurities (i.e., trace elements). Variability in CL colors can be thus related to re-distribution of defects and trace elements in the crystal structure during crystal growth (Götze et al., 2001). This technique proved to be invaluable for distinguishing individual quartz populations and tracing potential defects surrounding fluid inclusions affected by re-equilibration (e.g. Boiron et al., 1992). It can reveal a wide range of growth and alteration textures that are useful for understanding the formation history of ore deposits (Holness and Watt, 2001; Müller et al., 2003; Rusk and Reed, 2002)

During our study (SEM–CL) of selected quartz samples was performed at Natural History Museum in London using JEOL 5900LV Analytical SEM with an attached GATAN MiniCL detector. INCA© software was used in order to create the montage of individual pictures in the final CL maps (Figure 2.3). This technique proved to be invaluable for distinguishing individual quartz populations and tracing potential defects surrounding fluid inclusions affected by re-equilibration. The applied acceleration voltage and current was 20 kV and ~1 nA, respectively.
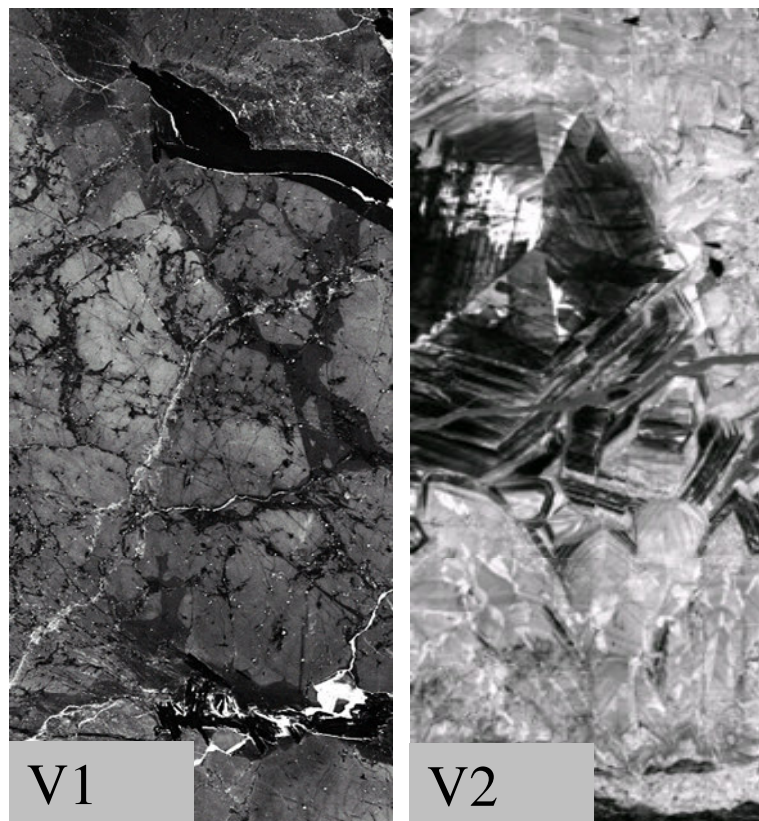
Figure 2.3: Example of CL-SEM maps from Kasejovice main quartz veins V1 and late quartz veins V2.

2.5 Quantitative Evaluation of Minerals Using Scanning Electron Microscopy (QEMSCAN)

The QEMSCAN *(Quantitative Evaluation of Minerals using Scanning Electron Microscopy)* technology is a widely accepted automated e-beam technique providing quantitative and statistically robust mineralogical data to the mining industry. It uses the X-ray mapping combined with BSE brightness to identify minerals in almost any type of geological material (Gottlieb et al., 2000; Pirrie and Rollinson, 2010; Hoal et al., 2009).

As the QEMSCAN distinguishes the different phases based on the correlation of X-ray spectra to a chemical composition of the mineral sample, it can be used to identify a wide variety of materials while the detail of information obtained could be really task specific. For the purposes of specific analysis of unknown samples, mixed phases and solid solutions the spectral database (SIP) can be updated and refined to cope with complex ores and unusual mineral chemistries (Gottlieb et al., 2000).

For the quality control purposes the accuracy and reproducibility (reliability) of the data are usually checked against the independent chemical assay. Also an independent method like QXRD, optical microscopy, SEM–EDS or Raman can be used for crosscheck. Quantitative modal data validation is based on the theoretical "mineralogical" assays calculated using the chemical composition of individual minerals, together with the results of the modal analysis and mineral densities. This provides a control on the appropriate assignment of the chemical and density data to each mineral of interest based on the (SIP) and primary list criteria.

Beside a modal mineralogy, also the liberation, associations, average grain size and other textural information can be obtained. This technique has been used in the effort to automatically search for mineral phases in rock samples from the Libčice district and evaluate the advances in automate mineralogy and petrology of fine grained rocks in general (see Chapters 5 and 6 for details).

2.6 Confocal Laser Scanning Microscopy (CLSM)

Confocal microscopy is a microscopic technique producing 3D images by alignment of 2D confocal sections in computer (Fredrich, 1999; Gu, 1996). In spite of the fact that CLSM techniques are nowadays almost routinely used in biology and medicine, there were not many publications available on their use in earth sciences. This chapter outlines some novel potential applications of CLSM in fluid inclusion research in general. Our effort was focused on examining the potential of geological samples which could benefit from this 3D microscopic technique. Especially the possibilities of exact 3D fluid inclusion reconstructions and volume calculations (e.g. Petford et al., 1994) were tested as a part of this thesis (Appendix A.3).

Introduction

The CLSM was firstly discovered and developed by Marvin Minsky in 1953, but it took more then thirty years for CLSM to become a standard scientific microscopic technique. The whole principle of confocal microscopy could be simply described as an effort to eliminate the light from non-focal plains "flare" to participate on the final microscopic image. The in focus depth of classical optical microscope is given from the aperture of the objective in use and the wavelength of light (typically in 10um range). In confocal microscopy this quantity is determined moreover by the confocal pinhole in use, which taper off the focus depth to nm scale and dramatically increase the achievable vertical resolution in potential 3D reconstructions. Several different alignments are used in order to achieve the confocal effect. The two main mechanisms are spinning-disk/Nipkow disk confocal microscopy (SDCM) developed by David Egger and Mojmír Petráň in 1967 and confocal laser scanning microscopy (CLSM) developed in 1978, by Thomas and Christoph Cremer. The schematic illustration of the CLSM system is presented at Figure 2.4. For more details on CLSM instrumentation and principles the reader is referred to many available reference works (e.g. Pawley JB (editor) (2006); Spring and Davidson, 2005). It is worth noting that for the applicability of the Confocal microscopy the special object qualities are required which is either the reflectivity for the laser (CLSM)/ Light (SDCM) form the object or the fluorescence response to the laser excitation of the sample.
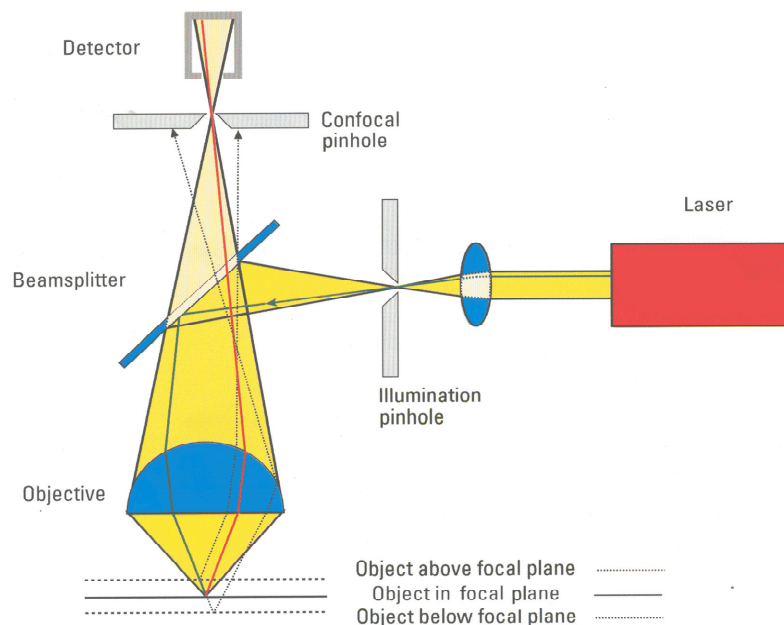
Figure 2.4: Example of configuration of common confocal laser scanning instrument (CLSM).

Instrumentation (methodology)

During our measurements on different geological samples we have used Olympus FV1000, Olympus FV300 and Leica SLd parameter microscopes. The sample preparation was dependent on the specific method used. Basically, we were able to study samples which are either fluorescent their self's, could be colored by fluorescent reagents fluorochroms or can make the laser to reflect in the reflected confocal microscopy mode. No other special sample treatment is necessary and classical microscopic thin sections, polish blocks etc. can be used for examination.

Software

One of the advantages of confocal microscopy is the digital character of the pictures, which allowed us to use image analysis and treat pictures automatically (Sheppard et al., 1997). The rapid progress in computer technology and software development brings us all advantages of real time 3D data visualization and analysis. In our experiments, the commercially available Bitplane IMARIS$^{©}$ software was used together with image J and LSC light program for almost all the data treatment and volume reconstructions and calculations. Currently, there is also a plenty of other software packages available for confocal microscopy (e.g. Voxel, Auto Align, Tracer 3D, SEM Align, 3D studio MAX).

Fluid inclusion study by CLSM

Precise knowledge of the inclusion volume and of the volume of individual phases inside the inclusion (e.g. bubble, solids, etc.) is of crucial importance for the calculation of fluid properties (density). Nowadays, an inaccurate volume estimates made on comparative charts (e.g. Roedder, 1984 or Shepherd et al., 1985) are still widely used. More precise estimations are based on sample rotation and accurate planar measurements (e.g. Diamond at al., 2003; Bakker and Diamond, 2006 and Stoller et al., 2007). Recently, the CLSM was tested in such applications. As we stated earlier, the CLSM can be used for exact 3D reconstruction of individual inclusions with some limitations. From our experiments and as reported also by Aplin et al., 1999 and Pironon et al., 1998, the volume calculations from the fluorescent inclusions are accurate within the 5% RSD. An example of precise 3D reconstruction of an inclusion is presented on Figure 2.5.
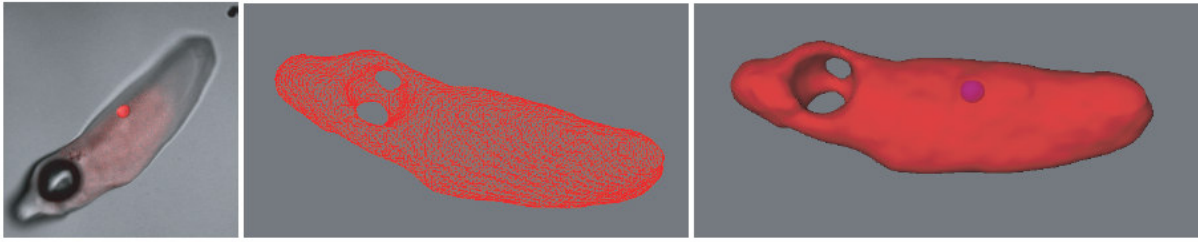
Figure 2.5: Three steps in 3D reconstruction and exact volume calculation of individual fluorescent fluid inclusion. The method used is Confocal Laser Scanning Microscopy CLSM with precision in volume calculation established to better then 95%.

For the aqueous inclusions the situation is more complex and the reflected mode needs to be used for their study because of their non-fluorescence nature. During our experiments we have been able to use the reflection on the phase boundary between the inclusion and also between the individual phases trapped within its void to visualize the exact inclusion position in the quartz matrix in 3D (Figure 2.6). We have also tried to combine the information of CLSM DIC mode and florescence signal to produce the 3D reconstruction of inclusion interior but this approach provides very limited success. For the samples studied it was not possible to obtain reliable volume estimate for non-fluorescent inclusions/matrix. We suggest that future tests on non-fluorescent (aqueous, aqueous-carbonic etc.) inclusions trapped in potentially fluorescent matrix should be performed to evaluate the possibility of "negative" 3D imaging of fluid inclusions. Possible fluorescent matrix includes calcite, dolomite, fluorite, sphalerite, apatite, zircon, monazite and others. Obviously, the inclusions trapped in amber or other organic materials can be examined by similar fashion.

As the volume calculation is not the only important parameter which could be obtained by the CLSM, we have also focused our attention on the ability to locate the FIA and their 3D distribution in quartz. It has been showed that even very small inclusions (>1um) which are not easily located by classical microscopy can be reliably identified in quartz based on their reflection. This allowed us to construct 3D reconstructions of FIP which could be used in orientation studies.

The important information/data which could be obtained by application of CLSM in this field of research are:

- Bubble filling degree estimations for autofluorescencet hydrocarbon-bearing inclusions (Pironon, 1998). Autofluorescencet inclusions are the most easily worked objects for volumetric reconstruction.

- Distribution of submicroscopic H_2O inclusions around the big ones (e.g. Aplin et al., 1999) is also possible via CSLM (e.g. Petford et al., 1994; Apine et al., 1999; Hrstka, 2006[b]) and can be used in inclusion reequilibration studies.

- 3D reconstructions and volume estimates for non-fluorescent (e.g. H_2O-CO_2-CH_4) inclusions entrapped in autofluorescencet (non-SiO_2) matrix are promising for future research
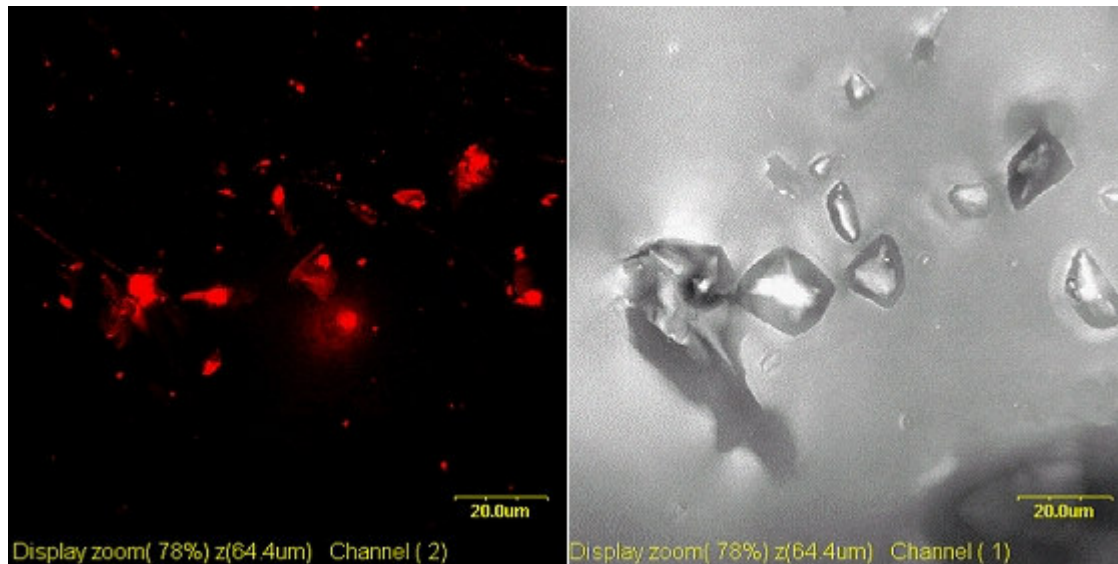
Figure 2.6: Example of reflected CLSM image of non-florescent inclusions from Kasejovice gold deposit

Apart from the importance of the precise volume fraction estimates in the thermodynamic calculations (Huizenga, 2001; Bakker, 2003), the knowledge of inclusion volume can be used for the standardization of single inclusion analysis methods like PIXE and LA ICP MS.

2.7   3D Nano-tomography

X-RAY NanoTomography is a method which combines X-ray transmission technique with tomographical reconstruction by using the focused X-ray beam pointed on the rotating sample. The data are simultaneously recorded by CCD detector and transferred to the PC which use the Cone-beam volumetric reconstruction algorithms (Feldkamp algorithm) for creation of the 3D image of the sample from the individual recorded 2D (radiography) sections (Skyscan, 1977). The great advantage of the NanoTomography is that it does not need any preparation, coating or vacuum treatment for the studied sample (Tricart et al., 2000). The final images represent a mixed combination of density and compositional information from the specimen (Baruchel et al., 2000). The maximal diameter of the sample is 10mm for SkyScan-2011 and about 50mm for SkyScan1172 where the resolution is about 150-250nm and 5um respectively (Skyscan, 1977). In spite of the fact that tomography techniques are nowadays almost routine used in biology, medicine and material sciences there were not many publications available on their use in earth

sciences. As a part of this thesis, we have focused on the potential application of this technique in precise fluid inclusion 3D localization and volume reconstruction Figure 2.7. All the measurements in this study were performed on NanoTomograph SkyScan-2011 in the SkyScan laboratory Belgium an are presented in the Chapter 7. Our work in this field is to the best of our knowledge the first attempt to apply 3D NanoTomograph in fluid inclusion research.
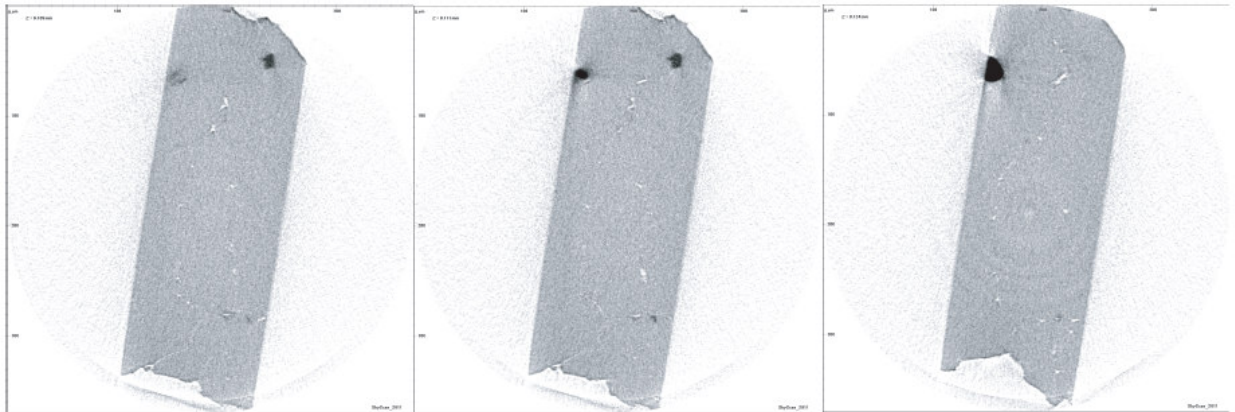
Figure 2.7: Individual 2D sections of a part of double polished thin section with numerous fluid inclusions on secondary trails as constructed by Nano CT SkyScan-2011.About few thousands of individual sections are used for computer 3D reconstruction of the sample. The dark parts represent small sulphide grains (higher density) grey matrix is quartz and white holes represent individual fluid inclusions.

3. BICARBONATE-RICH FLUID INCLUSIONS AND HYDROGEN DIFFUSION IN QUARTZ IN THE LIBČICE OROGENIC GOLD DEPOSIT, BOHEMIAN MASSIF (ARTICLE 1)

Tomáš Hrstka[1], Jean Dubessy[2], and Jiří Zachariáš[3]

[1] *Institute of Geology AS CR, v.v.i., Rozvojová 269, CZ-165 00 Prague 6 – Lysolaje, Czech Republic E-mail:* **hrstka@gli.cas.cz**

[2] *G2R(UMR 7566), Faculté des Sciences, Université Henri Poincaré-Nancy Université, BP-70239, 54506-Vandoeuvre-les Nancy Cedex France, E-mail: Jean.Dubessy@g2r.uhp-nancy.fr*

[3] *Charles University in Prague, Faculty of Science, Institute of Geochemistry, Mineralogy and Mineral Resources, Albertov 6, Praha 2, CZ-128 43, E-mail: zachar@natur.cuni.cz*

Abstract

Unusual paleofluid composition is reported for the Libčice orogenic-type gold deposit located in the Central Bohemian Plutonic Complex (CBPC), Czech Republic. Unexpected bicarbonate-rich fluids and their complex chemistry variations characterize primary fluid inclusions from the main gold-bearing quartz vein. Detailed microthermometry, Laser Raman Micro Spectroscopy (LRMS) and SEM cathodoluminiscence study was used to understand the complex chemistry and PTX history. The results indicate the presence of H_2O and H_2O-CO_2-CH_4 ($\pm$ N_2; H_2S) fluids, the latter displaying variations of the CO_2/CH_4 ratio in the gaseous phase from 6.8 to 0.06. Variation of the CH_4 content across single grains and between different levels of the mine was recorded. The presence of nahcolite, H_2 (up to 6 mol%) and ethane (0-0.2 mol%) in the fluids was also discovered by LRMS. Potential models for the formation of different types of fluids present in the deposit are discussed, including the genesis of HCO_3^- rich fluids as well as H_2 and C_2H_6 presence in the primary fluid inclusions. The potential influence of organic matter-bearing sediments, as well as the impact of the intrusion of CBPC, re-equilibration and/or re-speciation of fluid inclusions during the post-entrapment history are considered to have the main impact on the complex paleofluid chemistry. Based on the thermodynamic modeling, H_2 diffusion into the fluid inclusions was shown to be a main reason for the CH_4 variation on the scale of a single grain, as well as across the whole vein. Although the exact processes of production/formation of HCO_3^- and H_2 at the Libčice deposit remain open to discussion, reactions in the C-O-H system are considered to be a possible formation mechanism. This work also contributes to our understanding of the importance of post-entrapment modifications and reactions in the C-O-H system on interpretation/deciphering the processes in orogenic-type deposits.

Keywords: orogenic gold deposits, fluid inclusions, hydrogen diffusion, bicarbonate, Raman spectroscopy

3.1   Introduction

Fluid inclusion study is an important part of any ore deposit research and helps us to understand the fluid-rock interaction processes in general. The importance of a detailed and complete analytical and research approach in this field is unquestionable, as shown on the case study of unusual fluid compositions, where classical microthermometry cannot answer our questions about the fluid composition and evolution necessary for understanding the PTX conditions during the formation of the ore deposit. A fluid inclusion study of the Libčice deposit located in a contact zone of the Central Bohemian Plutonic Complex (CBPC) and belonging to the group of orogenic metalogenetic units of the Europe Variscian belt is described. This deposit is situated within a metallogenic zone with numerous gold deposits, like Mokrsko, Petračkova hora, Jílové, Kasejovice, Belčice (Boiron et al., 2001; Zachariáš, 2002; Zachariáš et al., 1997, 2001). The presence of nahcolite, H_2, ethane, multisolid inclusions and HCO_3^- in high concentrations makes the processes at the Libčice gold deposit quite unique, compared to classical orogenic gold deposits.

At the present time, the origin of the characteristic H_2O-CO_2±CH_4 fluids at the orogenic-type gold deposits is still controversial (Ridley and Diamond, 2000). Their generation has been attributed to metamorphic fluids, deep circulating meteoric water, magmatic fluids or other sources (e.g. Boiron et al., 1999, 2001, 2003; Goldfarb et al., 2001, 2005; Groves et al., 1998; Hagemann and Cassidy, 2000; Kerrich and Cassidy 1994). In addition to the common H_2O - CO_2±CH_4 fluids reported for the majority of orogenic-style gold deposits, the presence of variable amounts of non-aqueous volatiles, such as CH_4-N_2 and their fraction variations, have also been reported (Barrie and Touret, 1999; Klemd et al., 2002; Ridley and Hagemann, 1999; Zachariáš, 2002). Different approaches were employed to understand the paleofluid generation model and its importance for the mineralization process (and the reasons for fluid chemistry variations). In this study, based on room temperature and high temperature Laser Raman Micro Spectrometry (LRMS), the potential processes leading to the fluid composition variations on a small scale (i.e. grain scale) to a large scale (i.e. mine scale) are discussed. Compared to other locations, the paleofluid chemistry variations at the Libčice deposit are quite unique because of the preserved intra-grain variability and especially the presence of concentric profiles.

Bicarbonate-rich fluids reported in this study have never been reported for an identical environment (Burke, 2001; Dubessy et al., 1989; Kruger and Diamond, 2001). From the point of view of thermodynamic modeling, not many publications are concerned with the importance of HCO_3^- in paleofluids at higher temperatures. Speciation studies in the C-O-H (C-O-N-H-S) systems (Chen et al., 2004; Dubessy and Poty, 1988; Frantz, 1998; Huizenga, 2001; Martinez et al., 2004; Morgan et al., 1992) do not favour higher concentrations of HCO_3^- in the fluid phase under the conditions relevant for the formation of orogenic-type gold deposits (Goldfarb et al., 2001, 2005). The presence of high concentrations of bicarbonate in fluid inclusions from the Libčice deposit is discussed in detail in order to understand the paleofluid evolution. Large

variations in the CH_4/CO_2 ratio observed in the gaseous phases of individual inclusions and a systematic increase in CH_4 contents across analysed quartz grains is also discussed. A multi-analytical approach is emphasized when microthermometry alone is shown to be insufficient for solving such complex tasks. H_2 diffusion is proposed as an important post-entrapment modification leading to the observed CH_4/CO_2 variation.

The presence of hydrogen in fluid inclusions is discussed from the point of view of potential H_2 genesis in paleofluids, such as water radiolysis, fluid reactions with organic matter and reactions involving fluid-rock interactions (Dubessy et al., 1988; McCollom and Bach, 2009; Tsunogae and Dubessy, 2009). An elevated H_2 content is considered unusual for common paleofluids and has not been reported for similar geological conditions in the past. The presence of ethane (C_2H_6)-bearing aqueous carbonic fluids in the orogenic gold deposit setting is also rather rare (Bray et al., 1991).

3.2   Geological Setting

The Libčice deposit (Figure 3.1) is situated in Neoproterozoic intermediate to acid volcanic rocks of the Kozí Hory belt, in a narrow contact-metamorphic aureole of the Variscan Central Bohemian Plutonic Complex (CBPC; Holub et al. 1997a,b). The volcanic rocks (rhyolite to dacite) and their tuffs are overlain by silicified Neoproterozoic black shales (Lečice member). The Neoproterozoic rocks were intruded by two sets of lamprophyre dykes of unknown age. Dykes, up to 2 m thick and up to 1000 m in length, trend N-S (older dykes) and E-W (younger dykes). The main lamprophyre dyke changes over from spessartite to kersantite while the younger NE dykes correspond to kersantite.

Lečice black shales were formed in euxinic conditions during a long period of basin starvation (Suchý, 1992). They are rich in organic matter up to 1.5 wt.% of C org. (graphite, kerogen and pyrobitumen in variable proportions; Suchý et al., 2007) and in pyrite (up to 2 wt.% S). It is worth noting that the complexity and heterogeneity of organic materials coexisting in the rocks - kerogen, pyrobitumen and graphite (as well as "poorly organized graphite") - were all reported in literature for these rocks (Suchý et al., 2007).
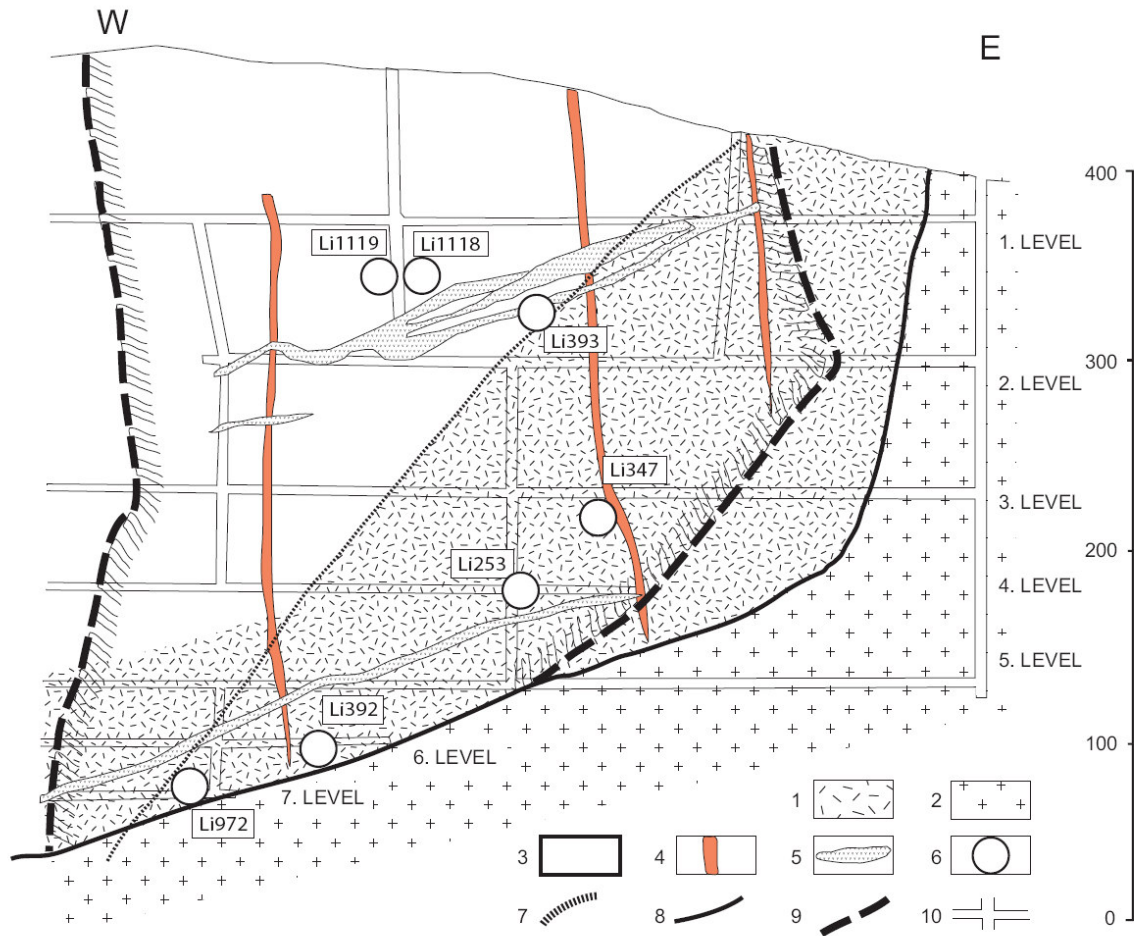
Figure 3.1: Vertical cross-section of the Libčice deposit underground mine, viewed parallel with the Main Vein,simplified after Šrein et al. (1995): 1 – rhyolite; 2 - peripheral biotitic granite (CBPC unit); 3 - Neoproterozoic black shales (Libčice member); 4 - Lamprophyre dykes; 5 - Aplites; 6 - Sample location; 7 - Fault zones; 8 - Granite contact; 9 – Outlines of the Main quartz Vein; 10 – Mine workings.

The Neoproterozoic volcanic rocks and gold-bearing quartz veins are underlain by peripheral biotitic granite of the CBPC unit (Libčice granite) at depths of 300-500 m under the present surface. In some places in the mine, the granite cuts and some associated aplites crosscut the main Libčice quartz vein. In the deepest parts of the mine, lamprophyres as well as hydrothermal quartz were also found as xenoliths in the peripheral granite. The thermal effect of the intrusion of the Libčice granite and possibly also cumulative thermal effect of other CBPC intrusives is responsible for recrystallization of quartz gangue and of the associated ore minerals and possibly also for the transformation of former carbonate gangue in some deeper parts of the mine into a calc-silicate (skarnoidal) assemblage.

The Libčice ore district consists of one dominant quartz vein ("the Main Vein") and of several other smaller veins (uneconomic), parallel, or perpendicular to the Main Vein. The veins largely follow the contact with lamprophyre dykes (N-S and E-W). The Main Vein is about 400 m long, usually 0.2-0.4 m, in places up to 1.5 m thick, striking W-E and dipping 70-90° to N/S. The quartz gangue of the Main Vein is formed by coarse grain, white to greyish quartz (denoted as Q1) exhibiting different degrees of thermal recrystallization. Younger quartz veins (denoted as Q2) are associated with E-W and/or N-S trending lamprophyre dykes in a broader area; however, they are relatively gold-poor, and significantly less thick. Quartz veinlets (denoted as Q3) within the fault calcite gangue are volumetrically minor and mineralization-free. Only data for the Main Vein (Q1) are presented and discussed in this paper.

Compared to other veins (Q2, Q3) in this area, only the Main Vein is located within the thermal aureole of the CBPC granites. In order to discriminate microtextures of the Main Vein quartz gangue we denoted sparse remnants (i.e. relicts) of original unrecrystallized quartz as Q1Ur, while the quartz that resulted from recrystallization of Q1 we denote as Q1N ("neoformed quartz"). Generally, the Q1N quartz dominates the gangue with 60-80 %.

The mineralogy of the deposit was reported previously (Litochleb and Šrein, 1994; Sejkora et al., 2009; Šrein et al., 1995; Zachariáš, 2002). The sulphide contents are generally low (less than 5%). Pyrrhotine is the main sulphide, followed by arsenopyrite, pyrite, chalcopyrite and marcasite. Löllingite is rarely found as inclusions in arsenopyrite. Native gold is present in two generations (gold-I with 2-5 wt. % Ag and younger gold-II with 12-13 wt. % Ag). Gold-I predominates and is commonly associated with Bi-Te-S phases. The occasional presence of various silicates – pyroxene (salite), grossular, titanite and wollastonite – was also reported from the Main Vein (Šrein et al., 1995).

The presence of xenoliths of the Main Vein (with visible gold-I) in the contact granitoids of the CBPC and also the presence of original carbonate gangue (*originally younger than gold-I*) transformed into the skarnoidal assemblage suggest that contact metamorphism of the district occurred after the formation of gold-I. The age of distal veins (Q2), rich in arsenopyrite, is difficult to assess, as is timing with respect to the contact metamorphism. The late quartz (Q3), however, clearly postdates the contact metamorphic event.

3.3   Methods and Samples

All the samples were prepared from the main quartz vein as thin sections for petrography and double polished wafers for fluid inclusion study. The samples represent both the lateral and the vertical profile of the deposit.

Microthermometric measurements were performed using the LINKAM THMSG 600 heating-freezing stage accompanied by OLYMPUS BX50 petrographic microscope at Charles University

in Prague and calibrated using synthetic substances with known melting points and natural pure CO_2 inclusions. The accuracy and precision have been calculated as $\pm$ 0.1 °C over the whole range of observed phase changes in the low temperature regime and about 1 °C for high temperature measurements. Where necessary, the clathrate melting temperatures were determined by temperature cycling (Diamond et al., 1994). Microthermometric abbreviations for temperatures of measured phase transitions are used in concordance with Diamond (2003): Ti (initial melting), Tm (final melting), Th (homogenization temperature).

Qualitative and quantitative Laser Raman Micro Spectrometry (LRMS) analysis was performed at the G2R laboratory in Nancy, using a Labram Dilor Jobin Yvon instrument (300 mm focal length; 1800 groove/mm grating), where the excitation radiation is 514.532 nm provided by an Ar^+ Laser Spectral Physic. High temperature LRMS measurements were performed by accompanying the instrumentation with a LINKAM THMSG 600 heating-freezing stage. The atmospheric N_2 correction for LRM analysed inclusions was determined by blank quartz measurements at the same focal depth outside the inclusion (e.g. Dubessy et al., 1989).

The Package FLUIDS 1 (Bakker, 2003) and the spreadsheet tools of Huizenga (2005) were used for interpretation and modeling of both the microthermometrical and the LRM results. Due to the lack of experimental data for complex, bicarbonate-rich, aqueous carbonic fluids, a theoretical salinity of 4 wt.% NaCl was used in all the calculations of the bulk fluid properties.

Cathodoluminiscence (SEM–CL) of selected quartz samples was performed at the Natural History Museum in London using a JEOL 5900LV analytical SEM with an attached GATAN MiniCL detector. The applied acceleration voltage and current were 20 kV and ~1 nA, respectively. INCA$^©$ software was used to create the montage of individual pictures in the final CL maps.

3.4   Quartz Microtexture of the Main Vein

The microstructures of the Main Vein quartz gangue indicate progressive recrystallization with remnants of the original quartz crystals preserved as "relict" grains (Q1Ur) and the matrix represented by recrystallization-related "neoformed" grains (Q1N). Relicts of Q1Ur have over 20 mm in size, mostly irregular, rarely regular shape and dark-grey mottled appearance due to numerous, randomly distributed fluid inclusions (2-50 μm in size). In contrast to Q1Ur, the newly formed grains (Q1N) and subgrains are clear, transparent and almost inclusion free. The Q1N grains have uniform size on a sample scale (Figure 3.2) and often exhibit sacharoidal texture, typical for thermally induced, strain-free recrystallization. Clear transparent grains, however with relatively abundant fluid inclusions, often occur as single grain inclusions enclosed in a pyrrhotite (sulphide) matrix. These also represent the Q1N type. Contact "relict" quartz (Q1Ur) is absent in samples from the immediate vicinity of the granite.

Q1Ur and Q1N exhibit very similar luminescence intensities. Therefore, the use of SEM-CL to distinguish between Q1Ur and Q1N is limited. The quartz (Q1Ur, Q1N) is also sensitive to the beam energy and the CL image thus vanishes rapidly under the exposure (Figure 3.2). Fluid inclusions trapped in Q1Ur and Q1N are not associated with any remarkable difference in the luminescence of the host.

The difference between Q1Ur and Q1N is thus, paradoxically, best seen with a normal optical microscope with plane-polarized transmitted light. The difference in the transparency between Q1Ur and Q1N increases significantly if polished wafers for fluid inclusions (about 250 μm thick) are used instead of standard polished thin sections (only 30-50 μm thick).

3.5   Fluid Inclusions Petrography and Microthermometry

Four types of primary to early secondary fluid and multisolid inclusions were identified in the relic (Q1Ur) and recrystallized (Q1N) quartz of the main Libčice vein. Secondary fluid inclusion trails were also recognized, but not studied in greater detail. Histograms of all the relevant microthermometric data are presented in Figure 3.3 and fluid inclusion microphotographs are shown in Figure 3.4 and Figure 3.5.
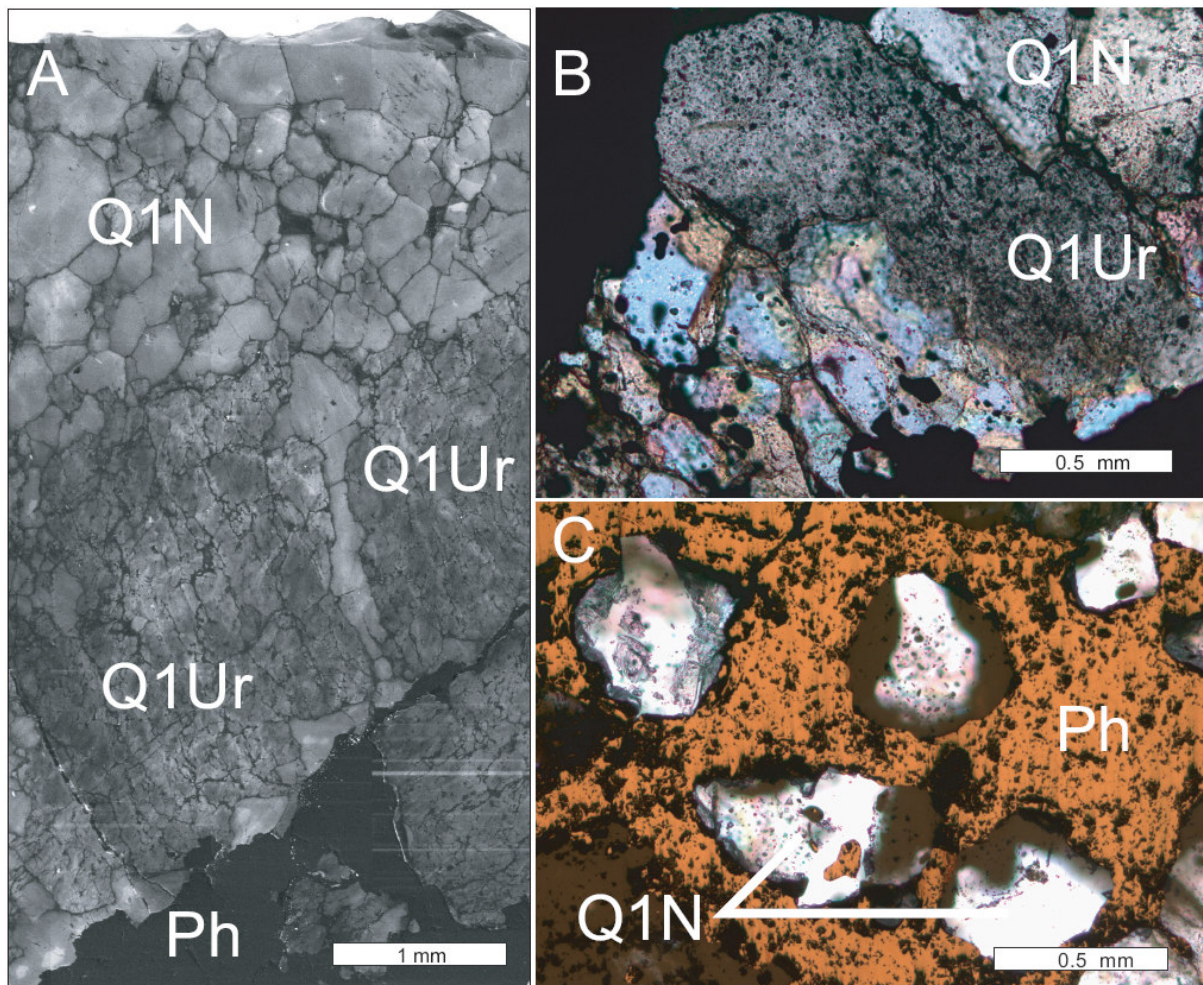
Figure 3.2: Microphotographs of quartz gangue of the Main Vein (A): SEM-CL map constructed from about 30 individual images showing the two types of quartz. (B): Microphotograph in transmitted light of dark relict grain (Q1Ur) enclosed in a transparent matrix of neoformed quartz (Q1N); (C): Microphotograph in transmitted light showing isolated grains of clear transparent quartz (Q1N) enclosed by a massive pyrrhotite matrix. Symbols used in all photos: Q1Ur - relict quartz representing the original Q1 gangue; Q1N - *neoformed* quartz formed by solid state-recrystallization; *Ph* – Pyrrhotite.

Aqueous-carbonic inclusions in relict quartz (Type 1 inclusions)

Type 1 inclusions are mostly two-phase (aqueous liquid + carbonic vapor), rarely three-phase (aqueous liquid + carbonic liquid + carbonic vapor) at room temperature (Figure 3.4) and 3 to 50 µm in size (commonly 10-20 µm). They are hosted only by relict quartz (Q1Ur). The inclusions occur randomly and are 3D-distributed, either in small clusters, or as isolated inclusions. Therefore we suggest their primary origin. Typical secondary trails are missing. The volume fraction of aqueous liquid is (0.5 ±0.1), and the shape of the inclusions is variable (negative crystal shapes being the most common). Some inclusions contained 1 or 2 birefrigent crystals identified by

Raman spectroscopy as nahcolite and calcite (Figure 3.6). These solids can be found in about 25-40 % of all the type 1 inclusions, but can easily be overlooked. In inclusions that look unaffected by recrystallization and/or leakage, the volume occupied by nahcolite and calcite crystals is relatively constant (~ 5 vol. %). In a few type 1 inclusions, other unidentified solids were sporadically present. The relatively constant volume ratio of nahcolite crystals in Type 1 inclusions may be considered to be circumstantial evidence for their daughter nature. The apparent absence of nahcolite in some inclusions may reflect kinetic difficulties associated with nahcolite nucleation. We have noticed nahcolite nucleation after a cooling (freezing) cycle in a few inclusions.

The partial homogenization of the carbonic phase (Th(car)), almost always to a liquid ($L_{car}+V_{car}\rightarrow L_{car}$), ranges between –21.6 °C and 29.5 °C. Final melting of solid CO_2 (Tm(car)) occurs between –56.6 °C and –64.1 °C and the final clathrate dissolution Tm(Cla) occurs between 8.3 °C and 12.3 °C. Systematic variation of Th(car) was observed in individual quartz grains in some samples: grain cores usually show the highest Th(car) values, while the rims exhibit the lowest ones (Figure 3.7). The majority of the inclusions decrepitated shortly before their final fluid homogenization or immediately after this temperature. Some inclusions homogenized at 280 - 315 °C (Th(total), usually to vapor).

The observed dissolution temperature of nahcolite is within 80-90 °C. The calcite crystals trapped in the same inclusions do not dissolve until the inclusion decrepitation at about 255 °C.

Aqueous-carbonic inclusions in recrystallized quartz (Type 2 inclusions)

Type 2 inclusions (Figure 3.4) are predominantly hosted by recrystallized quartz (Q1N), typically in the form of sparse 3D-distributed inclusions, possibly of primary origin (with respect to Q1N). Type 2 inclusions also rarely form secondary trails in relic quartz (Q1Ur). Of all type 2 inclusions present in a sample, usually those hosted by quartz enclosed inside a sulphide matrix (pyrite and/or pyrrhotine) were the largest and thus the most suitable for microthermometry (Figure 3.2). Type 2 inclusions are always two-phase (aqueous liquid + carbonic vapor) at room temperature, are 3 to 70 µm in size (commonly 10-25 µm), and display regular or negative crystal shapes. The volume fraction of the aqueous liquid is 0.5 ± 0.2. Similarly to type 1 inclusions, one or more solid phases (nahcolite and/or carbonate) were identified and are present in 50-70 % of type 2 inclusions.

With respect to the density of the gaseous phase, two subtypes can be defined. High density type 2 (Type 2a): Tm(car) from -66.2 to -60.0 °C (however not measurable in every inclusion), Th(car) from -49 to +20 °C (always to L), Tm(Cla) from +10.8 to +18.5 °C. Low-density type 2 (type 2b): the gas content of inclusions did not freeze even down to -196 °C. Th(car) occurred from -80 to –11 °C (always to V) and Tm(Cla) from +14.3 to +19.5 °C. The inclusions probably correspond to the H2 type of the Kerkhof (1990) classification. Apart from the density, there is no difference in the size, shape, distribution and volume fraction of the aqueous phase of type 2a and type 2b inclusions. We are not able to separate type 2a and 2b inclusions by petrographic criteria alone.

Therefore we cannot exclude that they represent two separate and genetically different inclusion types.

The final homogenization /Th(total)/ could not be measured due to partial leakage of majority inclusions above 250 °C (Type 2a). In most inclusions, nahcolite remained in the inclusions up to their decrepitation without any evidence of dissolution. Only occasionally melting of nahcolite was observed between 84 °C and 90 °C. Important variations of the CO_2/CH_4 ratio were found in both subtypes. However, there is no correlation between this parameter and the inclusion distribution at the grain scale (in contrast to type 1 inclusions in Q1Ur).
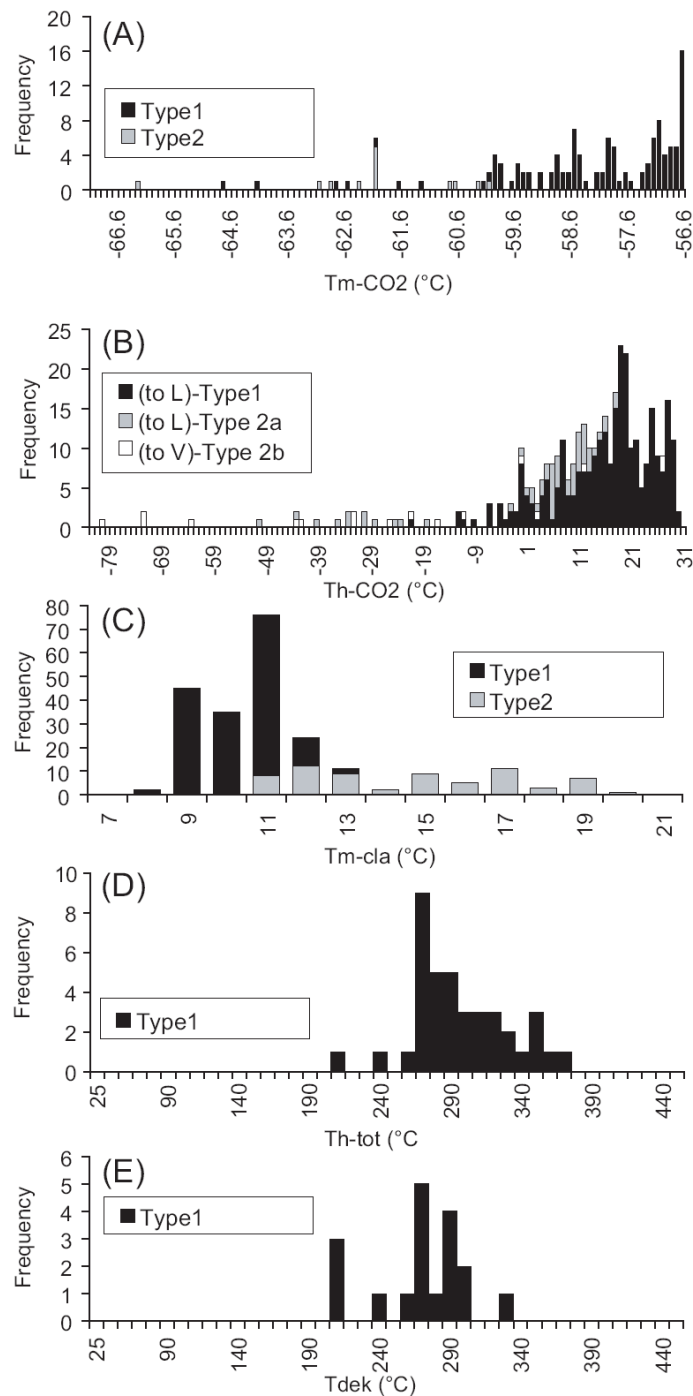
Figure 3.3: Histograms of microthermometric data of fluid inclusions from studied samples of the Main Vein.For detailed information about individual inclusion types, consult the main text, section 4 A) Melting temperature of the solid carbonic phase, B) Carbonic phase homogenization temperature, C) Temperature of clathrate dissociation, D) Total homogenization temperature (to the liquid state), E) decrepitation temperature.

Secondary aqueous inclusions (Type 3 inclusions)

Type 3 inclusions (Figure 3.4) are secondary and mostly form short intragranular trails in Q1Ur and Q1N quartz. Rare trails crosscutting grain boundaries between quartz Q1Ur and Q1N were also found. Inclusions are two-phase (aqueous liquid + aqueous vapor) at room temperature, mostly oval shaped and show homogeneous volume fraction of aqueous liquid (0.9 – 0.95). The temperature of the first/initial melting (Ti) is from -44 to -37.0 °C and the final melting of ice (Tm(Ice)) is between –4 and –1 °C, indicating that calcium is the main cation. There is no microthermometric evidence for the presence of gases. The total homogenization temperature (Th(total), usually to liquid) shows three maxima around 140, 180 and 260 °C.

Multisolid inclusions (Type 4 inclusions)

We have found numerous single-phase to multi-phase solid inclusions inside grains of recrystallized quartz Q1N (Figure 3.5). Occasionally, a volumetrically insignificant fluid phase was also identified. Some solids are very difficult to recognize or even to see by optical microscopy using a classical bright field. Very careful observation incorporating both plane and crossed polarization was necessary to observe their presence.

Type 4 inclusions (up to about 150-200 µm in size) usually consist of 3 to 10 solid phases. Based on their petrographic criteria, they are considered primary with respect to Q1N. The most frequent solid phases (identified using Raman microspectroscopy) are chlorite, calcium carbonate and albite, with a size that usually varies from 20 to 50 µm. Other solids (muscovite, rutile, pyrite, apatite, titanite, anatase ± some unidentified solids) occur randomly in different inclusions. It seems that there is a correlation between the number of type 4 inclusions present in the individual samples and the depth of the sample in the mine (i.e. distance to the granodiorite contact). The samples closest to the contact generally contain the highest number of multisolid inclusions. The fluid phase (gas, aqueous or both) mostly wets the surface of the solids, which makes its optical identification difficult and explains the absence of microthermometric data for these inclusions. However, H_2O, CO_2, CH_4, N_2, H_2 were identified using Raman microspectrometry (see section 6).

3.6   Raman Analysis

3.6.1   Gas analysis

Quantitative gas content measurements were performed on series of about 40 fluid inclusions representing the primary inclusions (Type 1) in the original quartz (Q1Ur) and the primary inclusions (Type 2) in the recrystallized quartz (Q1N). Selected representative measurements are presented in Table 2. Type 1 inclusions show (H_2O)-CO_2-CH_4 (± N_2, H_2S) composition with CO_2 as the main gas compound (98 to 89 mol% of gas content), CH_4 between 0.6 and 10 mol% and traces of N_2 and H_2S around 0.5 and 0.1 mol%, respectively. Type 2 inclusions contain traces of

C_2H_6, in addition to (H_2O)-CO_2-CH_4 ($\pm$ N_2, H_2S). The variations in the CO_2/CH_4 ratio are far more noticeable than in Type 1 inclusions. The CO_2 concentration varies from 95 mol% to 14 mol% and CH_4 varies from 5 mol% to 86 mol%. The concentrations of N_2 and H_2S are almost constant, around 0.5 and 0.1 mol%, respectively. C_2H_6 is constantly present at trace levels (0.1 mol%) and was identified from its Raman peaks (C-H stretching at 2955 cm^{-1} and C-C stretching at 990 cm^{-1}) (Figure 3.6). No evidence for precipitated carbon inside the inclusions was found by LRM. Type 4 inclusions: the composition of the volumetrically accessory fluid phase is highly variable - from nearly poor CH_4 in some cases to CH_4 – CO_2 mixtures (with or without H_2O). In some inclusions, H_2 was identified (Figure 3.6) in concentrations as high as 6 mol% (calculated using the standard methodology as described in Dubessy et al., 1989).

3.6.2   Evidence for HCO_3^- -rich fluids: Aqueous solutions and solids

The aqueous phase was also checked for the presence of polyatomic ions, such as CO_3^{2-}, HCO_3^-, SO_4, PO_4^{3-} and HS^-, which are Raman active, permitting their identification and analysis in the fluid phase (Dubessy et al., 1989). HCO_3^- in the aqueous phase of type 1 and type 2 inclusions was identified by its Raman peaks at 1013 cm^{-1} and 1362 cm^{-1} (Davis and Oliver, 1972; Frantz, 1998; Kruse and Franck, 1982; Oliver and Davis, 1973) (Figure 3.6) which were obtained even with small integration times (2 s), indicating a high concentration around 1 mole/litre. Dissolution of nahcolite at 80-90 °C indicates $NaHCO_3$ concentrations around 2 moles/litre $NaHCO_3$ (Haynes, 2003; Kogan et al., 1969; Vapnik and Moroz 2002). High-temperature Raman measurements also indicated the presence of HCO_3^- in solution after homogenization of selected inclusions at 326 °C. Calculation of the bicarbonate ion concentration from the Raman spectra is under development, so we were not able to quantify it precisely. These estimations suggest that HCO_3^- is probably the main anion in the solutions.

In spite of the fact that only 25-40% of the inclusions demonstrably contain nahcolite crystals, the authors assume the nahcolite is of primary (i.e. daughter) origin, based on the relatively constant crystal/inclusion volume ratio (see above) and on the Th(total) of the fluids over 300 °C which (most likely) excludes the presence of solid (i.e. trapped) nahcolite (Hoshino et al., 2006). The dissolution temperature of nahcolite in type 2 inclusions is highly variable, from 84-90 °C usually to above 250 °C, without any evidence of dissolution at this temperature. High dissolution temperatures can be interpreted either by high concentrations of bicarbonate, trapping of nahcolite together with the fluid, or metastability. According to previous data on fluid inclusions, dissolution temperature around 80 °C in type 1 inclusions and industrial dissolution plants of nahcolite deposits, the dissolution kinetics of nahcolite is sufficiently fast to reject metastability. If heterogeneous trapping is rejected, together with secondary origin of the nahcolite, concentrations of bicarbonates higher than 8 molal are expected (Haynes, 2003). It is worth noting, that pCO_2 higher than 100 bar are consistent with the stability of nahcolite with respect to trona (Liu and Fleet, 2009).
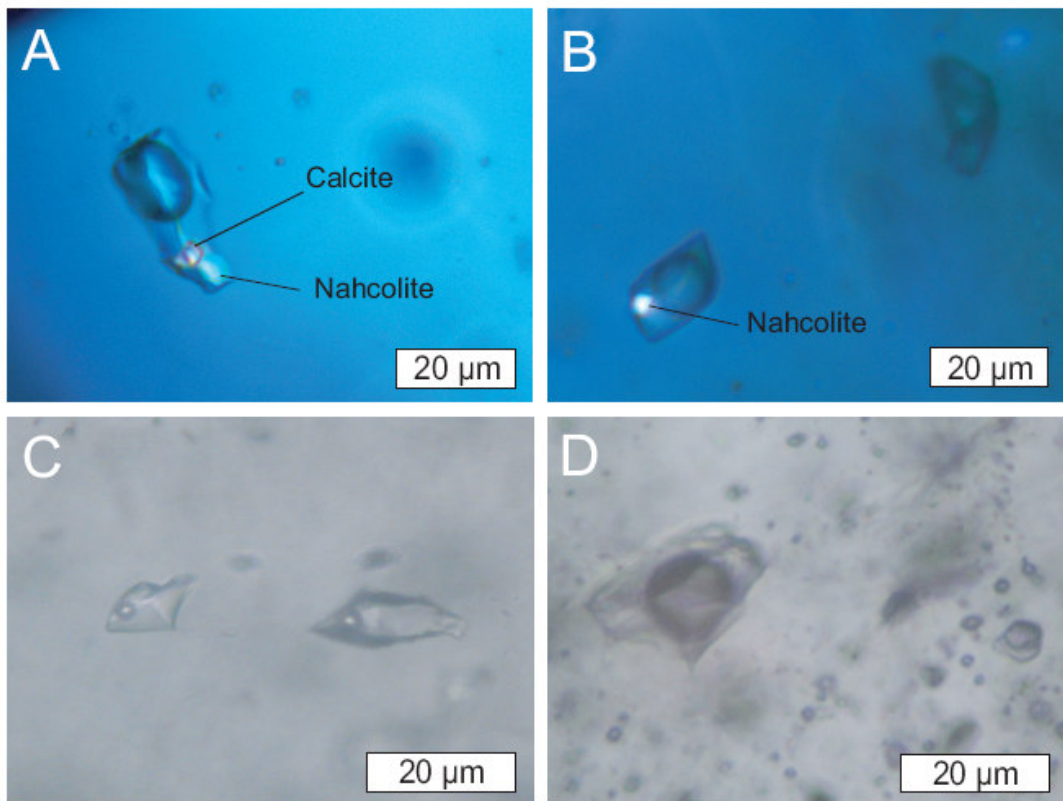
Figure 3.4: Photomicrographs of different types of fluid inclusions: (A) Type 2a primary aqueous-carbonic fluid inclusion from recrystallized quartz (Q1N) with trapped solids identified by Raman as nahcolite and calcite; (B) Type 2b primary aqueous-carbonic inclusion with nahcolite solid; crossed-polarized light; (C) Aqueous inclusions type 3; (D) Type 1 primary aqueous-carbonic fluid inclusions from relic quartz (Q1Ur).

Based on their Raman analysis, aqueous-only inclusions (type 3; secondary) also indicate the presence of HCO_3^- in the aqueous phase (possibly, lower than in type 1 and 2 inclusions Hrstka et al., 2010 – unpublished data). No nahcolite was found in type 3 inclusions.

The only fluids where the presence of bicarbonate was not identified are those trapped in multisolid (type 4) inclusions, possibly due to the small volume of aqueous solution resulting in a too weak intensity if the Raman signal.

It is mportant that no obvious evidence of the presence of bicarbonate can be obtained from the microthermometric measurements. The only indication could be the presence of the nahcolite crystals suggested by their birefringence in the inclusions. However, they are not present in all the identified inclusions with high bicarbonate concentrations and are totally missing in the secondary H_2O fluids with identically increased HCO_3^- contents. The eutectic temperatures and their comparison with the eutectic temperatures of the H_2O-$NaHCO_3$ and H_2O-$NaCl$-$NaHCO_3$ systems might be an indication but is sometimes inconclusive (Borisenko A.S., 1977; Huraiova et al.,

2002). The determination of the chlorine concentration cannot be based on modifications of the stretching band of water (e.g. Dubessy et. al., 2002; Mernagh and Wilde, 1989) in the absence of proper calibration. A software program developement is in progress for estimation of the bicarbonate concentration, combining microthermometric data, Raman analysis and thermodynamic modeling of the ice melting temperature (Dubessy et al., 2008).

3.7   Discussion

3.7.1   Summary of variability of the CO_2 and CH_4 contents

In our measurements, we have observed strong correlations between microthermometric data (Th(car), Tm(Cla) and the CH_4 content of the gaseous phase derived from LRMS spectra (e.g. correlation coefficient (r^2) between Th(car) and XCH_4 is 0.992; Figure 3.8 and Table 2). Thus, these correlations were used to infer the CH_4 content from microthermometric data for fluid inclusions, which were not analyzed by LRMS. Two major trends of measured and inferred CH_4 contents were recognized: one on the mine-scale (Figure 3.9) and one on the grain scale (Figure 3.7).

On the mine scale, in spite of some scattering of the XCH_4 content, type 1 inclusions show systematic enrichment in CH_4 contents with increasing depth/proximity to the contact with the granite (Figure 3.1, Figure 3.9). In addition to this large-scale variation, small-scale variability in the CH_4 contents in the gaseous phase was observed in the individual Q1Ur quartz grains (Figure 3.7). While the rims of large dark Q1Ur quartz grains show relatively high CH_4 values (up to 40 mol%), their centres are almost CH_4-free (down to 1 mol%).

Variation in the fluid composition in type 2 inclusions in Q1N quartz is far more obvious (13 to 94 CO_2 mol% in the gaseous phase); however, it lacks any systematic zonation either on the grain scale, or on the mine scale (i.e. random distribution of type 2 inclusions with variable CO_2/CH_4 ratios in Q1N quartz).
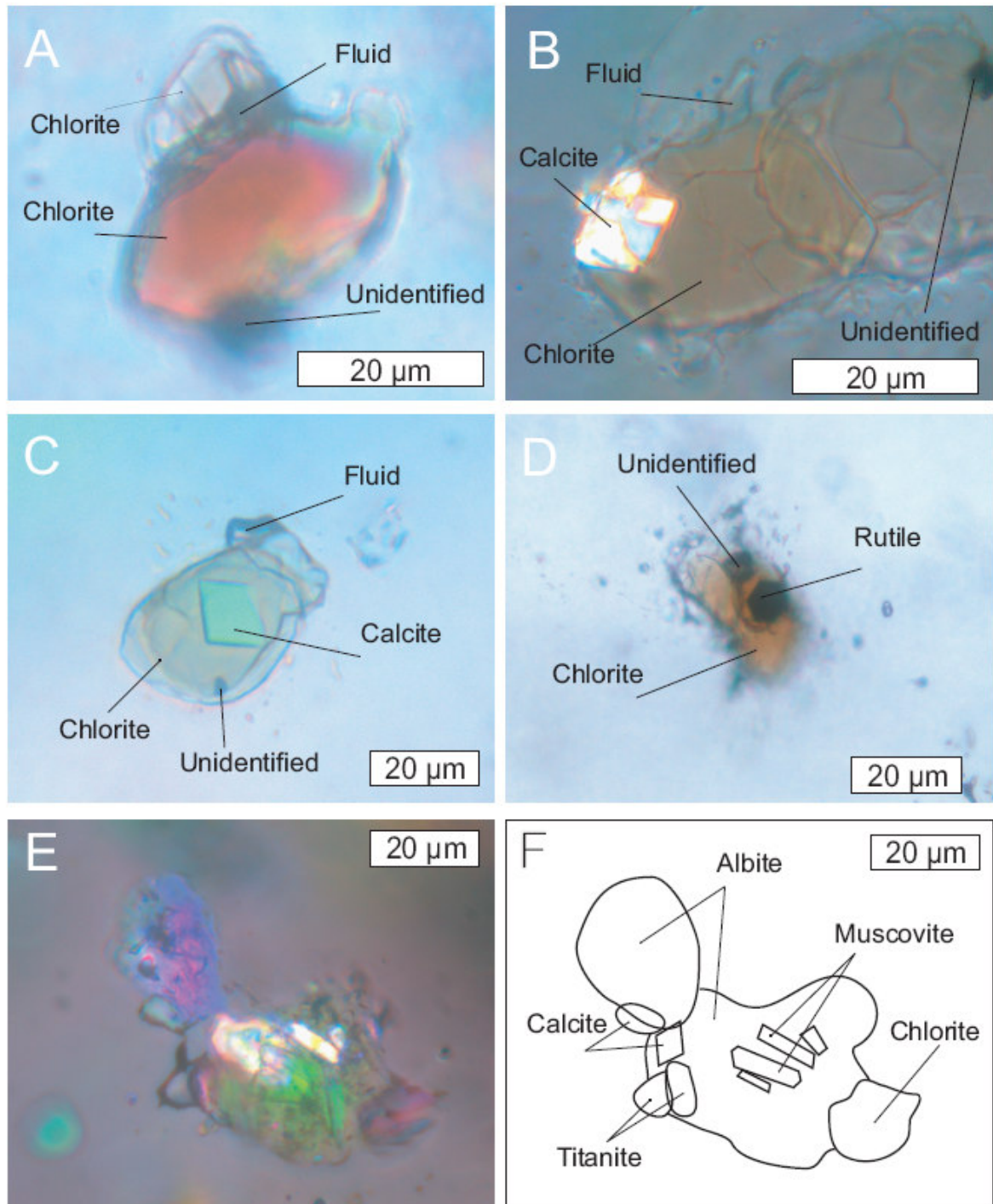
Figure 3.5: Photomicrographs of different types of multisolid inclusions (type 4) within the recrystallized quartz (Q1N). The marked phases were identified by Raman (LRMS).

3.7.2   Processes for CO₂/CH₄ variations in type 1 and type 2a inclusions

Significant variations in the CO_2 and CH_4 contents of natural fluids were already quoted at many localities/terrains worldwide. Potential primary processes responsible for these variations include: 1) complex hydrothermal history where different fluids passed through the vein under different conditions (e.g. Mernagh et al., 2004); 2) large fluctuations in the pressure (e.g. Robert et al., 1995; Zachariáš, 2002); 3) generation of CH_4 via interaction of aqueous fluids with graphite-bearing rocks at high temperatures (e.g. Huff and Nabelek, 2007); 4) partitioning of CH_4 into gaseous phases during boiling of a parent H_2O-CO_2-CH_4 fluid (e.g. Klein et al., 2000; Mernagh and Witt, 1994); and 5) fluid mixing between two or more fluids accompanied by fluid immiscibility (e.g. Diamond, 2001; Jia and Kerrich et al., 2000; Loucks, 2000; Yao et al., 2001; Zoheir et al., 2008). No convincing evidence was found for the active role of any of these mechanisms at the Libčice deposit. Fluid boiling can be rejected, based on the constant volume fraction of the aqueous phase in type 1 and type 2 inclusions, while minor variations in the bulk density of type 1 and type 2a inclusions point to negligible pressure fluctuations. Possibly the first mechanism could play a role, but this is difficult to prove.

Apart from the primary processes, significant CO_2/CH_4 variations can also be produced by post-entrapment re-equilibration/modification of the original inclusions (e.g. Mavrogenes and Bodnar, 1994; Morgan et al., 1993; Ridley and Hagemann, 1999). It is common practice to discuss fluid chemistry and post-entrapment modifications using ternary C-O-H plots (e.g. Bakker and Jansen 1993, Huizenga 2001). Two mechanisms should be considered: 1) H_2O diffusion; and 2) H_2 diffusion.

Ad H₂O diffusion: The effect of the addition or removal of water in a fluid of the C-O-H system can be easily described in the C-O-H triangle (Figure 3.10a-b). This evolution is a two steps evolution depending on whether graphite is present or precipitates. If we consider an initial fluid (IF) with CO_2/CH_4 >1, even if the fluid is not at equilibrium with graphite, its composition plots near the graphite saturation line. However, the first step of this evolution occurs along the straight line connecting the H_2O apex and the representative point of the initial fluid (IF) before H_2O modification. Water removal will result in a point representative of the new composition on this straight line outside the H_2O-IF segment. This trend is obviously not observed for the composition data (Figure 3.10c-d), as shown by the two solid arrows (Figure 3.10a). In addition, such process would result in rather low-density inclusions and require circulation of a water-poor fluid. The relatively constant volume fraction of the aqueous phase and the constant bulk fluid density exclude this hypothesis for type 1
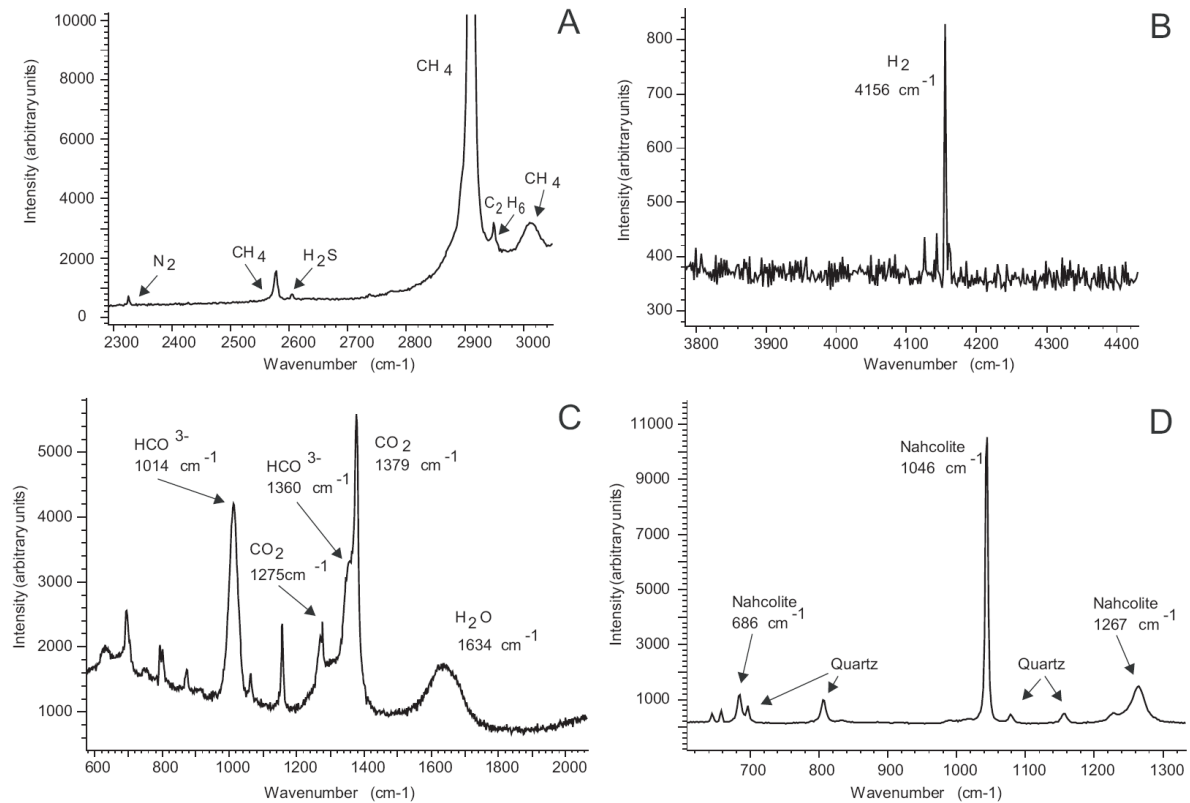
Figure 3.6: Raman spectra from different representative fluid inclusions: (A) Spectrum representing the typical gaseous speciation in a type 2a primary inclusion. Note the peak at 2950 cm^{-1} representing C_2H_6; (B) H_2 main peak at 4156 cm^{-1} from a type 4 inclusion; (C) Bicarbonate (HCO_3^-) in the aqueous solution of a type 1 primary inclusion. (D) Solid phase spectra identified as nahcolite from the type 2a inclusion.

and type 2a inclusions. If graphite reacts or precipitates with the new fluid, the evolution of the fluid composition lies along the intersection of the saturation line and the C apex. On the contrary, water diffusion in the inclusion will move the representative point in the C-O-H triangle towards the H_2O apex (Figure 3.10b). As the point resulting from this addition of H_2O is closer to the CH_4 point, the fluid will have a lower CO_2/CH_4 ratio. Let us note that, at the maximum water content, the CO_2/CH_4 ratio is close to unity. Further CH_4 enrichment cannot be produced by further H_2O addition. Finally, the addition of water would increase the bulk fluid density and volume fraction of aqueous liquid. These trends were not observed, and therefore we can rule out the hypothesis of addition of water to the inclusions.

Figure 3.7: Systematic variation of Th(car) (L+V=L) of type 1 inclusions (reflecting CH_4 content) in a relict quartz grain (Q1Ur); for more details consult the text or Fig. 3.8

Ad H_2 diffusion: When our bulk composition of type 1 and type 2a inclusions is projected on a C-O-H plot (Figure 3.10c-d), then all the data correspond to a quasi-linear trend pointing more or less towards the H_2 apex. For types 1 and 2a, the hydrogen diffusion into the inclusions is thus the best explanation for the observed trends. The slight deviation of the observed trend (symbols and dash-dotted line in Figure 3.10d) from the theoretical trend (dotted line in Figure 3.10d) can be explained by uncertainty in the estimation of the volume fraction of aqueous liquid (and consequently in the total amount of water). Although some sophisticated and precise methods (e.g. Bakker and Diamond, 2006; Hrstka, 2006a, 2006b; Stoller et al., 2007) of volume fraction estimation were developed, we have found them too complicated for routine analysis of large numbers of inclusions with complex shapes. Thus our calculation used a uniform value (0.5) for all the inclusions based on comparison with standard fill charts (Roedder, 1984; Shepherd et al., 1985), and on measurements of the inclusion long and short axes altogether with the bubble size (Zachariáš, 2002). An increase in this value from 0.5 to 0.55 only for the most CH_4-rich inclusions would position the data correctly along the calculated H_2-diffusion trend line.

The observed changes in fluid speciation in type 1 and type 2a inclusions suggest an increase in the H_2 content in inclusions up to values about 25 % higher than the original values (cf. numeric labels along the dotted line in Figure 3.10d). An increase in the hydrogen fugacity can be theoretically counterbalanced by generation either of CH_4 or of graphite, according to:

$$CO_2 + 4H_2 \rightarrow CH_4 + 2H_2O \qquad\qquad (3.1)$$

$$CO_2 + 2H_2 \rightarrow C + 2H_2O \qquad\qquad (3.2)$$
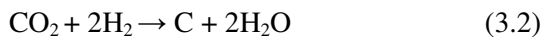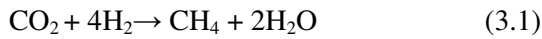
The absence of graphite in the inclusions can be explained as a failure in carbon nucleation due to kinetic barriers (Ziegenbein and Johanes, 1980). Therefore, reaction (1) is the only working mechanism of post-entrapment modification for type 1 and type 2a inclusions resulting from H_2 diffusion into the inclusion, producing a fluid oversaturated with respect to graphite.

Formation of type 2b inclusions

For the low-density type 2b inclusions, the question of their formation and/or post-entrapment modification is more complex than for types 1 and 2a. Type 2b inclusions form a short linear trend close to the H_2O apex, pointing towards type 1 and type 2a inclusions (Figs. 10c-d). In addition to the fluid composition (CO_2 : CH_4 : H_2O ratio), any model for generation/modification of type 2b fluids must also account for the very low density of the carbonic gaseous phase (~0.03 g/cm^3 for type 2b in contrast to >~0.6 g/cm^3 for types 1 and 2a). Theoretically, the following alternatives are possible:

1) Type 2b inclusions represent another generation of fluids, younger than H_2 diffusion-in processes that affected type 1 and type 2a inclusions. Thus, they should be secondary with respect to the quartz host (Q1N). However, we found no difference in the nature and distribution of type 2a and 2b inclusions in Q1N in general, except for sample Li392 where type 2a is missing. This sample possibly experienced the highest recrystallization (metamorphism).

Table 3.1: Q Summary of Raman and microthermometric data of type 1 and type 2 inclusions from Q1Ur and Q1N, respectively.

Sample	Inclusion	Spectrum	CO2 %mol	CH4 %mol	N2 %mol	H2S %mol	C2H6 %mol	Identified solids	Tm CO2	TmCLA	Th CO2	Mode	F-estimate
Q1Ur-quartz (Fluid inclusions Type 1)													
LiQ11A	30	c632	95.5	4.3	0.5	0.1			-57.8	10	20.3	L+V-L	0.5
LiQ11A	6	c642	93.4	6.0	0.5	0.1		nahcolite		10.1	18.0	L+V-L	0.5
LiQ11A	1	c643	95.3	4.4	0.5	0.1			-57.8	10.3	19.6	L+V-L	0.5
LiQ11A	3	c644	94.2	5.3	0.5	0.1			-57.9	9.8	21.1	L+V-L	0.5
LiQ11A	8	c645	94.0	5.5	0.5	0.1			-57.8	9.8	21.3	L+V-L	0.5
LiQ11A	34	c646	91.3	8.3	0.5	0.1			-58.8	10.4	17.1	L+V-L	0.5
LiQ11D	30	c647	92.2	7.6	0.5			nahcolite	-58.3	10	22.4	L+V-L	0.5
LiQ11D	2	c648	93.2	6.3	0.5	0.1				9.9	19.7	L+V-L	0.5
LiQ11D	7	c649	93.5	6.1	0.5				-58.1	9.9	19.9	L+V-L	0.5
Li11-2B	1	c687	95.5	4.0	0.5	0.2		-	-57.1	9.8	24.3	L+V-L	0.5
Li11-2B	3	c688	95.7	4.0	0.5	0.2		-		9.8	23.9	L+V-L	0.5
Li11-2B	32	c689	89.1	10.5	0.5	0.1		-	-59.4	11.2	14.2	L+V-L	0.5
Li11-2B	33	c690	87.1	12.6	0.5	0.1		-		12.3	8.2	L+V-L	0.5
Li253B	18	c693	92.0	7.4	0.5	0.1		-		10.1	19.4	L+V-L	0.5
Li253B	1	c694	91.6	8.2	0.5			carbonate	-58.4	10.4	17.6	L+V-L	0.5
Li253B	24	c695	91.5	8.2	0.5			carbonate		10.1	16.9	L+V-L	0.5
Li1118G-3	incl1	c708	98.6	0.6	0.6	0.2		-	-57.1	8.3	26.9	L+V-L	0.5
Li1118G-3	incl2	c707	98.6	0.7	0.5	0.2		-	-57.0	8.3	27.0	L+V-L	0.5
Q1N-quartz (Fluid inclusions Type 2)													
Type 2a													
L11-2A	1	c674	91.0	8.5	0.5			carbonate		11.1	13.8	L+V-L	0.5
L11-2A	2	c675	94.5	5.0	0.5	0.1		solid		11.0	19.7	L+V-L	0.5
Li253C-1	7	c685	82.7	17.0	0.5	0.1	0.1	-		12.2	7.2	L+V-L	0.5
Li253C-1	3	c686	83.0	17.0	0.5			-		12.0	4.7	L+V-L	0.5
Li253A-2	21	c696	61.3	37.0	1.4		0.1	-	-62	14.5	-16.7	L+V-L	0.5
Li253A-2	20	c697	79.5	19.0	1.4	0.1	0.1	-		12.4	3.3	L+V-L	0.5
Type 2b													
Li392A	40	c619	51.7	48.0	0.5					15.4	-26	L+V-V	0.6
Li392A	7	c620	44.7	54.7	0.5	0.1	0.1	carbonate?		17.1	-42	L+V-V©	0.6
Li392A	6	c621	69.9	29.8	0.5	0.1	0.1			14.8	-11	L+V-V	0.6
Li392A	25	c622	28.7	70.5	0.6	0.1	0.1	calcite - nahcolite		14.9	-63	L+V-V	0.6
Li392A	15	c623	53.5	46.0	0.5	0.1	0.1	nahcolite		15.8	-24	L+V-V©	0.5
Li392A	13	c624	45.6	54.2	0.5		0.1	calcite -		16.4	-43.5	L+V-V	0.6
Li392A	2	c626	13.9	85.5	0.5	0.1	0.15	nahcolite		16.9	-76	L+V-V	0.6
Li392A	4	c630	61.2	38.8	0.5					15.9	*-16*	*L+V-V*	0.5
Li392A	9	c631	53.6	46.3	0.5	0.1	0.1	calcite - nahcolite		14.3	-32	L+V-V	0.6

TmCO2   Final melting temperature of CO2
TmCLA   Final melting temperature of clathrat
ThCO2   Homogenisation temperature of CO2
mode   Mode of hologenization of CO2 (L,V,VC) liquid, vapor, critical
F-estimate Estimated volume fraction of liquid rim aqueous solution at room temperature

2) Type 2b originated by post-entrapment modification of type 2a inclusions. As discussed above, water diffusion out of the inclusion would lower the density of the gaseous phase at room temperature and the bulk fluid density. Alternatively, the decrease in the gas content in the inclusion as well of the density of the gas phase at room temperature is possible if the fluid is diluted by water before entrapment inside the inclusion. It is important that types 2a and 2b occur more or less randomly distributed within single Q1N grains (i.e. without the presence of identifiable secondary fluid inclusion trails). Therefore, a bulk diffusion process is excluded, as it would affect all the inclusions in a regular way. Any

process would therefore have had to operate selectively on a grain scale. Diffusion and/or migration via a system of irregular pore microchannels or microcracks is then likely.

3) Type 2 and type 3 inclusions were trapped during a single process: the initial fluid (type 2a) was at equilibrium with the graphite or carbon component with carbon activity below 1, with an initial H/O ratio close to 2. Then a supply of water (type 3) occurred without any reaction with the carbon phase due to the absence of equilibrium with the carbon phase. Fluid trapping (type 2b) happened continuously during this input of water.

4) Types 2a and 2b represent heterogeneous trapping of immiscible fluids from a parent fluid, such as type 1 unmixed at P-T-X conditions near its critical point; the properties of the two coexisting fluids could then be very similar.

At this moment we do not have convincing petrographic evidence for preference of any of these processes. Intuitively, we suggest the first hypothesis as the most probable, as it is the simplest.

3.7.3   *H_2 diffusion profile modeling (type 1 inclusions)*

Gold-bearing quartz veins at Libčice were subjected to contact metamorphism during the evolving stages of intrusion of the Central Bohemian Plutonic Complex (CBPC). The thermal effects of this episode can be found both on a mine scale (conversion of some hydrothermal carbonates into skarnoidal assemblages, presence of contact hornfelses, presence of lamprophyre xenoliths with remnants of original Q1-quartz gangue in the peripheral granite of the CBPC) and on hand scales (partial or complete recrystallization of quartz gangue). We suggest that the inward diffusion of hydrogen into Type 1 inclusions occurred during fluid-assisted thermal recrystallization of quartz gangue Figure 3.12.

Although an increase in the CH_4 content of originally CO_2-rich fluids has already been observed at many localities worldwide, the preserved intra-grain variability and especially the presence of concentric compositional profiles (Figure 3.11A) have not been reported yet. In order to interpret the intra-grain CO_2/CH_4 variability, we have performed modeling of the H_2 diffusion into quartz grains using the planar source equation (Howels, 1974 in Mavrogenes and Bodnar, 1994) and average diffusion coefficients from Kats et al. (1962). The input and output data of this modeling are shown in Figure 3.11.

Table 3.2: (Table 2) Summary of bulk composition and density data of type 1 and type 2 inclusions from Q1Ur and Q1N, respectively. Please note the high variation in the CO_2/CH_4 ratio.

Q1 Sample	Inclusion	Spectrum	VAPOUR-LIKE GAS MIXTURE (at 20 °C) Vm (cc/mol)	CO2	CH4	N2	C2H6	H2S	BULK FLUID INCLUSION Vm (cc/mol)	H2O	CO2	CH4	N2	C2H6	H2S	Na+	Cl-
Q1Ur-quartz (Fluid inclusions Type 1)																	
LiQ11A	30	c632	54.45	0.952	0.042	0.005		0.001	26.96	70.764	26.309	0.972	0.114	0.000	0.024	0.909	0.909
LiQ11A	6	c642	58.48	0.934	0.06	0.005		0.001	27.65	72.647	23.913	1.431	0.119	0.000	0.024	0.933	0.933
LiQ11A	1	c643	58.55	0.950	0.044	0.005		0.001	27.68	72.623	24.325	1.045	0.119	0.000	0.024	0.933	0.933
LiQ11A	3	c644	59.48	0.941	0.053	0.005		0.001	27.84	73.058	23.660	1.264	0.119	0.000	0.023	0.938	0.938
LiQ11A	8	c645	59.62	0.939	0.055	0.005		0.001	27.86	73.128	23.538	1.313	0.120	0.000	0.023	0.939	0.939
LiQ11A	34	c646	59.24	0.911	0.083	0.005		0.001	27.72	72.894	23.133	1.960	0.118	0.000	0.023	0.936	0.936
LiQ11D	30	c647	61.23	0.919	0.075	0.005		0.001	28.08	73.715	22.478	1.772	0.119	0.000	0.023	0.947	0.947
LiQ11D	2	c648	59.71	0.931	0.063	0.005		0.001	27.79	73.015	23.492	1.478	0.117	0.000	0.023	0.938	0.938
LiQ11D	7	c649	59.69	0.934	0.061	0.005			27.79	73.005	23.572	1.431	0.117	0.000	0.000	0.937	0.937
Li11-2B	1	c687	57.10	0.953	0.040	0.005		0.002	27.68	72.679	24.249	1.027	0.130	0.000	0.049	0.933	0.933
Li11-2B	3	c688	57.14	0.953	0.040	0.005		0.002	27.66	72.623	24.317	1.019	0.128	0.000	0.049	0.932	0.932
Li11-2B	32	c689	58.74	0.889	0.105	0.005		0.001	27.64	72.762	22.732	2.495	0.119	0.000	0.024	0.934	0.934
Li11-2B	33	c690	56.48	0.868	0.126	0.005		0.001	27.35	72.086	22.833	3.084	0.122	0.000	0.024	0.926	0.926
Li253B	18	c693	60.18	0.920	0.074	0.005		0.001	27.83	73.162	23.094	1.726	0.117	0.000	0.023	0.939	0.939
Li253B	1	c694	59.47	0.913	0.082	0.005			27.75	72.959	23.120	1.931	0.118	0.000	0.000	0.937	0.937
Li253B	24	c695	59.03	0.913	0.082	0.005			27.70	72.828	23.242	1.942	0.118	0.000	0.000	0.935	0.935
Li1118G-3	incl1	c708	54.90	0.986	0.006	0.006		0.002	27.63	72.442	25.301	0.171	0.174	0.000	0.052	0.930	0.930
Li1118G-3	incl2	c707	54.90	0.986	0.007	0.005		0.002	27.64	72.467	25.274	0.200	0.146	0.000	0.052	0.931	0.931
Q1N-quartz (Fluid inclusions Type 2)																	
Type 2a																	
L11-2A	1	c674	57.39	0.91	0.085	0.005			27.50	72.326	23.639	2.057	0.121	0.000	0.000	0.929	0.929
L11-2A	2	c675	58.95	0.944	0.05	0.005		0.001	27.72	72.733	24.076	1.182	0.118	0.000	0.024	0.934	0.934
Li253C-1	7	c685	58.29	0.824	0.169	0.005	0.001	0.001	27.53	72.705	21.227	4.035	0.119	0.024	0.024	0.934	0.934
Li253C-1	3	c686	56.76	0.826	0.169	0.005			27.35	72.227	21.679	4.117	0.122	0.000	0.000	0.927	0.927
Li253A-2	21	c696	54.01	0.614	0.371	0.014	0.001		26.80	71.700	16.760	9.322	0.352	0.025	0.000	0.921	0.921
Li253A-2	20	c697	57.47	0.794	0.19	0.014	0.001	0.001	27.41	72.493	20.678	4.582	0.338	0.024	0.024	0.931	0.931
Type 2b																	
Li392A	40	c619	810.91	0.516	0.479	0.005			29.38	95.314	1.507	0.724	0.007	0.000	0.000	1.224	1.224
Li392A	7	c620	878.64	0.447	0.546	0.005	0.001	0.001	29.39	95.551	1.223	0.762	0.007	0.001	0.001	1.227	1.227
Li392A	6	c621	678.50	0.696	0.297	0.005	0.001	0.001	29.38	94.690	2.331	0.535	0.009	0.002	0.002	1.216	1.216
Li392A	25	c622	2326.23	0.287	0.705	0.006	0.001	0.001	29.57	96.809	0.325	0.376	0.003	0.001	0.001	1.243	1.243
Li392A	15	c623	782.25	0.534	0.459	0.005	0.001	0.001	34.99	94.510	1.992	1.056	0.011	0.002	0.002	1.214	1.214
Li392A	13	c624	931.47	0.454	0.54	0.005	0.001		29.41	95.644	1.180	0.712	0.007	0.000	0.001	1.228	1.228
Li392A	2	c626	2266.36	0.139	0.854	0.005	0.001	0.001	29.55	96.880	0.162	0.467	0.003	0.001	0.001	1.244	1.244
Li392A	4	c630	680.92	0.609	0.386	0.005			34.92	94.006	2.551	1.017	0.013	0.000	0.000	1.207	1.207
Li392A	9	c631	1084.18	0.533	0.46	0.005	0.001	0.001	29.47	95.802	1.208	0.522	0.006	0.001	0.001	1.230	1.230
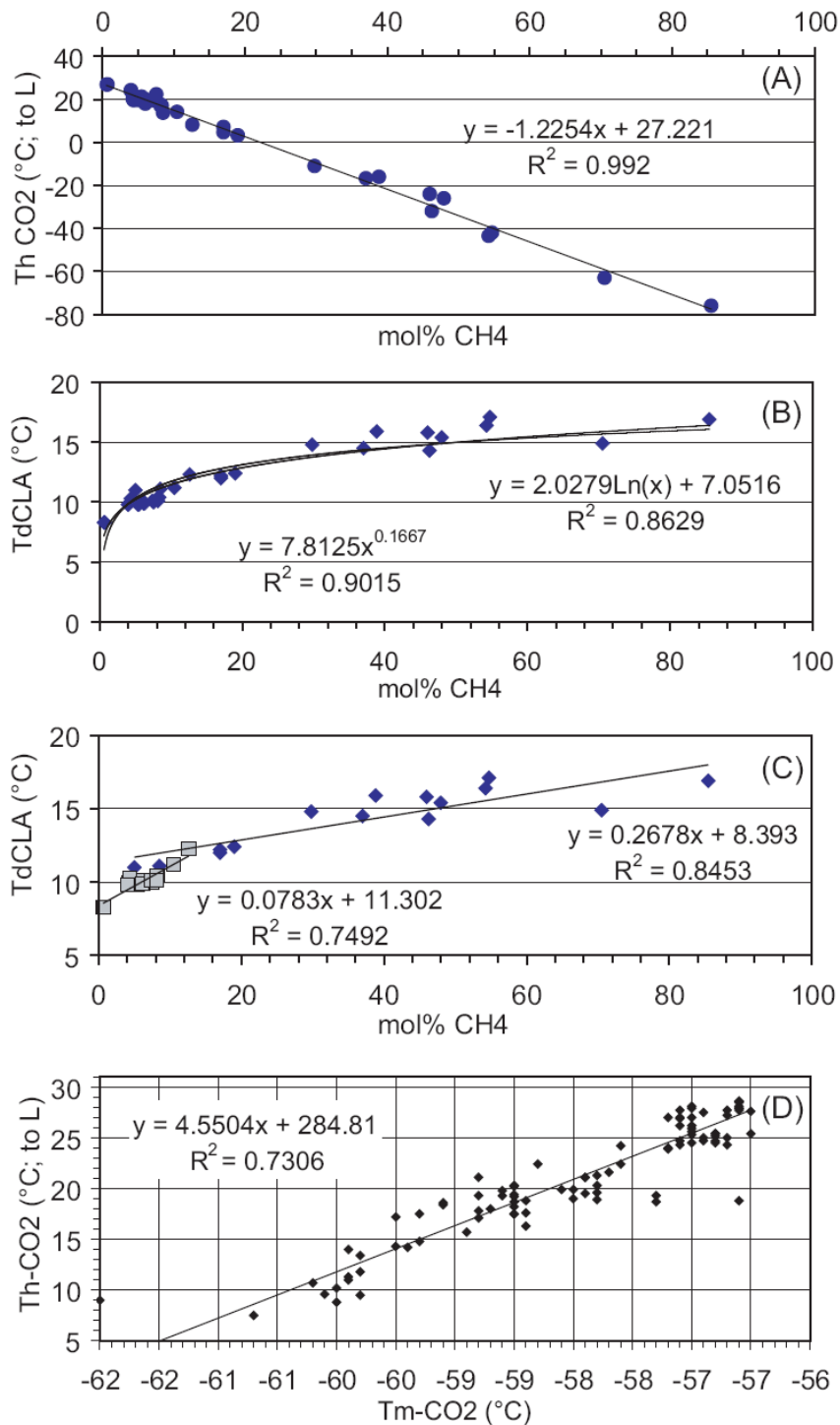
Figure 3.8: Correlation between microthermometric parameters and CH_4 content (mol%) of the carbonic phase determined by Raman spectroscopy. High values of regression coefficients indicate significant correlation not only between Th(car) and CH_4, but also between Tm(Cla) and CH_4.

In total, 8 core to rim profiles from two different Q1Ur grains (Figure 3.11A) were constructed. In the model we used the highest observed content of CH_4 in the gaseous phase of type 1 inclusions (40.1 mol % CH_4) to represent the fully re-equilibrated diffusion product. The relative diffusion efficiency is then defined as $100 * [X_{CH4}] / 40.1$. An average correlation between the CH_4 content (expressed in terms of the relative diffusion efficiency) and the distance of an inclusion relative to quartz grain core/rim is shown in line 1 of Figure 3.11B deduced from the analytical data. For the calculation, the H_2 diffusion is not considered below 300 °C, firstly because it is less efficient and secondly because chemical equilibrium between molecular species in the COH system is difficult to attain for kinetic reasons even below 400 °C (Morgan et al., (1992)). Diffusion calculations have been performed between 300 and 600 °C and the required diffusion time is estimated in a such ways that the theoretical diffusion profile (line 2 in Figure 3.11B) best fit the observed/intended profile (lines 2 in Figure 3.11B and Figure 3.11C).

A time of ~ 60 years was calculated to give a profile for which the relative efficiency of H_2 diffusion is higher than 90 % over the whole grain (line 3 in Figure 3.11B and Figure 3.11C) with the same temperature (400 °C) and same hydrogen fugacity gradients. On the other hand, a diffusion profile corresponding to 17 days shows that the inner part of the grain is almost unaffected by the hydrogen diffusion (lines 4 in Figure 3.11B and Figure 3.11C).

From the comparison of the calculations with the analytical data, it could be inferred that H_2 diffusion and fluid inclusion re-equilibration were rather fast processes (Figure 3.11C). They took from a few days (at 600 °C) to a few years (at 300 °C). For the most probable range (400-500 °C), the H_2 diffusion required only from 20 to 100 days. The time necessary for almost complete re-equilibration of the type 1 inclusions (i.e. disappearance of variations in the CO_2/CH_4 ratio on a grain scale) is approximately 5.5 years at 600 °C, and ~300 years at 350 °C for a H_2 fugacity gradient of 0.267 bar (i.e.: $pH_2^{external} = 1.334$ bar, $pH_2^{internal} = 1.067$ bar- based on the observed variation profiles). A higher gradient would result in faster diffusion and shorter times of equilibration; however, it would also produce more CH_4-rich fluid inclusions near the quartz grain rims than we have observed. A potential solution for this discrepancy would be partial resorption of the original quartz grain (i.e. inclusions now observed close to the grain surface originally occurred much deeper in the profile).

The limitations of this modeling must be borne in mind, as it does not take into account the 3D character of a grain, and the different ways in which the fluid could interact through cracks and micropores. However, generally speaking, there is good correlation between the real data and our model representing H_2 diffusion into the inclusions. This diffusion, with decreasing intensity towards the centre of individual relict grains, can easily account for the observed variations in CO_2/CH_4 for the Libčice deposit Q1Ur quartz.

In some MSI inclusions (type 4), up to 6 mol % of H_2 was found in the vapour phase, as found by the Raman analysis. Such high concentrations could be explained by the fact that the amount of CO_2 in the inclusion was too small to consume H_2.
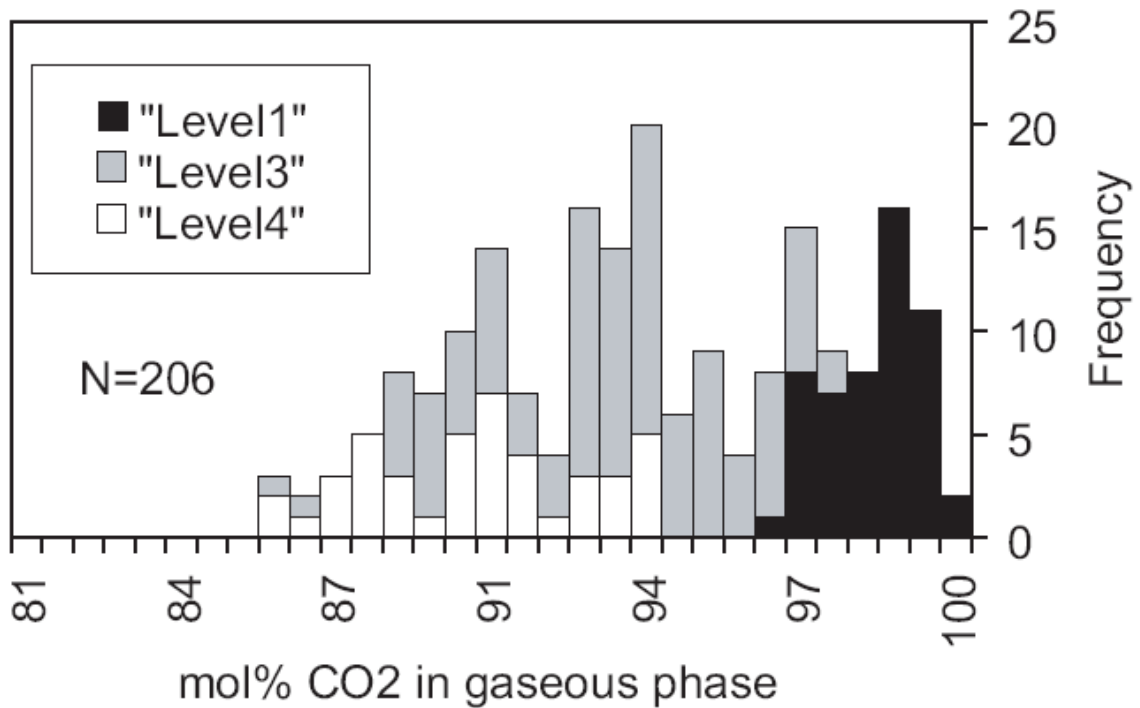
Figure 3.9: Variation of the CO_2 concentration in the gaseous phase of fluid inclusion populations across the Libčice mine (for the situation of mine levels see Fig. 3.1). Due to the fact that the gaseous phase of the studied inclusions can be well approximated by a binary system (CO_2-CH_4), the CH_4 content of inclusions at various mine levels can be easily calculated from the figure.

3.7.4   Source of H_2: Discussion

H_2 is known as a fluid component in many modern geothermal fluids, but only in quantities below 1 mol%. Higher concentrations can be expected only in the temperature range above 500 °C in fluids in equilibrium with graphite and with an O_2 fugacity near that of the Q-F-M buffer. However, H_2 content is expected to decrease below the detection limit for Raman analysis for C-O-H fluids during cooling at equilibrium (Dubessy at al., 1988; Dubessy et al., 1989).

H_2 in fluid inclusions has been reported previously in several cases; however, it was detected mostly by destructive (bulk) methods. Due to the fact that some of the measured H_2 could come from other mineral reactions during the sample analysis treatment, only the analysis of single

inclusions by non-destructive techniques can be taken as a true proof of the presence of H_2 in paleofluids. Only a few data have been published on the presence of hydrogen in fluid inclusions (Dubessy et al., 1988; Derome, et al., 2003; Peretti et al., 1992; Tsunogae and Dubessy, 2009).
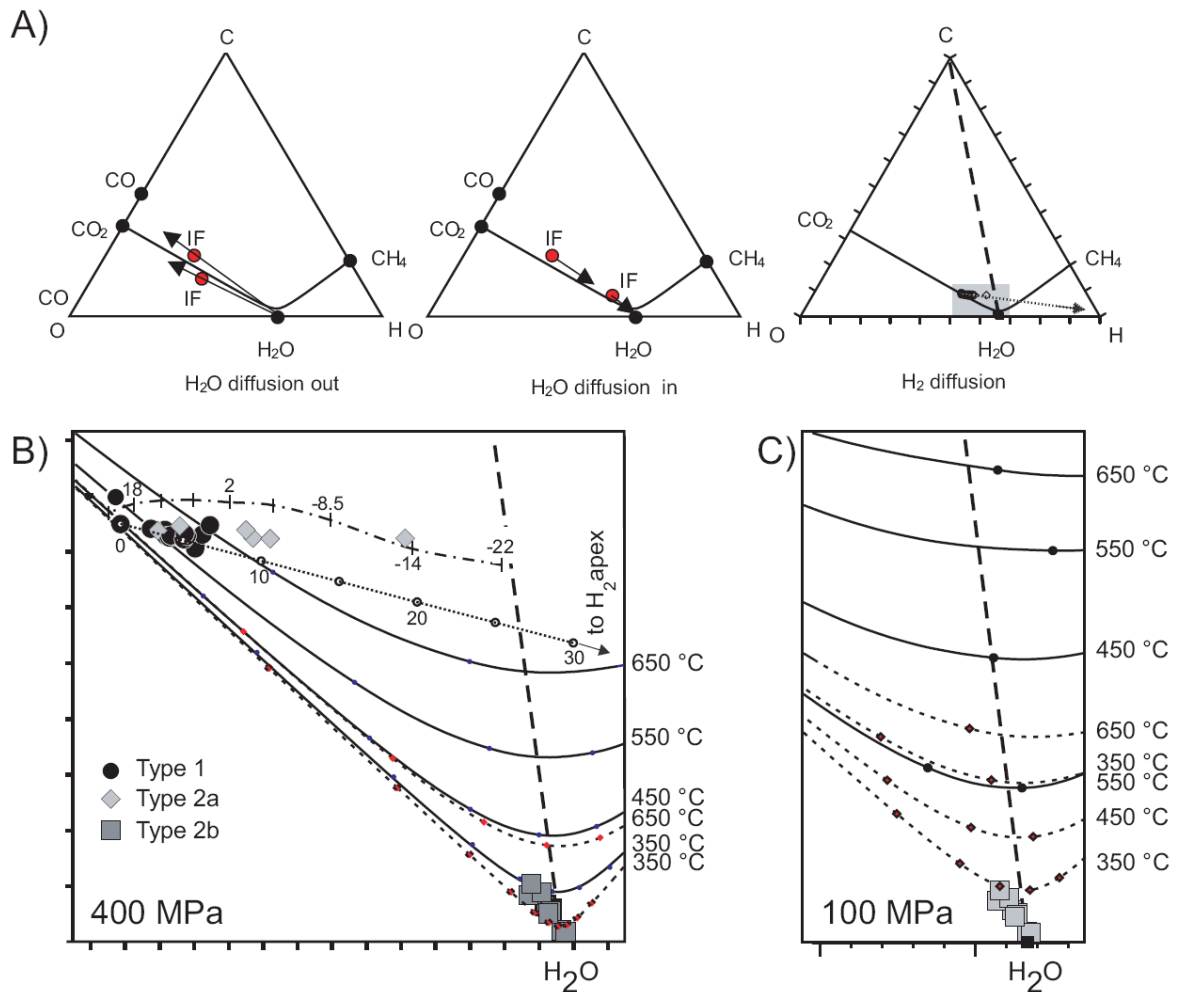
Figure 3.10: Composition of the studied fluid inclusions in the C-O-H system. A) Schematic system topology. (IF) marks the theoretical initial fluid as detailed in section 7.2. The solid curve represents the graphite saturation curve at 400 MPa, the dashed line marks the composition of the fluid produced by dehydratation reaction of graphite-bearing metapelites (i.e. constant atomic ratio H:O = 2, Connolly and Cesare, 1993). The shadowed rectangle shows the segment represented in figures B and C; B-C) Detail of compositional relationships at 400 MPa (B) and at 100 MPa (C). Solid lines represent the graphite saturation curves calculated for variable temperatures (indicated on the right-hand side), for variable oxygen fugacity, however, under the assumption of ideal graphite activity ($\gamma C = 1$). The short dashed lines represent the graphite saturation curves calculated at reduced graphite activity ($\gamma C = 0.3$). The straight dotted line with numeric labels 0, 10, 20 and 30 corresponds to the hypothetical evolution of the original inclusions that underwent inward hydrogen diffusion. Line points to the H2 apex. The numbers indicate the relative increase in hydrogen content in the inclusion fluid phase (in relative % with respect to the initial inclusion hydrogen content). Due to hydrogen diffusion, the most re-equilibrated inclusions are also the most CH4-rich ones. The theoretical trend line is more or less parallel (similar) to the natural trends observed within the

population of Type 1 (black solid circles), and Type 2a (grey diamonds) inclusions, both studied by Raman spectroscopy. Comparison of the data with the theoretical trend allows us to suggest an increase in the hydrogen content in the most re-equilibrated type 1 and type 2a inclusions by about 7 and 11 (19.5) relative %, respectively. An increase by about 25 relative % can be deduced based on the profile measured by Zachariáš (2002) (presented here by the dash-dotted curve labeled with the temperatures of partial homogenization of CO2 /to L; from +18 °C trough to –22 °C/). The composition of low-density type 2b (gray square) is markedly different. They all lie in the vicinity of the H2O projection. Their formation solely via hydrogen diffusion from type 1 inclusions is thus unrealistic. Probable alternatives for their formation are discussed in the text, section 9.3.

Three different mechanisms for the generation of H_2 have been reported in the literature (Bakker and Elburg, 2006; Dubessy at al., 1988; McCollom and Bach, 2009; Sleep et al., 2004). These are: water radiolysis (Dubessy at al., 1988); serpentinization (Peretti et al., 1992; Sleep et al., 2004), and fluid reactions with organic matter. In our case we can exclude the first two processes as uranium ore, or large mafic or ultramafic bodies are missing in the studied area.

Other likely mechanisms of hydrogen formation include phyllosilicates involving redox reactions (like $NH_4^+ \rightarrow H^+ + NH_3$ or $NH_4 \rightarrow \frac{1}{2} N_2 + 3/2 H_2$; e.g. Papineau et al., 2005). Such a reaction would require a high N_2 content in the fluid phase and an increase in both CH_4 and N_2 contents. There is no such evidence from the fluid inclusion data of this case study.

Organic matter is also an important gas-forming agent. Even if H_2 was reported in oil field waters and is most abundant in sediments with increased content of organic matter (Nechayeva, 1968), CH_4 and not hydrogen is the dominant gas formed by thermal maturation. According to Tissot and Welte (1987), the temperature required for CH_4 pyrolysis (conversion to H_2) is 500 to 1200 °C at pressures below 1 bar. These conditions are not common in the Earth's crust and are usually restricted only to volcanic areas with high thermal gradients and low pressures. However, in the absence of other possible mechanisms, the following cracking reaction of alkanes at high temperatures could be proposed for the formation of H_2: $C_nH_{2n+2} \Rightarrow (n-1)C_{(graphite)} + CH_4 + 2(n-1)H_2$. An oil which was submitted to intense alteration (thermal, radiolitic, oxidation) is transformed in pyrobitumen. Similar reactions could be written even with less hydrogen-rich organic compounds resulting in the formation of pyrobitumens, which are observed in the Lečice black shales. The hydrogen fugacity values of the external fluid used in the diffusion calculations show that it does not require the use an anomalously high H_2 content in the fluid. The isotope geochemistry should be elucidated to support such an origin.

3.7.5 *Bicarbonate-carbonate-rich fluids*

According to the review of Liu and Fleet (2009), nahcolite is found in various kinds of environments: evaporite ore beds (Dyni, 1996; Wang et al., 1991), concretions in sedimentary

basins, hot springs and saline lake precipitates, and fluid inclusions from metamorphic rocks. Nahcolite is also closely associated with carbonatitic volcanoes and was reported as an alteration product of natrocarbonatitic lavas (e.g. Zaitsev and Keller, 2006).

The probable source of nahcolite/HCO_3^- in our system is not clear. Nahcolite has not been found in the different rocks, but this could result from its subsequent dissolution due to its high solubility. Nahcolite is present in Green River oil shales (e.g. Reitsema, 1980) and could have been present in the organic carbon-rich Neoproterozoic sediments (e.g. Reitsema, 1980). Therefore, these Libčice sediments could have been the origin of both high concentrations of bicarbonate fluids and of the production of H_2-rich fluids by circulation of hot fluids. However, the hypothesis of Na-metasomatized (Na-altered) metavolcanites ("paleodacite to paleorhyolite") cannot be excluded. The latter have the highest Na content of all the studied rocks, based on the QEMSCAN analysis (Hrstka, 2010 – unpublished data). The two origins are not necessarily mutually exclusive.
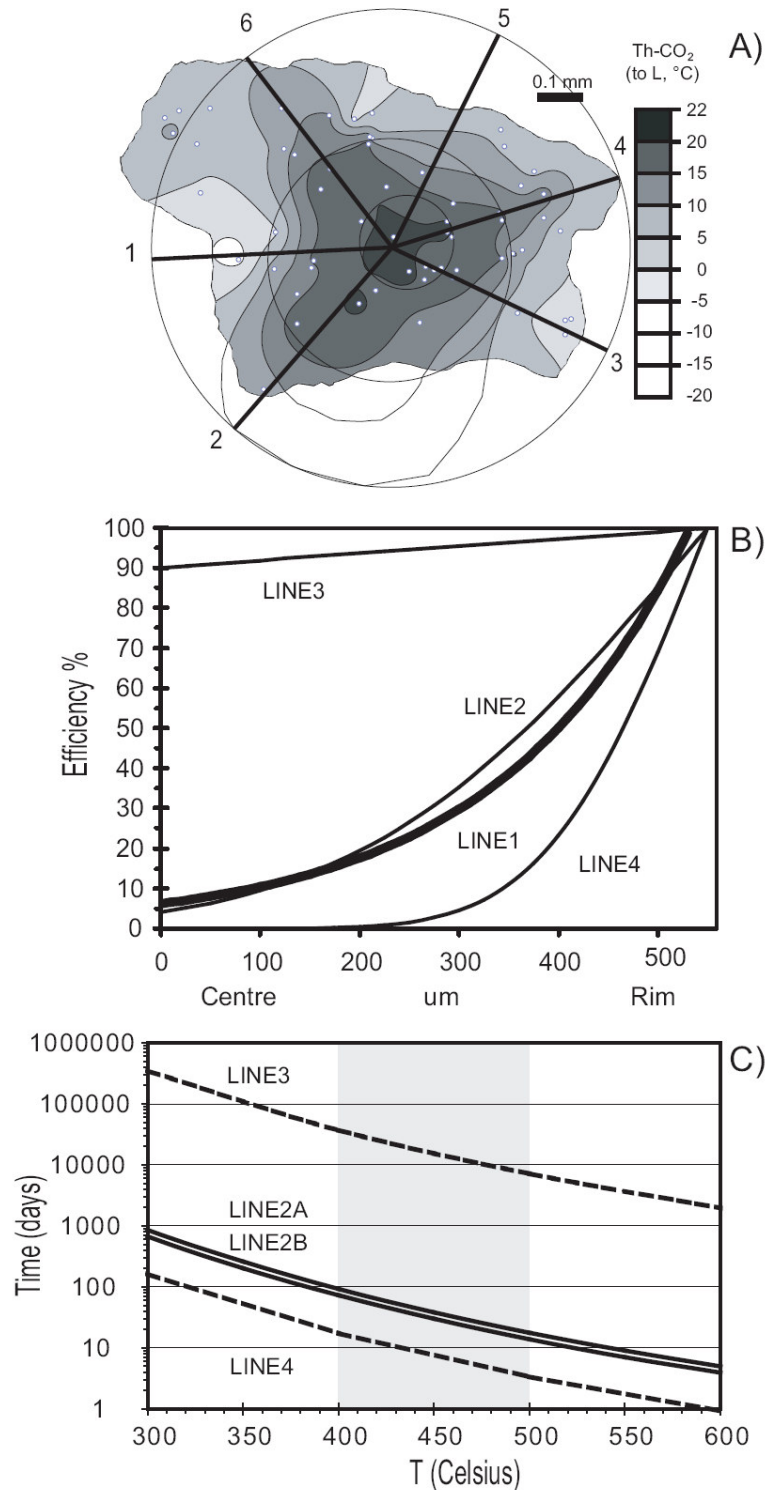
Figure 3.11: Hydrogen diffusion modeling in quartz using a planar source equation (Howels 1974 in Mavrogenes and Bodnar, 1994) and the diffusion coefficients (D; cm^2s^{-2}) of Kats et al., (1962): A) grain with observed Th(Car) variations (i.e. CO_2/CH_4 variations in a gas phase). The profiles that were used in construction of an "average diffusion profile" (line 1 in fig. B) are labeled 1 through 6. B) The relative H_2 diffusion efficiencies vary with the distance from the grain surface/core calculated for temperature 400 °C, a

H_2 fugacity gradient of 0.267 bar, diffusion coefficient of $D = 5.25*10^{-11}$ cm^{2}s^{-2} and for the grain shown in figure A. Line 1 represents the average of the measured compositions on the individual profiles converted to the relative efficiency of H_2 diffusion. Line 2 represents the ideal fit of the observed data (line 1) with the planar source equation and resulted in diffusion lasting ~70 days. For line 3, the duration was set to ~60 years, in order to achieve more or less complete diffusion over the whole grain profile (i.e. relative efficiency >90%). Line 4 represents an opposite alternative to Line 3. Time was set to ~17 days in order to minimize diffusion in the broader zone around the grain core (0-250 μm) and keep it at a maximum at grain rim. C) Times required to reach the various H_2 diffusion scenarios from (B) under temperatures ranging from 300 to 600 °C. The line indices are same for both figures (B and C).

3.7.6   Origin of multi-solid inclusions (type 4) in quartz

Numerous, almost fluid-free multi-solid inclusions were frequently identified in the Q1N quartz and rarely found in Q1Ur. They are composed of barely soluble minerals, such as albite, chlorite, muscovite, rutile, pyrite, apatite, titanite and anatase. The formation of these solids as daughter phases from a hydrothermal fluid is therefore highly improbable. Although our multi-solid inclusions resemble melt inclusions, their occurrence within the hydrothermal vein gangue makes this origin less probable.

We presume that the multi-solid inclusions represent relicts of mineral phases primary present along grain boundaries of the Q1 quartz (before its recrystallization) and, to a minor extent, phases formed during thermal recrystallization of the gangue. From this point of view, it is noteworthy that multi-solid inclusions are most abundant in samples from the immediate vicinity of the granodiorite contact. Therefore, they probably had relatively high formation temperatures (>450 °C). The presence of H_2 in type 4 inclusions further implies the importance of hydrogen formation and diffusion during the contact metamorphism in our region.

3.7.7   The presence of C_2H_6

The presence of C_2H_6 was sporadically reported in orogenic gold terrains (Neumayer and Hagemann 2002) and in reduced carbonic fluids from middle to lower crustal level rocks (Graney and Kesler, 1995; Polito et al., 2001; Tsunogae and Dubessy, 2009). C_2H_6 is generally not expected for fluids with formation conditions such as those at the Libčice gold mine. According to Klein and Fuzikawa (2010), the presence of C_2H_6 and other light hydrocarbons in the fluid inclusions from the gold–quartz vein deposits has been documented in a few cases in the Canadian Abitibi belt (Graney and Kesler, 1995), in the Barberton greenstone belt of South Africa (Bray et al., 1991; De Ronde et al., 1992), and in the Yilgarn block of Western Australia (Polito et al., 2001). The source of these hydrocarbons appears to be the reduction of CO_2 to CH_4 and C_2H_6 or interaction of fluids with organic matter (Beeskow et al., 2006; Potter et al., 2004). The formation of CH_4 and C_2H_6 by abiotic versus biotic processes was also discussed by Whiticar (1999): thermogenic gases typically have C1/(C2+C3) < 100, which is the case for our type 1 inclusions.

In our case, the absence of C_2H_6 in the early metamorphic fluids (type 1) and its presence in the late fluids (type 2) implies the origin of C_2H_6 by the combined effect of fluids and heat on the organic-rich Neoproterozoic sediments at the time of the CBPC intrusion.
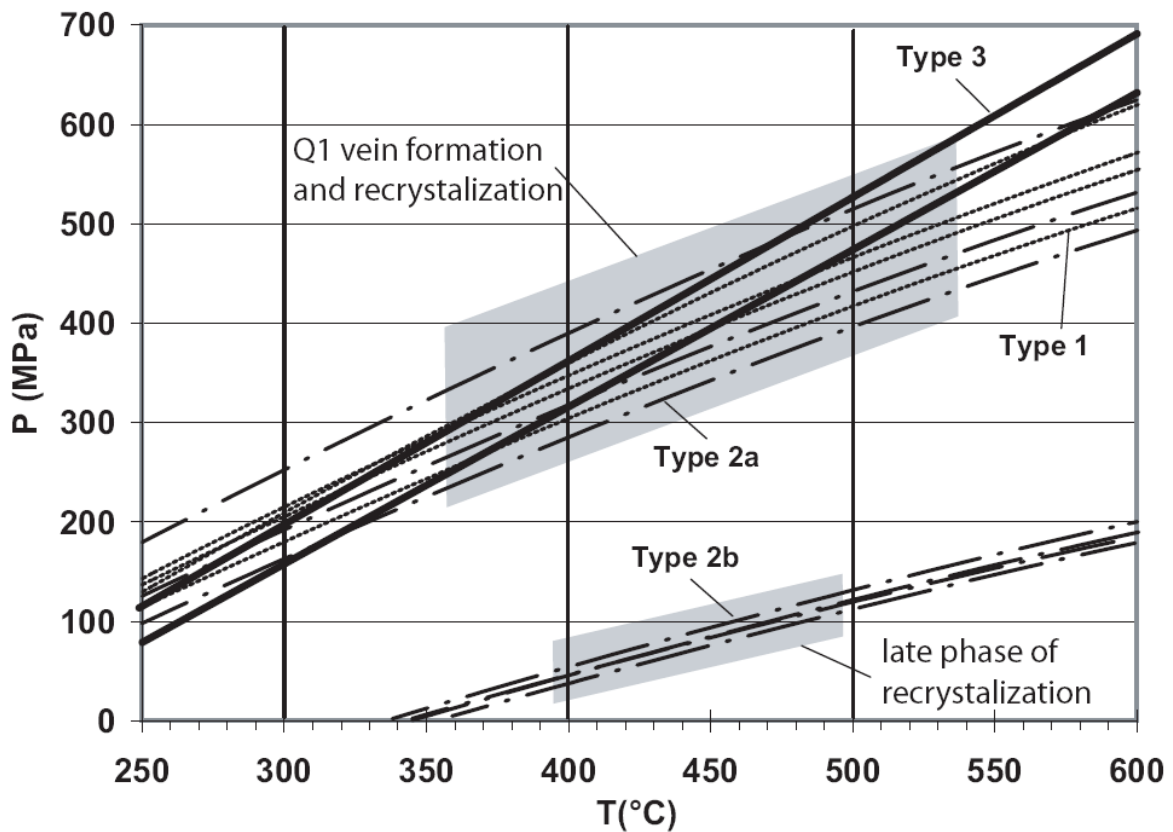
Figure 3.12: Isochors estimation of P/T conditions at the Libčice gold deposit inferred from the data in this study and in Zachariáš, 2002; Zachariáš et al., 1997; Sejkora et al., 2009.

3.8   Conclusions

This study reports the unusual composition of fluid inclusions from an orogenic-type gold deposit at Libčice in Central Bohemia. Firstly, extreme variations in the CO_2/CH_4 ratio of the gaseous phase of fluid inclusions occur both on a grain and on a mine scale. Secondly, the presence of bicarbonate-rich (HCO_3^-) paleofluids as well as identified hydrogen (H_2) and ethane (C_2H_6) make the processes at the deposit quite unique, compared to other orogenic-type gold deposits.

The Libčice deposit is also exceptional for well-documented crosscutting relationships between the gold-bearing quartz veins and between the late intrusive phases of the Central Bohemian Plutonic Complex. Quartz veins, including the gold mineralization, underwent contact metamorphism, with an intensity that rapidly decreased along the vein strike (with the distance from the contact with the peripheral granite). Quartz gangue itself underwent total to partial solid-state recrystallization. Some of the observed unusual fluid compositions are attributed to this process.

Four types of primary fluid inclusions were observed in the gangue of the main Libčice vein. Type 1 inclusions exhibit pronounced variations in the CO_2/CH_4 ratio in the gaseous phase, while the bulk content of water remains more or less stable. An increase in the CH_4 content from 0-4 mol% to about 40 mol% was observed along the core to rim traverse in some relic grains of the original quartz (Q1Ur). We attributed all these observations to the influence of inward hydrogen diffusion during fluid-assisted solid-state recrystallization of the quartz gangue.

Type 2 inclusions are also aqueous-carbonic, however slightly more water-rich. They exhibit even more extreme variations in the CH_4 content (from 13 to 94 mol% in the gaseous phase) than type 1 inclusions and the unexpected presence of C_2H_6 (0-0.2 mol%). They can be subdivided into two subtypes, differing particularly in the gaseous phase density. They were probably formed during thermal recrystallization of the quartz gangue. They were also influenced by devolatilization of the organic-rich Neoproterozoic shales (Libčice member).

Type 3 inclusions are only secondary and aqueous.

Type 4 inclusions are multi-solid, with only a Raman-detectable fluid phase, with many silicate phases and with up to 6 wt. % of free hydrogen. They most likely represent the relicts of some mineral phases primarily present in Q1 gangue and recrystallized to the present form during the thermal influence of CBPC intrusion.

To best of our knowledge, this study reports the first appearance of Raman measurable HCO_3^- in the liquid phase of natural fluid inclusions from an orogenic-type gold deposit. Many of the type 1 and type 2 inclusions also host crystals (daughter solids) of nahcolite and/or calcite. The estimated concentration of HCO_3^- in the fluid phase may be as high as approx. 20 wt. %.

Apart from the high concentration of bicarbonate related to almost all the fluid types, the general characteristic of the Libčice deposit are similar to those of other orogenic-type deposits in the Jilove belt (H_2O-CO_2±CH_4 low to moderate salinity fluids with probable trapping temperature of 300-450 °C). The influence of different host-lithology combined with the thermal (and fluid) effects of late magmatism seem to be the key parameters for the unusual bicarbonate-rich (HCO_3^-) paleofluids and for the presence of H_2 and C_2H_6 in the studied inclusions.

Diffusion modeling of the CO_2/CH_4 ratio variations along the core to rim traverse in the relic grains of the original (unrecrystallized) quartz suggests short duration of the thermal effects related

to the intrusion of Libčice peripheral granite. Hydrogen diffusion into the fluid inclusions is the main mechanism responsible for the observed variations in CH_4 in the type 1 fluids both on a mine scale and on a single grain scale.

3.9   Acknowledgements

4. POTENTIAL CONCENTRATION MEASUREMENTS OF HCO_3^- AND PH ESTIMATES IN NATURAL FLUID INCLUSIONS BY RAMAN SPECTROSCOPY: A CASE STUDY FROM THE LIBČICE GOLD DEPOSIT (ARTICLE 2)

Tomáš Hrstka[1], and Jiří Zachariáš[2]

[1] *Institute of Geology AS CR, v.v.i., Rozvojová 269, CZ-165 00 Prague 6 – Lysolaje, Czech Republic E-mail: **hrstka@gli.cas.cz***

[2] *Charles University in Prague, Faculty of Science, Institute of Geochemistry, Mineralogy and Mineral Resources, Albertov 6, Praha 2, CZ-128 43, E-mail: zachar@natur.cuni.cz*

Status: In preparation

Abstract

The unusual fluid inclusion composition has been reported earlier at the Libčice orogenic gold deposit (Zachariáš, 2002 and Hrstka et al., 2011). Bicarbonate (HCO_3^-) rich H_2O-CO_2 ± (CH_4, N_2, H_2S, C_2H_6) and H_2O fluids were recorded. Earlier Raman study revealed the presence of elevated concentrations of HCO_3^- in all paleofluid generations from the main gold-bearing quartz vein. This paper reports on high-temperature Raman measurements made in order to confirm the proposed anomalously high concentrations of bicarbonate in the Libčice paleofluids. Also, first attempts to validate the individual Raman peaks for future quantitative analysis of HCO_3^- in aqueous-carbonic paleofluids and potential pH calculation were performed on these natural fluid inclusions. pH-controlled equilibria of $(HCO_3^-)/(CO_3^{2-})$ (with main Raman peaks at about 1017 cm^{-1} and 1064 cm^{-1}, respectively) were used in this respect. The high concentration of HCO_3^- in the fluids was confirmed by the presence of a peak at 1014 cm^{-1} and at 1360 cm^{-1} even at temperatures above total homogenization (Th tot). Proportions of the peak integrated areas were measured in order to receive the relative concentration of HCO_3^- in the aqueous solution. For the low-temperature measurements the peak area ratio $RC_{HCO3}=A_{1014}(HCO_3^-)/((A_{1640}(H_2O)-A_{1620}$ (Quartz)) formula was suggested as the most practical while the peak height ratio ($RC_{HCO3}=I_{1360}(HCO_3^-)/((I_{1640}(H_2O)-I_{1620}$ (Quartz)) seems more applicable for temperatures above 100 °C. The behavior of quartz matrix and the possibility of spectral subtraction of quartz from solution spectra were tested to overcome the peak overlap of quartz and CO_3^{2-} at around 1066 cm^{-1}. Based on our results, the Libčice paleofluids were estimated at pH 7–8.5. The extremely high variation in relative peak intensity of the monitored part of quartz spectrum was confirmed even within a single grain. Other peak parameters were tested for establishing the best potential calibration strategies for quantitative Raman measurement of bicarbonate in natural fluid inclusions both at room and at elevated temperatures. This research is important for the future pH calculation development and high-temperature Raman spectroscopic study of fluid inclusions/paleofluids.

4.1   Introduction

Raman spectroscopy is now a well-established technique for the study of fluid inclusions and paleofluid chemistry in general (e.g., Burke, 2001; Dubessy et al., 1989, 1992). It can be used for non-destructive calculations of the gas composition content (Dubessy et al., 1989; Wopenka and Pasteris, 1986), study of polyatomic ions in solution (Boiron et al., 1999; Dubessy 1983; Rosasco and Roedder, 1979) and other applications like salinity determination and gas clathrate classification (e.g., Mernagh and Wilde 1989; Dubessy et al., 2002; Baumgartner and Bakker, 2009). For further reading on Raman application in fluid inclusions research the reader is referred to excellent reviews (e.g., Burke, 2001; Burruss, 2003) and references therein.

The importance of HCO_3^- fluids in geosciences in general is obvious for the low-temperature systems below 100 °C (Stumm and Morgan, 1996). Above this temperature, however, the prevalence of Cl^- and other anoins is reported for hydrothermal paleofluids (Kruger and Diamond, 2001 and Frantz, 1998). Majority of previous studies also suggest acidic rather than alkaline fluids. Nevertheless, the presence of bicarbonate ions in some environments is potentially more important than believed previously (Vapnik and Moroz, 2002). In the last few years, the occurrence of nahcolite has been reported from aqueous-carbonic fluids related to different deposits. The presence of this mineral in inclusions might be a sign of elevated bicarbonate concentrations. However, HCO_3^- has not been directly measured and quantified by Raman spectroscopy in naturally occurring inclusions yet.

Quantitative calculations of the concentration of Raman active ions such as CO_3^{2-}; HCO_3^-; SO_4; PO_4^{3-}; HS^-, can lead us to important information about pH, $f_{O2,}$ f_S fugacity as well as other parameters of the paleofluid (Dubessy et al., 1989). While the concentration of SO_4; HS^- polyatomic species in natural paleofluids was measured and even quantified for some species (Dubessy et al., 2002), no similar data has been reported for HCO_3^- from natural fluid inclusions. The presence of bicarbonate in fluid inclusions was predicted but not confirmed due to the overlap of the Raman peaks of HCO_3^- with the peaks from the host minerals reported (Burke, 2001; Dubessy et al., 1989). This paper represents one of the first Raman studies of bicarbonate in natural aqueous-carbonic paleofluids from quartz and one of the first attempts on their potential quantification in order to calculate the pH. The high-temperature measurements of the HCO_3^- -rich system were also performed in order to help us in the current effort to use Raman spectroscopy for homogenized fluid inclusions (e.g., Azbej et al., 2007; Chen and Zheng, 2004; Pironon et al., 2000; Dubessy et al., 2001; Martinez et al., 2004).

The Libčice deposit is located in a contact zone of the Central Bohemian Plutonic Complex (CBPC) and belongs to the group of orogenic metallogenic unit of the European Variscan belt. This deposit is situated within a metallogenic zone with numerous gold deposits like Mokrsko, Petračkova hora, Jílové, Kasejovice, Belčice (Boiron et al., 2001; Zachariáš, 2002; Zachariáš et al., 1997, 2001).

Mineralogy of the deposit was reported previously (Litochleb and Šrein, 1994; Šrein et al., 1995; Zachariáš, 2002; Sejkora et al., 2009). The content of sulfides is generally low (less than 5%). The main sulfide is pyrrhotite followed by arsenopyrite, pyrite, chalcopyrite and marcasite. Löllingite is rarely found in the form of inclusions in arsenopyrite. Native gold is present in two generations (gold-I with 2–5 wt. % Ag and younger gold-II with 12–13 wt. % Ag). Gold-I is the dominant phase and is commonly associated with Bi-Te-S phases. Occasional presence of various silicates – pyroxene (salite), grossular, titanite and wollastonite – was also reported from the Main vein (Šrein et al., 1995). Fluid inclusions were previously studied by Zachariáš, 2002 and Hrstka et al., 2011.

The Libčice ore district consists of a single dominant quartz vein ("the Main vein") and of several other smaller veins (uneconomic), parallel or perpendicular to the Main vein. The Main vein is about 400 m long, usually 0.2–0.4 m, locally max. 1.5 m thick, it strikes W-E and dips 70–90° to N/S. Quartz gangue of the Main vein is formed by coarse-grained, white to greyish quartz (denoted as Q1) demonstrating different degrees of thermal recrystallization. Younger quartz veins (denoted as Q2) are associated with E–W- and/or N–S-striking lamprophyre dykes in a broader area, however, they are relatively gold-poor, and significantly less thick. Minor and mineralization-free are quartz veinlets (denoted as Q3) within fault calcite gangue. In this paper, only data for the Main vein (Q1) are presented and discussed.

In order to discriminate microtextures of the Main vein quartz gangue, we denoted the remnants (i.e., relicts) of original unrecrystallized quartz as Q1Ur, while the quartz that resulted from recrystallization of Q1 is herein referred to as Q1N ("neoformed quartz"). Generally, the Q1N quartz dominates the gangue, constituting 60–80 % (Hrstka et al., 2011).

Microstructures of the Main vein quartz gangue indicate a progressive recrystallization with remnants of original quartz crystals preserved as "relict" grains (Q1Ur) and matrix represented by recrystallization-related "neoformed" grains (Q1N).

Q1Ur and Q1N show a very similar intensity of luminescence, and the use of SEM-CL for distinguishing between Q1Ur and Q1N is limited. Fluid inclusions trapped in Q1Ur and Q1N are not associated with any remarkable difference in the luminescence of the host.

The difference between Q1Ur and Q1N is thus, paradoxically, best seen using an ordinary optical microscope and a plane-polarized transmitted light. The difference in the transparency between Q1Ur and Q1N significantly increases if polished wafers for fluid inclusions (about 250 μm thick) are used instead of standard polished thin sections (only 30–50 μm thick).

4.2   Methods - Samples - Experimental

All the studied samples were prepared from the main quartz vein of the Libčice gold deposit. Microthermometric measurements were performed using LINKAM THMSG 600 heating–freezing stage accompanied by OLYMPUS BX50 petrographic microscope and calibrated using synthetic substances and natural pure CO_2 inclusions. Precision is calculated to be ± 0.1 °C in the whole range of observed phase changes in a low-temperature regime and about 1 °C for high-temperature measurements.

Qualitative and quantitative laser Raman microspectrometry (LRM) analysis was performed at G2R laboratory Nancy using a Labram Dilor Jobin Yvon (300 mm focal length; 1800 groove/mm grating) model, while excitation radiation provided by the Ar^+ spectral physic laser was 514,532nm. High-temperature LRM measurements were carried out by accompanying the instrument with LINKAM heating-freezing stage. The spectra treatment as baseline correction, peak picking, subtraction and curve fitting was conducted by WiRE2 software and Thermo Galactic software package. Where necessary, a mixed Gaussian – Lorentzian curve was used for fitting of the individual peaks. By default, all parameters have been floated in the fit, with no limits set, starting at 50% Lorentzian-Gaussian, following the standard routine of WiRE2 software (Tolerance 0.01; Maximum iterations 200; Square root).

4.3   Fluid Inclusion Petrography

Inclusions from the main quartz vein were studied both from Q1UR and Q1N quartz grains generation at the Libčice Gold deposit. The inclusions of the Type 1 and Type 2 were measured representing the primary inclusions for the Q1UR and Q1N, respectively. Apart from the primary inclusions, also secondary FIA were analyzed from both Q1UR and Q1N. Data on fluid evolution are available elsewhere (e.g., Zachariáš, 2002; Hrstka et al., 2011). Also the detailed description of all FIA assemblages can be found in Hrstka et al., 2011.

Type 1 aqueous carbonic inclusions

Type 1 aqueous-carbonic inclusions are basically two-phase ones (L+V) at the room temperature, mostly of regular shape and with a homogeneous phase ratio ($\varphi = 0.5 \pm 0.1$). Some of these inclusions contain also solid phases in the form of 1 or 2 birefrigant crystals (usually nahcolite, calcite as determined by Raman spectroscopy). Type 1 inclusions are hosted exclusively by grains of "unrecrystallized" relict quartz (Q1UR) and can be considered as primary with respect to this quartz (due to irregular 3D distribution).

The microthermometric characteristics are as follows: partial homogenization of carbonic phase (Th-car) occurred almost always to liquid (Lcar+Vcar→Lcar), from -21.6 to 29.5 °C; final melting

of solid CO_2 (Tm(car)) occurs between –56.6 °C to –64.1 °C, and the final clathrate dissolution Tm(Cla) between 8.3 °C to 12.3 °C. The total homogenization temperature (Th-tot) shows a maximum around 280 and 315 °C usually to vapor (V) by expansion of the CO_2-rich phase (L and C modes of homogenization were observed just occasionally). Majority of the inclusions decrepitated, however, before reaching Th-tot or immediately after this temperature. When observed, the dissolution temperature of nahcolite lies within 80–90 °C. Calcite crystals trapped in the same inclusions do not dissolve until the inclusion decrepitation at about 255 °C.

Type 2 aqueous carbonic inclusions

Type 2 inclusions are typically hosted by quartz Q1N ("neoformed quartz") that crystallized during thermal recrystallization of the original quartz gangue. This quartz is clear, well transparent and occurs in the form of inclusions (or interlocked grains) inside the sulfides (pyrrhotite), or forms quartz vein matrix. Type 2 inclusions are always two-phase (aqueous liquid + carbonic vapor) at the room temperature, 3 to 70 µm in size (commonly 10–25 µm), and display regular or negative crystal shapes. The volume fraction of aqueous liquid is 0.5 ± 0.2. Similarly to type 1 inclusions, one or more solid phases (nahcolite and/or carbonate) were identified and are present in 50–70 % of type 2 inclusions.

With respect to the density of the gaseous phase, two subtypes were defined (Hrstka et al., 2011). Apart from their density, no difference was found in the size, shape, distribution and volume fraction of the aqueous phase between type 2a (high-density) and type 2b (low-density) inclusions (Hrstka et al., 2011).

The microthermometric characteristics are as follows: high-density type 2 (Type 2a): Tm(car) from -66.2 to -60.0 °C (however, not measurable in every inclusion), Th(car) from -49 to +20 °C (always to L), Tm(Cla) from +10.8 to +18.5 °C. Low-density type 2 (type 2b): gas content of inclusions has not frozen even down to -196 °C. Th(Car) occurred from -80 to –11 °C (always to V), Tm(Cla) from +14.3 to +19.5 °C. Inclusions probably correspond to the H2 type in the classification of Kerkhof (1990).

Final homogenization /Th(total)/ could not be measured due to partial leakage of majority inclusions above 250 °C (Type 2a). In most inclusions nahcolite remained in the inclusions up to their decrepitation with no evidence of dissolution. Only occasional melting of nahcolite was observed at between 84 °C and 90 °C. Important variations in the CO_2/CH_4 ratio were found in both subtypes. However, there is no correlation between this parameter and the distribution of the inclusions at a grain scale (in contrast to type 1 inclusions in Q1Ur).

Type 3 aqueous inclusions

Type 3 are secondary inclusions occurring mostly in short intragranular trails (hosted both by Q1Ur and Q1N). Rarely, trails crosscutting grain boundaries of both quartz Q1UR and Q1N were also found. Inclusions are two-phase (L+V) at room temperature, mostly oval-shaped, and show homogeneous volume fraction of aqueous liquid (0.9–0.95).

The microthermometric characteristics are as follows: the temperature of initial melting (Ti) from -44 to -37.0 °C; final melting of ice (Tm-ice) from –4 to –1 °C, indicating that calcium is the main cation. There is no microthermometric evidence for the presence of gases. The total homogenization temperature (Th-tot, usually to vapor) shows maximum at around 140, 180 and 260 °C. No solid phases were found in secondary H_2O inclusions.

4.4   Results and Discussion

Raman study of bicarbonate-rich fluid inclusions is quite often hampered by the absence of an appropriate standard, hosted in quartz matrix and exhibiting variable bicarbonate concentrations. As the HCO_3^- was recognized during our previous study (Hrstka et al., 2011) in the aqueous phase of different inclusion types (by the presence of its peaks at 1017 cm^{-1} and 1360 cm^{-1}), the Raman spectra from the Libčice deposit represent a suitable test-set for the potential bicarbonate concentration calculations Figure 4.1.

We can assume that the individual fluid inclusion assemblages (FIA), representing groups of inclusions trapped at the same time/conditions, contain the approximately same concentration of HCO_3^-, while the different FIAs are expected to contain different concentrations of bicarbonate. Therefore. Raman spectra collected during our previous study (Hrstka et al., 2011) were reprocessed in order to estimate bicarbonate concentrations.

The high variability of different fluid types at the Libčice deposit, proved by microthermometry and Raman spectroscopy, provides us with this natural laboratory and allows the study of such unique fluid chemistry. Our relative HCO_3^- measurements allow us to make constraints on the potential calibration strategies for bicarbonate content measurement in natural fluid inclusions enclosed in quartz matrix.
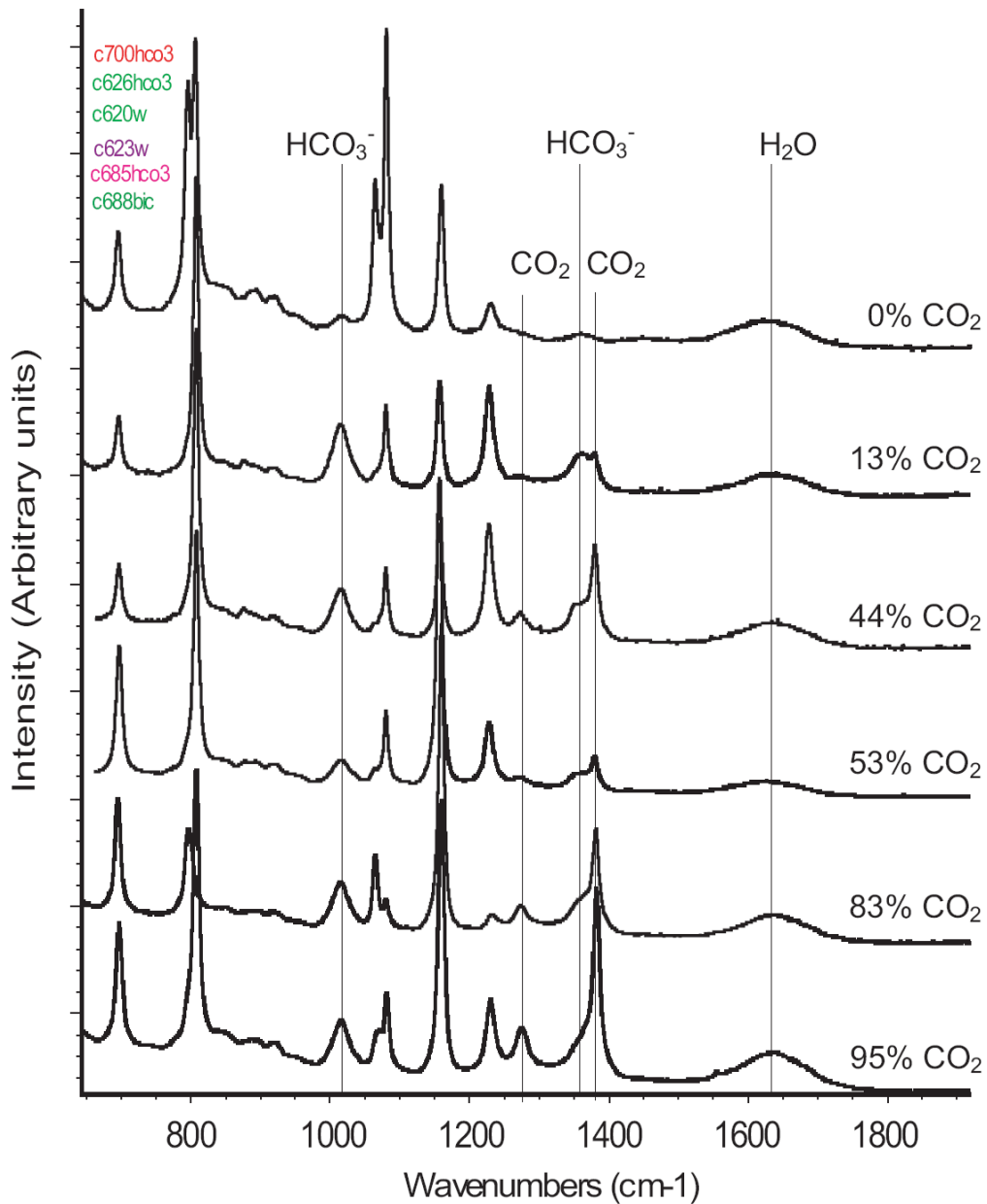
Figure 4.1: Raman spectra of bicarbonate from the aqueous-carbonic (H_2O-CO_2±CH_4) and aqueous only (H_2O) fluid inclusions in quartz matrix. Bicarbonate and CO_2 dissolved in the aqueous phase are presented. The peaks not highlighted in the image represent quartz matrix. Detailed compositions of the inclusions shown are presented inTable 4.1.

4.4.1 Gas calculation

During our experiments, quantitative gas content measurements were performed on a series of fluid inclusions representing the primary inclusion population for the original quartz Q1UR (Type1) and the primary fluid inclusions from Q1N (Type2).

Over 400 inclusions were analyzed by microthermometry and about 40 fluid inclusions were analyzed by LRM to provide evidence of the quick and complex evolution of the fluid events, which was previously suspected from the microthermometry results (Hrstka et al., 2011; Zachariáš, 2002).

The measured fluid inclusions could be classified into two categories according to the gas chemistry. This is in agreement with their occurrence mode according to petrological / petrographical / textural criteria.

Q1UR quartz primary inclusions (Type1) show H_2O-CO_2 ±(CH_4 N_2 H_2S) composition with dominant CO_2 species constituting about 98 to 89 mol% of gas content, while CH_4 forming the rest with 0.6 to 10 mol%, and traces of N_2 and H_2S are quite constant at around 0.5 and 0.1 mol%, respectively.

Q1N quartz Type 2 fluid inclusions gas content have the same main gases present as Type 1 inclusions (H_2O) CO_2 CH_4 N_2 H_2S + C_2H_6 but the variations in CO_2 *versus* CH_4 are far more important. CO_2 concentrations range from 95 mol% to 14 mol%, and CH_4 from 5 mol% to 86 mol%. The concentrations of N_2 and H_2S are almost constant still at around 0.5 and 0.1 mol%, respectively. In these fluids, ethane is constantly present at the level of traces in all measured inclusions of Type 2. Ethane clearly seen from its Raman peak at 2950 cm^{-1} and verified by the C-C stretching at 990 cm^{-1} was calculated as around 0.1 mol% from gas content. (It is worth noting that this compound was not detected in Q1UR (Type1) inclusions). No sign of precipitated carbon in the inclusions was found by the LRM.

4.4.2   High-temperature Raman measurements

The selection of inclusions/samples suitable for high-temperature Raman study was highly restricted due to the fact that primary fluid inclusions frequently show decrepitation or partial leakage at temperatures close to the Th-tot (around 300 °C), due to the rise of the internal pressure. The selection of inclusions was therefore restricted to inclusions having preferably an oval shape and small dimensions. An extreme caution was given to avoid the selection of inclusions where the water–gas ratio might have been changed during the previous experiments. Only inclusions that were continuously inspected during the increasing temperature (homogenization) were considered eligible. Finally, we selected 15 inclusions for heating experiments. Unfortunately, only two inclusions survived the heating and allowed to measure Raman spectra at all temperatures. The presence of bicarbonate in the solution is demonstrated by the peaks in the 1014 cm^{-1} and 1360 cm^{-1} region (Figure 4.2), which are clearly present in the low-temperature measurements but can be recognized also at high temperatures. The spectra were collected both at temperatures close to the Th-car (20 °C), at room temperature and at elevated temperatures (100, 200, 250 and 300 °C) and also a few degrees after the Th-tot which was 324 °C to vapor and 325 °C to critical or nearly

critical. The relative concentrations of gases in inclusions were calculated for the room temperature after Dubessy et al. (1989): 93.5 mol% CO_2, 6.5 mol% CH_4, 0.1 mol% H_2S and 80.5 mol% CO_2, 5.8 mol% N_2, 13.6 mol% CH_4 and 0.15 mol% H_2S, respectively.

For inclusion 1 in the spectra collected at temperatures slowly reaching the Th-tot, we can recognize the growth (increase) of the similarities between the spectrum collected in the liquid compared to the spectrum recorded from the gas phase. These pass to a single spectrum collected at a temperature reaching the Th-tot critical. The presence of HCO_3^- can be easily recognized up to the temperature of 250 °C where the peaks slowly decrease in their intensities and cannot be recorded clearly due to the small diameter of the fluid inclusion and potential overlaps.

For the second inclusion (inc 2), the presence of the two different phases was recorded much easier because of the type of homogenization to liquid. The spectra show the presence of bicarbonate clearly up to the Th-tot, and a few degrees above, which supports our previous suggestion that the HCO_3^- should be the most important anion in the solution. The shift of the spectral position with increasing temperature is demonstrated in Figure 4.2 and quantified in Figure 4.3.
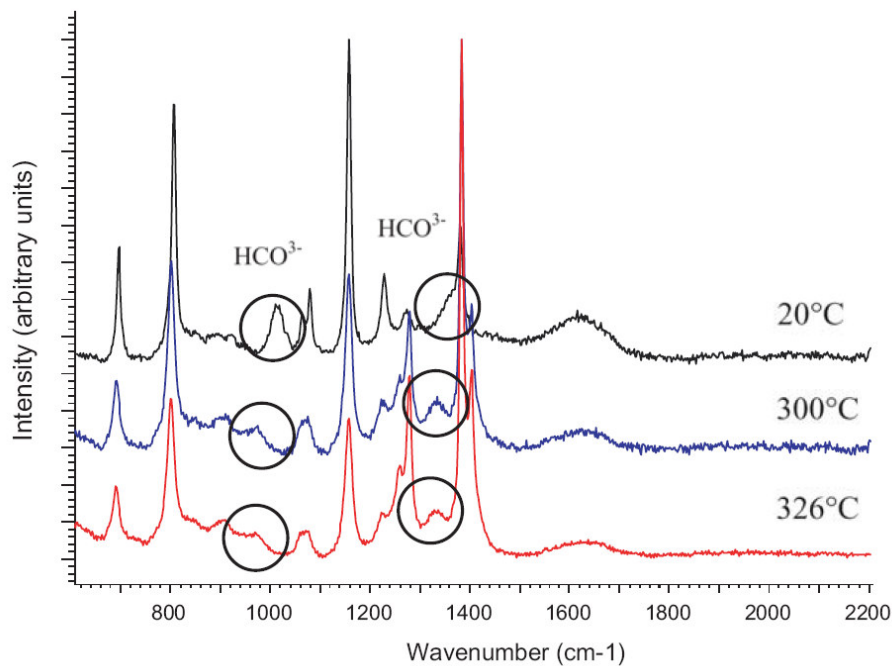
Figure 4.2: Example spectra of a bicarbonate-rich aqueous phase present in H_2O-CO_2 fluid inclusions at variable temperatures. The presence of bicarbonate in the solution is represented by the peaks in the 1014 cm^{-1} and 1360 cm^{-1} region, which are clearly present in low-temperature measurements.
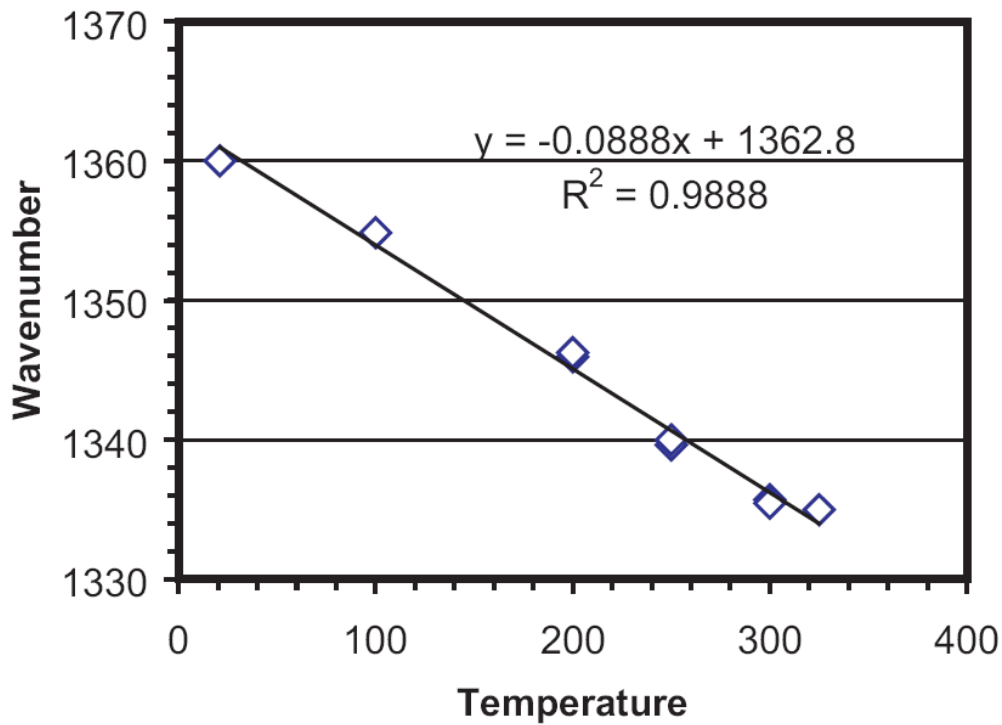
Figure 4.3: A Raman shift of the 1360 cm^{-1} bicarbonate peak in CO_2-H_2O fluid inclusions with temperature.

4.4.3   Relative HCO$_3$ concentration calculation

4.4.3.1   Using room temperature data

Based on the earlier work of Dubessy et al. (1989 and 2002) the calculation of the polyatomic ions relative concentration (RC) can be inferred as a ratio of corrected integrated area of bicarbonate peak and the peak of an internal standard (water). This is further complicated by the quartz (matrix) spectral interference in the H_2O bending region. Based on this observation we calculated the relative bicarbonate concentration as the ratio between the bicarbonate corrected integrated area at 1014–1017 cm^{-1} (A_{1017} (HCO_3^-)) and the corrected area of H_2O bending vibration ($A_{1635}(H_2O)$), while subtracting the quartz peak at the same wave number region as the H_2O bending (A_{1615}(quartz)).

$$RC_{HCO_3^-} = A_{1017}(HCO_3^-)/((A_{1635}(H_2O)-A_{1615}(quartz)) \qquad (2.1)$$

Due to the effect of crystal orientation on the shape, size and exact position of Raman peaks of quartz (Krishnamurti, 1958), a blank measurement needs to be always taken within the same quartz grain as close to the inclusion as practicable to perform the matrix correction. Examples of the observed variations in quartz spectra within the region of interest are shown in Figure 4.4
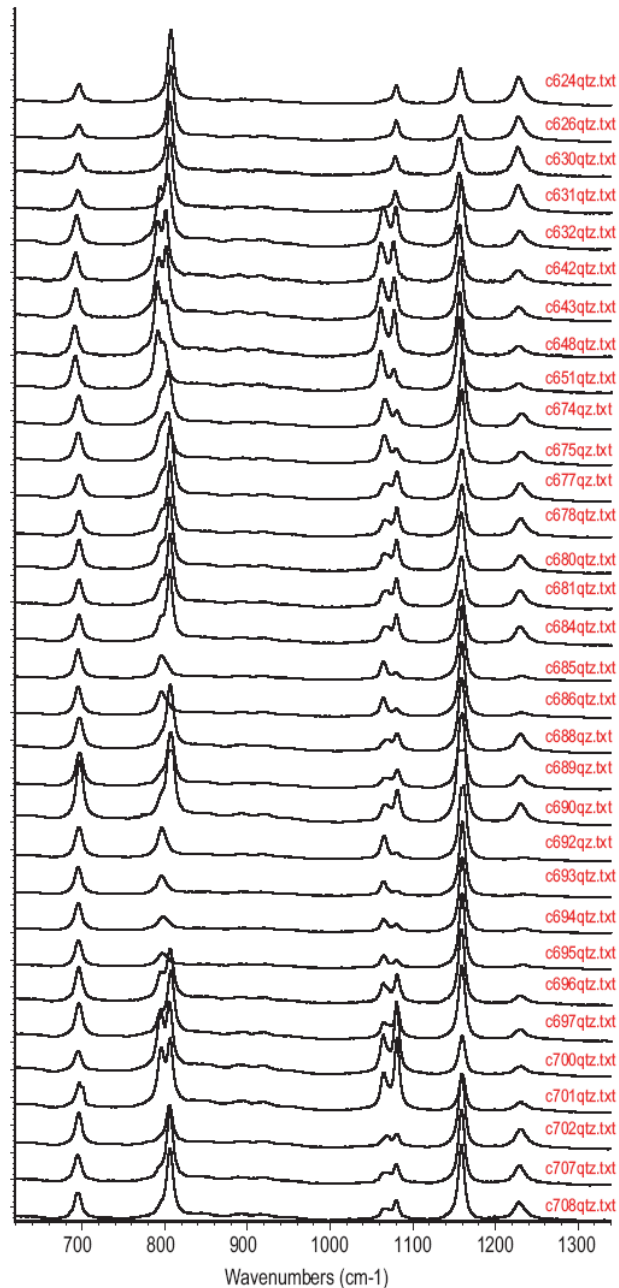
Figure 4.4: Examples of the observed variations in the Raman spectra of quartz for individual grains with different crystal orientations.

Based on the studies of speciation of HCO_3^- and CO_3^{2-} in aqueous solutions (e.g., Rudolph et.al., 2007) and other similar species (e.g., Coveney et al., 1971; Dubessy et. al., 1992; Dubessy et. al., 1982; Wu and Zheng, 2010), the detection limits for HCO_3^- and CO_3^{2-} ions could be inferred to be below 0.002 mol kg^{-1}. The relative HCO_3^- concentration based on the room temperature measurements was calculated at 0.73 to 4.18, respectively, for the inclusions analyzed, while the

higher numbers represent lower bicarbonate concentrations. The value of 2.10 represents the average relative concentration of bicarbonate in the primary fluids at the Libčice gold deposit.

Individual inclusions from the same population (FIA) show relatively the same HCO_3^- concentrations (similar RC values), while different populations differ more significantly (Tab 4.1 and Figure 4.5). Type 1 inclusions show relatively constant RC values (1.55 to 2.7), type 2 inclusions data are more scattered (0.73 to 3.93; even within a single FIA). Type 3 inclusions (H_2O) have the lowest concentration of bicarbonate with RC values reaching 4.18. Type 2 inclusions revealed no correlation between their highly variable CO_2 content and the relative HCO_3^- concentration.

In our study (calculations) the effect of salinity (chlorinity) was neglected, as it is believed to be below 5 wt.% (NaCl eq.) and cause negligible variation in H_2O Raman peak readings. The effect of Cl^- (salinity) needs to be considered for more generic HCO_3^- calculation in the future as it could affect the H_2O bending vibration parameters (shape, height, width).

 The interpretation and exact quantification of bicarbonate concentrations of the individual FIA at the Libčice gold deposit require a more detailed study in the future, including the use of external standards as solutions. A software program is in progress for the estimation of bicarbonate concentration combining microthermometric data, Raman analysis and thermodynamic modeling of ice melting temperatures (Dubessy et al., 2008).

Table 4.1: Data on relative bicarbonate concentration based on peak area ratio of bicarbonate and water as an internal standard. Microthermometric and Raman data of selected fluid inclusions are also presented.

Table 1

Sample	Sample ID	inclusion	spectrum	Width	Height	Area	CO2 %mol	CH4 %mol	N2 %mol	H2S %mol	C2H6 %mol	solids		Tm CO2	TdCLA	Th CO2		Tm-ice	RC%
						Relative Bicarbionate Concentration													
Type 1																			
LiQ11A	8 30		c632	3.91	0.63	2.45	95.5	4.3	< 0,5	< 0,1	nd			-57.8	10	20.3	L+V-L		40.8
LiQ11A	9 1		c643	4.03	0.65	2.63	95.3	4.4	< 0,5	0.1	nd			-57.8	10.3	19.6	L+V-L		38.0
LiQ11A	10 34		c646	4.32	0.56	2.48	91.3	8.3	< 0,5	0.1	nd			-58.8	10.4	17.1	L+V-L		40.3
LiQ11D	11 2		c648	5.44	0.37	2.13	93.2	6.3	0.5	0.1	nd				9.9	19.7	L+V-L		46.9
Li11-2B	5 3		c688	4.28	0.61	2.63	95.7	4.0	< 0,5	0.2	nd -				9.8	23.9	L+V-L		38.0
Li11-2B	6 32		c689	4.10	0.56	2.31	89.1	10.5	< 0,5	0.1	nd -			-59.4	11.2	14.2	L+V-L		43.2
Li11-2B	7 33		c690	3.94	0.69	2.70	87.1	12.6	< 0,5	0.1	nd -				12.3	8.2	L+V-L		37.0
Li253B	12 18		c693	3.82	0.52	1.98	92.0	7.4	0.5	0.1	nd -				10.1	19.4	L+V-L		50.4
Li253B	13 1		c694	3.66	0.54	1.93	91.6	8.2	< 0,5	nd	nd carbonate			-58.4	10.4	17.6	L+V-L	-4	51.8
Li253B	14 24		c695	3.76	0.42	1.55	91.5	8.2	< 0,5	nd	nd carbonate				10.1	16.9	L+V-L		64.6
Li1118G-3	15 incl1		c708	4.68	0.36	1.80	98.6	0.6	0.6	0.2	nd -			-57.1	8.3	26.9	L+V-L		55.4
Li1118G-3	16 incl2		c707	3.80	0.43	1.73	98.6	0.7	0.5	0.2	nd -			-57	8.3	27	L+V-L		57.7
Type2																			
Li392A	17 40		c619	4.24	0.45	1.89	51.7	48.0	< 0,5	nd	nd				15.4	-26	L+V-L		53.0
Li392A	18 7		c620	4.63	0.45	2.26	44.7	54.7	0.5	< 0,1	< 0,1 carbonate?				17.1	-42	L+V-L		44.3
Li392A	19 6		c621	3.40	0.33	1.09	69.9	29.8	< 0,5	0.1	< 0,1				14.8	-11	L+V-L		91.6
Li392A	20 15		c623	3.45	0.26	0.73	53.5	46.0	0.5	< 0,1	< 0,1 nahcolite 2xx				15.8	-24	L+V-L		137.4
Li392A	21 13		c624	3.96	0.39	1.56	45.6	54.2	< 0,5	nd	< 0,1 calcite -				16.4	-43.5	L+V-L		64.0
Li392A	22 2		c626	4.37	0.29	1.29	13.9	85.5	< 0,5	0.1	0.15 nahcolite				16.9	-76	L+V-L		77.4
Li392A	23 4		c630	6.53	0.47	2.92	61.2	38.8	< 0,5	nd	nd				15.9	*-16*	L+V-L		34.3
Li392A	24 9		c631	3.40	0.81	2.86	53.6	46.3	< 0,5	< 0,1	< 0,1 calcite - nahcolite				14.3	-32	L+V-L		35.0
Li392B	25 11		c651	3.61	0.29	1.01	58.2	41.7	< 0,5	0.1	< 0,1 muscovite						L+V-L		98.8
L1-2A	26 1		c674	4.21	0.79	3.32	91.0	8.5	< 0,5	nd	nd carbonate				11.1	13.8	L+V-L		30.2
L1-2A	27 2		c675	3.73	1.06	3.93	94.5	5.0	< 0,5	0.1	nd solid X				11	19.7	L+V-L		25.4
Li253C-1	28 7		c685	3.63	0.43	1.35	82.7	17.0	< 0,5	0.1	< 0,1 -				12.2	7.2	L+V-L		74.0
Li253C-1	29 3		c686	3.82	0.52	2.06	83.0	17.0	< 0,5	nd	nd -				12	4.7	L+V-L		48.5
Li253A-2	30 21		c696	4.65	0.42	2.08	61.3	37.0	1.4	nd	0.1 -			-62	14.5	-16.7	L+V-L		48.2
Li253A-2	31 20		c697	3.91	0.49	1.94	79.5	19.0	1.4	0.1	< 0,1 -				12.4	3.3	L+V-L		51.4
Type3																			
Li253B	3 8		c691	3.31	0.93	2.93	90.5	3.0	6.5	nd	nd	-	H_2O				L+V-L	-2.4	34.1
Li253B	4 16		c692	3.73	0.80	2.72	70.0	25.0	5.0	nd	nd	-	H_2O				L+V-L	-2.6	36.8
Li253A-1	1 30		c700	3.49	1.23	4.18	1.6	53.2	45.3	nd	nd	-	H_2O				L+V-L	-1.7	23.9
Li253A-1	2 31		c701	3.68	1.15	4.10	3.9	44.5	51.6	nd	nd	-	H_2O				L+V-L	-1.7	24.4

$RC_{HCO3}=A_{1014}(HCO_3^-)/((A_{1640}(H_2O)-A_{1620} (Quartz))$
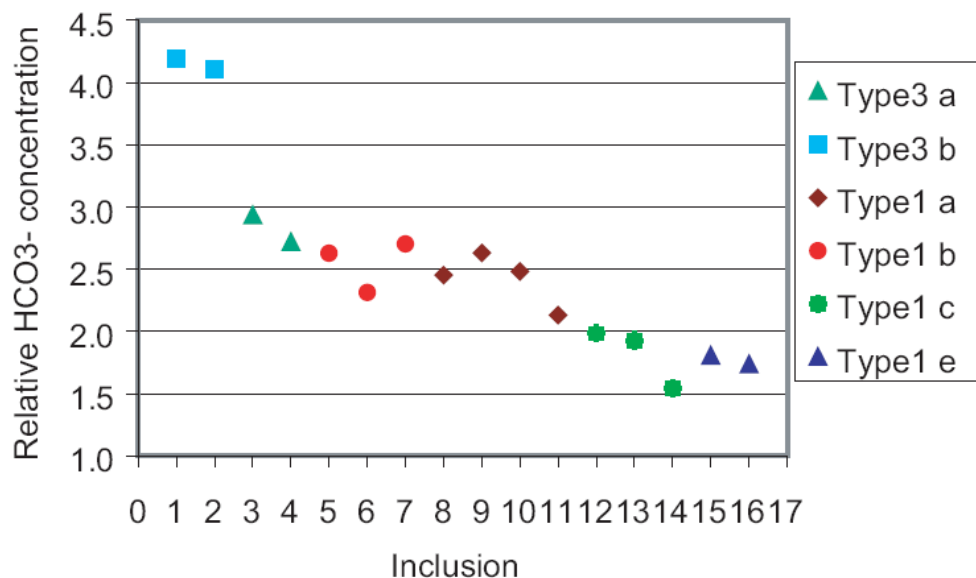
Figure 4.5: Relative concentrations of bicarbonate expressed as $RC_{HCO3}=A_{1017}(HCO_3^-)/((A_{1635}(H_2O)-A_{1615}(Quartz))$ from individual inclusions in quartz Q1.

4.4.4   High-temperature relative HCO_3^- concentration measurements

The observed HCO_3^- peak shifts with the increasing temperature led to a significant overlap with other peaks from the quartz matrix in the 1017 cm^{-1} region. This makes the use of the above stated calculation based on 1017 cm^{-1} region impossible for homogeneous fluids at around 300 °C. At temperatures between 100–300 °C, the region of 1335-1360 cm^{-1} is more suitable for concentration calculations. This is due to the separation of the HCO_3^- peaks from the Fermi doublet due to its limited shift with temperature. Based on our spectra, we suggest using the linear intensity ratios as a better option for relative bicarbonate concentration estimations than the peak integrated areas. This is supported by the linear correlation of the 1360 cm^{-1} peak shift temperature dependence (Fig. 3). The determination of the other peak shift (1017 cm^{-1}) is not trivial and even though it is visible in Figure 4.2, it was not quantified at higher temperatures.

The application of the 1360 cm^{-1} bicarbonate peak in the processing of room temperature data is complicated by its masking by the $CO_2(aq)$ matrix. As the peaks of dissolved CO_2 do not shift towards lower frequencies with the increasing temperature (as reported previously by Azbej et al., (2007) and confirmed also by our study), the 1360 cm^{-1} HCO_3^- Raman peak becomes better separated from the 1388 cm^{-1} Fermi doublet at elevated temperatures. This generally helps with its use for quantitative analysis of HCO_3^- in H_2O-CO_2 ($\pm$ CH_4) paleofluids at elevated temperatures.

4.5 HCO_3^- and CO_3^{2-} Equilibria and a Possible pH Calculation for the Studied Fluids

he pair of Raman peaks at 1017 cm^{-1} (HCO_3^-) and 1064 cm^{-1} (CO_3^{2-}) were tested by this study as a possible way for pH calculation in bicarbonate-rich paleofluids as its relevant phase equilibria are controlled by the pH. The main problems associated with this approach are the spectral overlap of quartz and CO_3^{2-} at around 1064 cm^{-1} and the lack of experimental data that could be used for calibration of relative concentrations of these polyatomic ions. Moreover, the fact that HCO_3^- is a low Raman scatterer implies that low concentrations of CO_3^{2-} in paleofluids are hard to detect.

Interestingly, we did not find an interference from quartz at the 1017 cm^{-1} in our samples, even though it was suspected earlier by Burke (2001). Raman peak of HCO_3^- was easily detectable without any spectral interaction with the quartz matrix in all our samples.

The spectral math involving baseline correction, matrix (quartz) subtraction and peak fitting was used in order to overcome the problem of spectral overlaps of the 1064 cm^{-1} (CO_3^{2-}) peak with quartz peaks (1063 cm^{-1} and 1082 cm^{-1}). Reference blank measurements were taken outside each inclusion, at the same focal depth. Blank spectra were then subtracted to reference quartz peak at 1232 cm^{-1} *(1229 cm^{-1})* before baseline correction and peak fitting. (see Figure 4.6 for details). The resulting ratio of area and height of 1017 cm^{-1} (HCO_3^-) / 1064 cm^{-1} (CO_3^{2-}) was used to estimate

the fluid inclusion pH according to data from Davis and Oliver (1972) and Abbot at al. (1981). Based on this comparison we suggest pH in fluid inclusions from the Libčice gold deposit to be close to neutral ($\sim$ 7) or slightly alkaline ($\sim$ 8.5) conditions.

Two to three quartz peaks were identified (Figure 4.7) in the interval of interest of 1000–1100 cm^{-1} instead of only two (cited in literature as 1063 and 1082 cm^{-1}). In our case these have centers at $\sim$1065, 1072 and 1081 cm^{-1}, respectively, and their relative position and peak intensity varies with crystal orientation and/or deformation. In agreement with the previous work of Krishnamurti (1958), their position shifts for the different inclination of the optical axis is in the range of 2 to 8 cm^{-1}. This explains the complexity of relative Raman intensity ratios of quartz matrix in the region significant for CO_3^{2-} quantification. These interferences/shifts also limit the quantitative concentration measurements of sodium carbonate as described by Wu and Zheng (2010) in natural fluid inclusions hosted in quartz.

Measurement of orientated quartz samples can be suggested for overcoming the effect of spectral interferences of quartz and CO_3^{2-} at around 1064 cm^{-1}, hence also for the improvement of the detection limits for CO_3^{2-}.
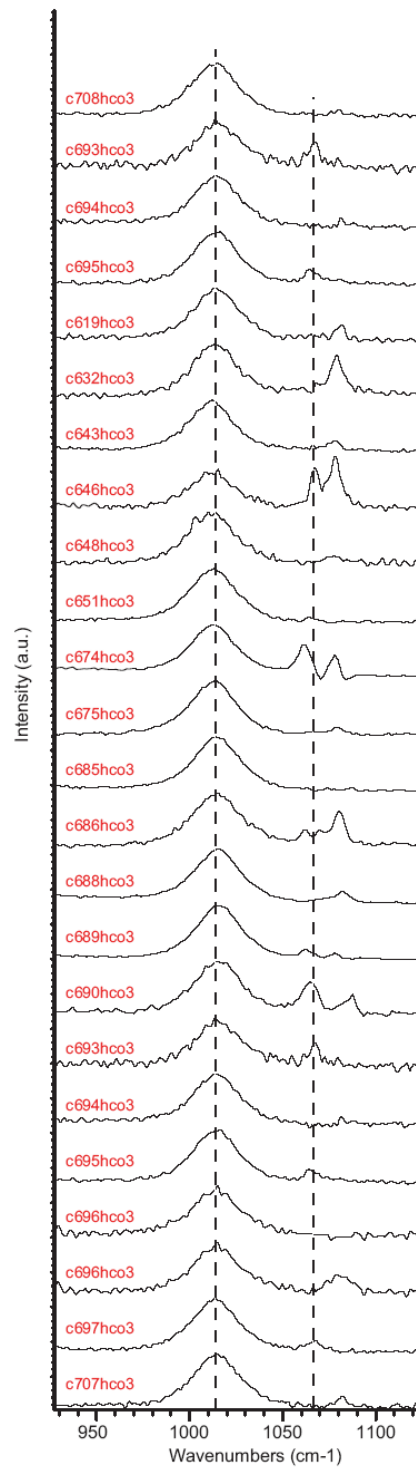
Figure 4.6: Raman spectra of the quartz matrix spectral subtraction results in the region proposed for pH calculation of paleofluids. Relative intensity ratio of HCO_3^- (1017 cm^{-1}) / CO_3^{2-} (1066 cm^{-1}) can be inferred from the image. Note the occasional relatively small peak at 1066 cm^{-1} representing the potential CO_3^{2-} presence and also some spectral artifacts created by spectral math and the influence of highly variable relative position and peak intensity of quartz.
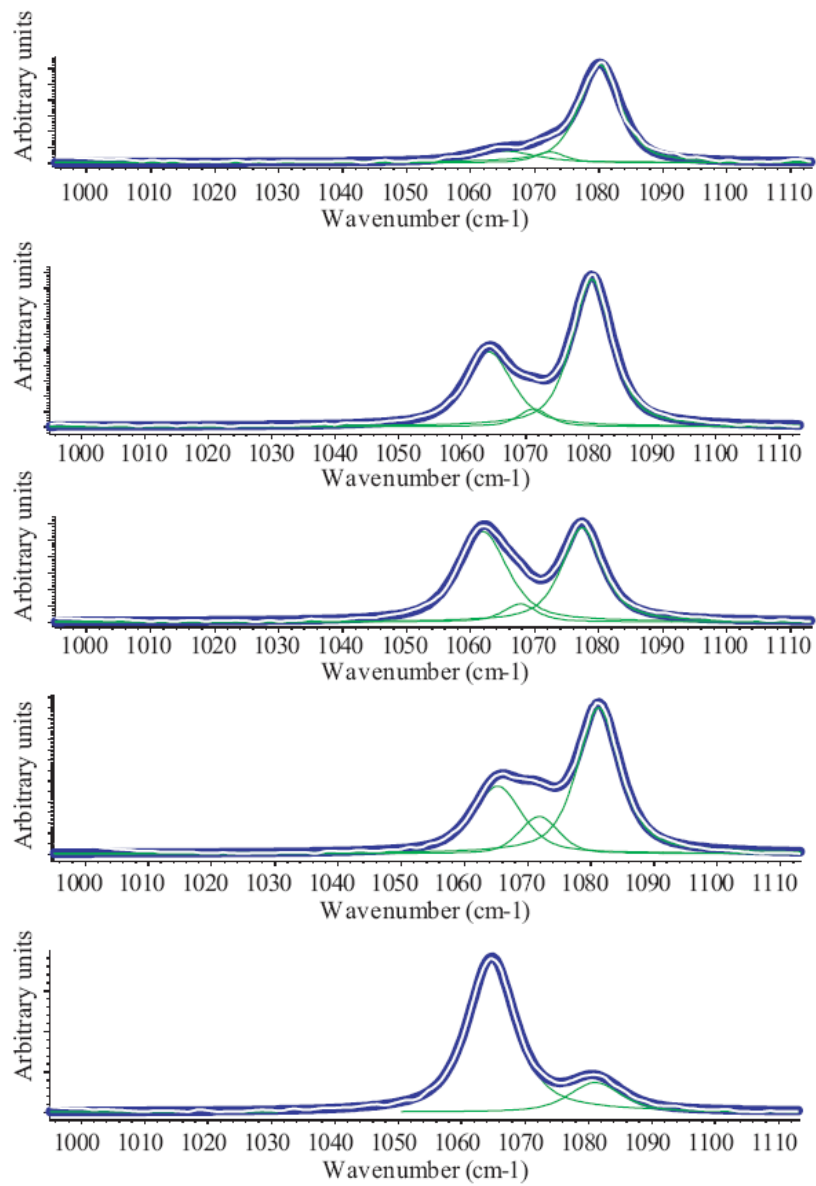
Figure 4.7: Example Raman spectra of the quartz matrix showing variations in the region of interest for CO_3^{2-} quantification and potential pH calculation of paleofluids. The variations are due to differences in crystal orientation.

4.6   Conclusions and Future Work

The high concentration of bicarbonate was directly confirmed by the RT and HT Raman spectroscopy in the natural aqueous-carbonic fluid inclusions from an orogenic-style gold deposit of Libčice.

Potential peaks for concentration calculation of bicarbonate in the H_2O-CO_2-CH_4 system and quartz matrix were tested for both low-temperature and high-temperature measurements. For HCO_3^- these were established at 1014 cm^{-1} and 1360 cm^{-1}, while the H_2O bending vibration peak at 1630 cm^{-1} was suggested as an internal reference for the relative concentration calculation.

In low-temperature measurements, the RC_{HCO3}=A_{1014}(HCO_3^-)/((A_{1640}(H_2O)-A_{1620} (Quartz)) formula involving peak area ratios was suggested as the most practical while the peak height ratio (RC_{HCO3}=I_{1360}(HCO_3^-)/((I_{1640}(H_2O)-I_{1620} (Quartz)))) seems more applicable to temperatures close to the homogenization temperature (100–300 °C).

This is mainly because the shift of both peaks with temperature towards the low wavenumbers. It leads to masking/overlap of the "1014 cm^{-1} HCO_3^-" peak by quartz and improves separation of the "1360 cm^{-1} HCO_3^-" peak from peak of the CO_2 dissolved in water which interestingly shows little to no shift with temperature. Also the change in the peak shapes with temperature is more favorable for the use of the 1360 cm^{-1} peak for high-temperature Raman measurements.

Due to the overlap between H_2O bending and quartz, the deconvolution and subtraction of quartz and H_2O peaks at around 1620 cm^{-1} seems to be important for the use of the H_2O peak as a reference (internal standard) for quantification of any polyatomic ions in fluid inclusions. The use of stretching vibration of water at around 3600 cm^{-1} can be suggested as an alternative internal standard. Nevertheless, its dependence on salinity and crystal orientation needs to be taken into account as well.

The relative quantification of HCO_3^- concentration at the Libčice gold deposit was calculated and shows variable quantities in different fluid populations and single inclusions as expected. Relatively constant HCO_3^- concentrations were confirmed for selected inclusions from the same FIA, while the inclusions from different parts of the mine show systematic changes in bicarbonate concentrations as a function of the distance from the CBPC intrusion. The nahcolite and calcite daughter crystals do not seem to affect bicarbonate concentrations for the individual inclusions.

CO_3^{2-} detection and quantification in natural inclusions trapped in quartz is restricted/complicated by the spectral interference of the main CO_3^{2-} peak (1062 cm^{-1}) with quartz (1063 cm^{-1} and 1082 cm^{-1}). Even with spectral subtraction and peak deconvolution the expected low quantities of CO_3^{2-} cannot be measured very accurately because of the variance in relative intensity ratios of individual quartz peaks in the region of interest. Measurements of orientated crystals might help to minimize the impact of interference from 1063 cm^{-1} peak of quartz intensity which is strongly

dependent on crystal orientation. We expect that the principal Raman shift of the 1086 cm^{-1} peak in carbonates may also affect the ability to precisely quantify CO_3^{2-} in carbonates.

Additional tests on standards of known HCO_3^{-} concentrations are necessary to set up the detection limits and absolute concentration calculations. This will involve the creation of HCO_3^{-} -bearing synthetic fluid inclusions with a known cation concentration/chemistry.

Acknowledgements:

5. QEMSCAN ANALYSIS OF ROCKS FROM THE LIBČICE MINE AREA: SEARCH FOR SPECIFIC LOW-DENSITY MINERALS IN FINE-GRAINED ROCK SAMPLES (ARTICLE 3)

Tomáš Hrstka[1,2],

[1] *Institute of Geology AS CR, v.v.i., Rozvojová 269, CZ-165 00 Prague 6 – Lysolaje, Czech Republic*
*E-mail: **hrstka@gli.cas.cz***

[2] *Charles University in Prague, Faculty of Science, Institute of Geochemistry, Mineralogy and Mineral Resources, Albertov 6, Praha 2, CZ-128 43, E-mail: zachar@natur.cuni.cz*

Status: In preparation

Abstract

Automated mineralogy techniques have become increasingly utilized not only in metallurgy and mining applications but also in broad geological research areas. QEMSCAN, as a representative of automated e-beam techniques, was tested for the identification and quantification of specific low-density minerals in fine-grained rock samples. The QEMSCAN advantages over more traditional techniques like optical microscopy, XRD or classical SEM were examined. In addition, the repeatability and reproducibility of individual measurements were studied in relation to the size of the sample analyzed and its natural heterogeneity.

Ten rock samples were analyzed from the close vicinity of the Libčice mine for the potential presence of nahcolite or other minor Na-bearing phases. The presence of these minerals would correlate with the bicarbonate-rich nature of the paleofluids present in the main quartz vein of the Libčice gold deposit. QEMSCAN analysis demonstrated the absence of nahcolite in the studied black shales and in other rock types. Sodium deportment in all the studied rocks is attributed mostly to Na feldspars (usually representing about 90 % of the Na in the rock). Other minor Na-bearing phases are clay minerals.

Based on the test for reproducibility and repeatability of the QEMSCAN measurements the relative standard deviation (RSD) varied generally from 0.5 to 10 % for phases representing above 5 wt % of the modal composition. For phases representing less than 5 wt % modal the RSD can increase dramatically. The RSD variation is strongly dependent on the average particle size and sample texture (i.e., rock heterogenity on a small scale).

5.1　Introduction

QEMSCAN is a well-established automated mineralogy technique which was originally developed as a tool for metallurgy and mining applications and was broadly used for statistically robust automated mineralogical analysis of plant products and feed (Gottlieb et al., 2000). During the last decade, more general applications of QEMSCAN and other e-beam technologies have become available to industry and scientists. Wide variety of geological materials were analyzed including, dust particles, coal, exploration samples, cement etc. (Latti et al., 1997; Gottlieb et al., 2000; Pirrie et al., 2000; Adamini and Hrstka, 2008; Andersen et al., 2009; Haberlah et al., 2010, 2011).

In this study we have tested the use of automated mineralogy system to search for potential presence of nahcolite or other minor high-Na low-density phases in fine-grained rock, which could correlate with the bicarbonate rich nature of all paleofluids present in the main quartz vein of the Libčice Gold deposit (Hrstka et al., 2011). QEMSCAN data were compared with optical microscopy and X-ray powder diffraction analysis.

General problems related to fully automated mineralogical analysis of samples as well as estimates of relative standard deviation RSD% for measurements are also discussed in detail. The exact differentiation between the individual rock-forming minerals and their alteration products is still not unambiguous. Manual interaction or future implementation of an expert system will be necessary to provide accurate results on complex fine grained rocks while the introduction of new analytical procedures seems to have promising results in this regards (Haberlah et al., 2010).

5.2　Samples Description

Samples have been prepared as classical thin sections for petrographic examination. For the purpose of QEMSCAN analysis selected samples were carbon coated. Alcohol based sample preparation was used to avoid potential damage to water soluble species. Ten samples of rocks from the close vicinity of Libčice gold deposit were selected representing typical lithologies present. Metamorphosed Proterozoic sediments and associated igneous rocks were examined including: black shales (LB22, LB20); chert (LB4); quartzite (LB25); aplites and metasomatised dykes (LB9, LB10, LB17, LB23); tuffs and rhyolites (LB2, LB15).

5.3　Experimental and Methods

All the samples were analysed by the QEMSCAN E-series and 310-series instruments fitted with 4 or 3 Sirius series - Si(Li) detectors (SIRIUS 10/SUTW). All the test measurements were run at 25keV with 5 nA beam current. FieldImage analysis mode was used to collect 63 fields with 2500 um across per sample. This represents 2 by 2.5 cm area per thin section. Selected 10.5 um point spacing lead to over 3.5 million analytical points per sample (collected within less then 7h-corresponding to less then 4h on the new QEMSCAN systems available at the moment Botha et al., 2008).

Quantitative mineralogical fieldscan measurements were performed to create mineralogical maps of all samples (Figure 5.1). Apart from the modal mineralogy these maps were also used to study mineral distribution and textures. Quantification of chemical composition of individual minerals and their mass distribution was used to provide information on elemental deportment of Na.

Repeatability and reproducibility of QEMSCAN system was tested on the series of measurements from our standard samples with known modal mineralogy composition to establish the minimal number of mineral grains required to take an advantage of quantitative mineralogy and obtain statistically valid automated mineralogical data. The results of this testing are presented in a separate article (Chapter 6) which was presented at ICAM (International Congress of Applied Mineralogy) 2008.

To support the identification of individual main mineralogical species the XRD and petrographical examination were also conducted. For the XRD analysis the representative samples of selected rocks were prepared and analyzed using PANanalytical X`Pert Pro diffractometer equipped with a diffracted-beam monochromator and X`Celerator multichannel detector. The analysis conditions were as following: CuKα radiation, 40kV, 30mA, step scanning at 0.02°/100s in the range 3-80° 2θ. The quantitative analysis employed the X`Pert HighScore software 1.0d, equipped with the JCPDS PDF-2 database (ICDD, 2002).

Polarizing Optical microscope OLYMPUS BX50 accompanied with the DP70 digital camera was used for petrographic investigation.

Also an automated Raman mapping of selected samples was performed in regards to correlate its results with the QEMSCAN data and provide first constrains on the applicability of ultra fast Raman imaging as a tool for quantitative mineralogy and petrology. The results of this investigation will be presented elsewhere.

5.4   Results

Results of modal analysis and elemental deportment data are presented in the Table 5.1 , Table 5.2 and Figure 5.2 respectively.
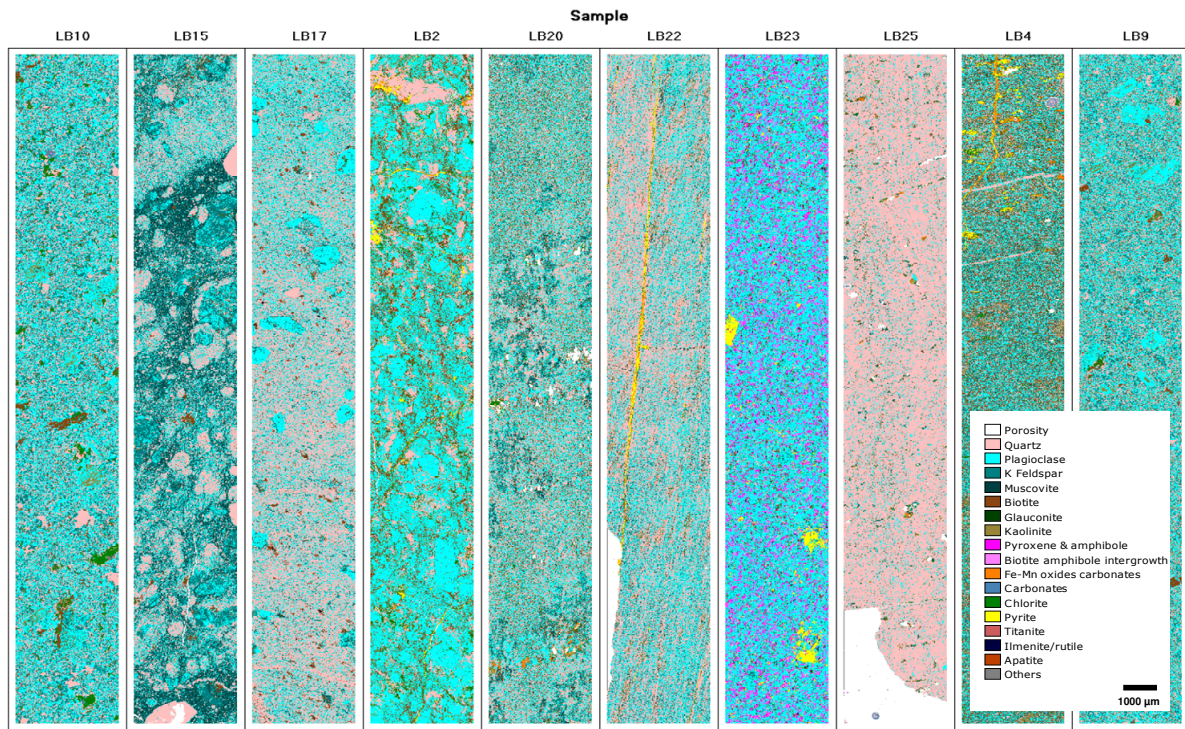
Figure 5.1: Example of the color coded mineral maps from the QEMSCAN analysis.

As a part of this project the repeatability and reproducibility of QEMSCAN system was also tested on the series of measurements from our standard samples with known modal mineralogy composition to establish the minimal number of mineral grains required to take an advantage of quantitative mineralogy and obtain statistically valid automated mineralogical data. The results of this testing are presented in a separate article in Section 6 which was presented at ICAM (International Congress of Applied Mineralogy) 2008.

Table 5.1: QEMSCAN measurement modal results.

Survey	Id										
	Name	LBa									
	Datastore Name	LBa Rock									
Sample	**Name**	**LB17**	**LB20**	**LB22**	**LB23**	**LB25**	**LB4**	**LB2**	**LB15**	**LB9**	**LB10**
	Id	A	B	C	D	E	F	G	H	I	J
Untitled	**Total Mass**	**100.00**	**100.00**	**100.00**	**100.00**	**100.00**	**100.00**	**100.00**	**100.00**	**100.00**	**100.00**
Measurement	**Measurement Mode**	**FieldImage**	**FieldImage**	**FieldImage**	**FieldImage**	**FieldImage**	**FieldImage**	**FieldImage**	**FieldImage**	**FieldImage**	**FieldImage**
Mineral Mass	Quartz	50.68	34.25	51.10	4.08	82.81	17.66	17.91	27.33	25.97	25.96
	Albite	14.26	15.61	1.55	6.33	2.01	8.73	37.94	0.60	15.41	19.89
	Plagioclase	0.67	1.68	1.19	40.07	0.25	9.48	12.33	0.36	7.09	5.45
	K Feldspar	7.37	9.20	9.02	1.06	2.79	12.45	0.75	28.46	18.86	22.95
	Muscovite	2.02	3.68	2.46	1.35	0.66	2.71	0.51	16.40	0.68	0.57
	Biotite	2.70	7.73	1.31	4.46	1.22	21.39	11.71	1.78	6.35	3.15
	Glauconite	0.13	1.98	0.53	0.05	0.01	1.72	0.84	0.07	0.25	0.04
	Illite	18.58	17.37	25.44	5.51	7.37	11.59	2.67	22.86	17.34	15.29
	Kaolinite	3.32	5.66	4.19	1.68	1.08	9.45	7.62	1.95	6.88	3.31
	Pyroxene & amphibole	0.00	0.00	0.00	12.67	0.01	0.00	0.04	0.00	0.01	0.01
	Biotite amphibole intergrowth	0.00	0.00	0.00	15.34	0.00	0.00	0.00	0.00	0.01	0.03
	Fe-Mn oxides carbonates	0.00	0.90	0.12	0.01	0.34	0.71	0.60	0.01	0.00	0.00
	Carbonates	0.03	0.04	0.07	0.93	0.02	0.09	0.03	0.02	0.10	0.34
	Chlorite	0.13	1.59	0.60	2.47	1.26	3.42	4.67	0.08	0.89	2.72
	Pyrite	0.00	0.01	1.97	2.83	0.02	0.42	2.12	0.00	0.00	0.00
	Titanite	0.01	0.21	0.43	0.16	0.13	0.07	0.09	0.01	0.02	0.10
	Ilmenite/ rutile	0.08	0.08	0.01	0.76	0.03	0.07	0.16	0.03	0.00	0.00
	Apatite	0.03	0.00	0.01	0.10	0.00	0.00	0.00	0.04	0.13	0.12
	Others	0.00	0.01	0.02	0.12	0.01	0.03	0.02	0.01	0.01	0.08

In agreement with the expectations, alkaline tuffs were identified as the highest Na source. No Nahcolite was identified in the studied rocks while the Na deportment was attributed mainly to Na feldspars representing over 90% of Na in all the samples.
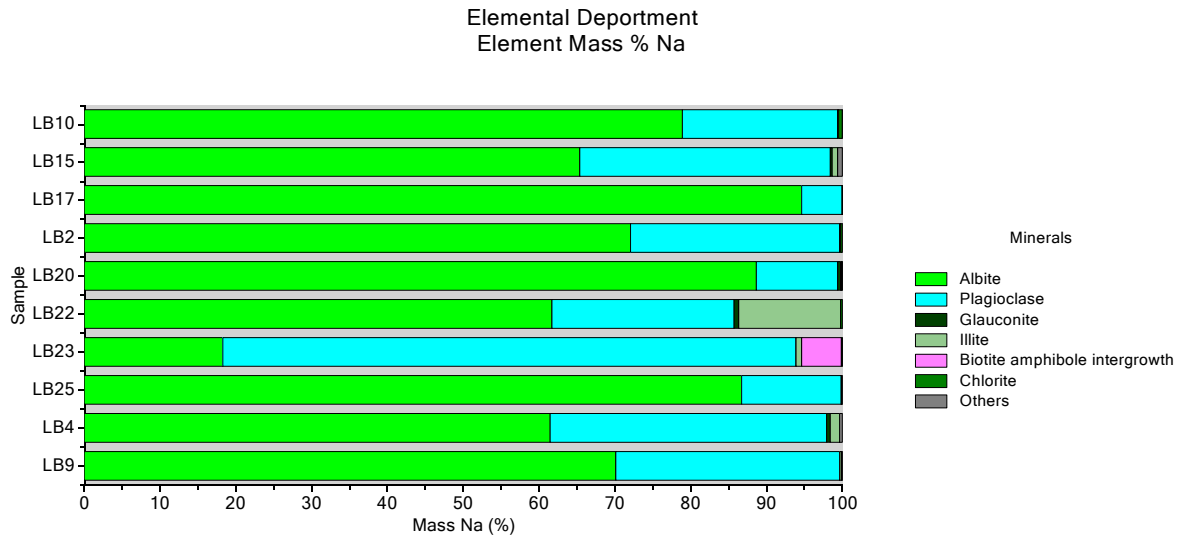
Figure 5.2: Elemental deportment data based on the modal mineralogy.

Table 5.2: QEMSCAN elemental deportment data based on the modal mineralogy.

Mass Na (%)

Minerals	Sample	LB9	LB4	LB25	LB23	LB22	LB20	LB2	LB17	LB15	LB10
	Albite	70.06	61.46	86.66	18.24	61.67	88.68	72.01	94.68	65.32	78.94
	Plagioclase	29.54	36.51	13.24	75.64	24.00	10.68	27.66	5.26	33.09	20.43
	Glauconite	0.04	0.39	0.01	0.00	0.68	0.36	0.05	0.03	0.24	0.01
	Illite	0.20	1.23	0.01	0.77	13.43	0.19	0.02	0.02	0.72	0.15
	Biotite & amphibole intergrowth	0.00	0.00	0.00	5.16	0.00	0.00	0.00	0.00	0.00	0.01
	Chlorite	0.14	0.08	0.05	0.18	0.20	0.08	0.22	0.01	0.07	0.46
	Others	0.01	0.33	0.03	0.00	0.01	0.00	0.04	0.00	0.56	0.01

To evaluate the repeatability of analysis of fine-grained rocks, the series of quantitative measurements were compared to assess the real rocks heterogeneity and provide leads on RSD% for quantitative analysis of rocks in thin sections.

For these tests each thin section was split in 10 and 5 equivalent/allotments represented by 6 or 12 square fields (2500µm^2 each) selected in successive manner and randomly. Successive and randomly selected field groups were then compared for their mineralogy and RSD%. The results are presented in Table 5.3, Table 5.4 and Figure 5.3.

Table 5.3: QEMSCAN measurement repeatability results.

Survey	Id															
	Name															
Sample	Name	RSD	AVG	RSD%	RSD	AVG	RSD%	RSD	AVG	RSD%	RSD	AVG	RSD%	RSD	AVG	RSD%
	Id	A	A	A	B	B	B	C	C	C	D	D	D	E	E	E
Field ID Number Final6	Name	LB17	LB17	LB17	LB20	LB20	LB20	LB22	LB22	LB22	LB23	LB23	LB23	LB25	LB25	LB25
Mineral Mass(%)	Quartz	6.49	50.33	12.9%	0.66	34.24	1.9%	5.80	51.35	11.3%	0.39	4.09	9.5%	3.86	82.79	4.7%
	Plagioclase	0.15	0.67	22.8%	0.12	1.68	7.0%	0.31	1.20	26.0%	0.61	40.05	1.5%	0.06	0.25	23.8%
	K Feldspar	0.82	7.42	11.0%	0.86	9.22	9.4%	1.32	8.95	14.8%	0.16	1.06	15.5%	0.87	2.80	31.1%
	Muscovite	0.22	1.00	22.1%	0.24	1.48	16.3%	0.22	0.81	27.4%	0.07	1.09	6.4%	0.16	0.35	44.6%
	Biotite	0.57	2.91	19.5%	0.79	9.20	8.6%	0.47	1.55	30.4%	0.60	4.63	13.1%	0.49	1.35	36.2%
	Glauconite	0.01	0.03	45.5%	0.06	0.77	8.2%	0.03	0.20	17.5%	0.00	0.02	14.4%	0.00	0.00	171.3%
	Illite	1.74	19.47	8.9%	1.00	19.21	5.2%	2.50	26.88	9.3%	0.16	5.54	3.0%	1.41	7.55	18.6%
	Kaolinite	0.31	3.32	9.3%	0.44	5.85	7.5%	1.10	4.26	25.9%	0.07	1.81	3.6%	0.29	1.09	26.7%
	Pyroxene & amphibole	0.00	0.00	-	0.00	0.00	-	0.00	0.00	-	0.45	12.70	3.5%	0.01	0.01	95.7%
	Biotite amphibole intergrowth	0.00	0.00	-	0.00	0.00	-	0.00	0.00	-	0.61	15.37	4.0%	0.00	0.00	-
	Fe-Mn oxides carbonates	0.00	0.00	331.7%	0.57	0.89	64.2%	0.29	0.11	268.9%	0.00	0.01	34.2%	0.13	0.33	37.9%
	Carbonates	0.01	0.03	39.3%	0.02	0.04	53.6%	0.03	0.07	35.4%	0.07	0.93	7.6%	0.01	0.01	99.9%
	Chlorite	0.02	0.13	19.4%	0.31	1.58	19.5%	0.31	0.59	51.3%	0.19	2.48	7.8%	0.25	1.26	20.0%
	Pyrite	0.00	0.00	-	0.01	0.01	171.3%	1.45	2.01	72.2%	1.35	2.75	49.0%	0.04	0.01	289.0%
	Titanite	0.00	0.01	64.2%	0.05	0.21	22.1%	0.18	0.42	42.7%	0.02	0.16	10.3%	0.04	0.13	27.4%
	Ilmenite/rutile	0.04	0.07	58.9%	0.03	0.08	32.8%	0.01	0.01	77.5%	0.07	0.75	9.4%	0.02	0.03	54.1%
	Apatite	0.02	0.03	57.7%	0.00	0.00	-	0.01	0.01	50.8%	0.01	0.10	9.8%	0.00	0.00	-
	Others	0.01	0.00	138.7%	0.01	0.01	126.1%	0.01	0.02	38.1%	0.02	0.12	20.0%	0.01	0.01	95.7%
Field number random 6 from 63	Name															
Mineral Mass(%)	Quartz	1.18	50.92	2.3%	0.82	34.25	2.4%	2.50	51.46	4.8%	0.34	4.10	8.3%	2.05	82.63	2.5%
	Plagioclase	0.07	0.67	10.4%	0.11	1.69	6.7%	0.14	1.17	11.7%	0.43	40.05	1.1%	0.04	0.25	14.1%
	K Feldspar	0.30	7.31	4.1%	0.91	9.09	10.0%	0.51	8.96	5.7%	0.16	1.06	15.5%	0.36	2.82	12.9%
	Muscovite	0.15	1.00	14.7%	0.19	1.48	12.6%	0.10	0.79	12.8%	0.07	1.09	6.7%	0.06	0.36	17.0%
	Biotite	0.37	2.90	12.9%	0.54	9.22	5.8%	0.20	1.53	13.3%	0.36	4.59	7.9%	0.30	1.36	22.0%
	Glauconite	0.01	0.03	30.5%	0.05	0.77	7.0%	0.02	0.19	7.7%	0.00	0.02	15.8%	0.01	0.00	138.7%
	Illite	0.62	19.34	3.2%	0.93	19.06	4.9%	1.24	26.95	4.6%	0.14	5.54	2.6%	0.69	7.61	9.0%
	Kaolinite	0.20	3.34	6.1%	0.22	5.82	3.8%	0.54	4.22	12.9%	0.06	1.82	3.4%	0.17	1.11	15.7%
	Pyroxene & amphibole	0.00	0.00	-	0.00	0.00	331.7%	0.00	0.00	-	0.37	12.68	2.9%	0.01	0.01	95.7%
	Biotite amphibole intergrowth	0.00	0.00	-	0.00	0.00	-	0.00	0.00	-	0.40	15.34	2.6%	0.00	0.00	-
	Fe-Mn oxides carbonates	0.00	0.00	222.5%	0.62	0.94	66.7%	0.15	0.12	120.4%	0.00	0.01	36.7%	0.11	0.34	31.9%
	Carbonates	0.02	0.03	49.0%	0.02	0.04	49.4%	0.01	0.07	19.4%	0.05	0.93	5.7%	0.02	0.02	111.8%
	Chlorite	0.02	0.12	15.0%	0.22	1.62	13.7%	0.18	0.60	30.6%	0.11	2.48	4.5%	0.15	1.27	11.5%
	Pyrite	0.00	0.00	-	0.01	0.01	145.3%	0.66	1.93	34.5%	0.89	2.81	31.9%	0.02	0.02	110.2%
	Titanite	0.00	0.01	49.4%	0.02	0.21	9.4%	0.06	0.42	15.2%	0.01	0.17	5.6%	0.03	0.13	19.2%
	Ilmenite/rutile	0.04	0.07	50.3%	0.01	0.08	18.0%	0.00	0.01	27.6%	0.06	0.76	7.9%	0.01	0.03	33.9%
	Apatite	0.02	0.03	55.0%	0.00	0.00	-	0.00	0.01	36.7%	0.01	0.10	13.5%	0.00	0.00	-
	Others	0.00	0.00	222.5%	0.01	0.01	95.7%	0.01	0.02	52.4%	0.02	0.12	13.2%	0.01	0.01	95.7%
Field ID Number Final12	Name															
Mineral Mass(%)	Quartz	1.86	50.36	3.7%	0.31	34.24	0.9%	4.80	51.33	9.3%	0.25	4.09	6.0%	3.52	82.80	4.3%
	Plagioclase	0.09	0.67	13.5%	0.10	1.68	5.8%	0.24	1.20	19.9%	0.49	40.05	1.2%	0.06	0.25	24.0%
	K Feldspar	0.33	7.42	4.5%	0.61	9.22	6.7%	0.68	8.96	7.6%	0.10	1.07	9.7%	0.71	2.80	25.4%
	Muscovite	0.15	1.00	15.0%	0.18	1.48	11.9%	0.19	0.81	23.5%	0.04	1.09	3.3%	0.12	0.35	33.8%
	Biotite	0.38	2.92	13.0%	0.67	9.20	7.3%	0.37	1.55	23.6%	0.46	4.62	10.0%	0.47	1.35	34.9%
	Glauconite	0.01	0.03	21.1%	0.06	0.77	7.3%	0.02	0.20	11.0%	0.00	0.02	0.0%	0.01	0.00	154.9%
	Illite	1.23	19.34	6.3%	0.79	19.21	4.1%	1.44	26.89	5.4%	0.14	5.54	2.6%	1.21	7.55	16.1%
	Kaolinite	0.22	3.32	6.6%	0.37	5.84	6.3%	1.03	4.26	24.2%	0.06	1.81	3.1%	0.26	1.10	23.9%
	Pyroxene & amphibole	0.00	0.00	-	0.00	0.00	-	0.00	0.00	-	0.27	12.70	2.2%	0.01	0.01	109.5%
	Biotite amphibole intergrowth	0.00	0.00	-	0.00	0.00	-	0.00	0.00	-	0.25	15.37	1.6%	0.00	0.00	-
	Fe-Mn oxides carbonates	0.00	0.00	244.9%	0.49	0.89	55.6%	0.20	0.11	178.8%	0.00	0.01	35.0%	0.08	0.33	23.1%
	Carbonates	0.01	0.03	31.0%	0.01	0.04	35.4%	0.02	0.07	32.6%	0.07	0.93	7.0%	0.01	0.01	77.5%
	Chlorite	0.02	0.13	11.9%	0.21	1.58	13.3%	0.29	0.60	48.5%	0.10	2.48	4.2%	0.23	1.26	18.6%
	Pyrite	0.00	0.00	-	0.01	0.01	109.5%	0.81	2.02	40.0%	0.84	2.77	30.4%	0.03	0.02	187.4%
	Titanite	0.00	0.01	49.0%	0.04	0.21	18.2%	0.17	0.42	41.5%	0.01	0.16	8.4%	0.03	0.13	22.8%
	Ilmenite/rutile	0.03	0.08	33.7%	0.02	0.08	30.5%	0.01	0.01	63.2%	0.06	0.76	7.4%	0.01	0.03	46.5%
	Apatite	0.01	0.03	23.8%	0.00	0.00	-	0.00	0.01	35.0%	0.01	0.10	7.7%	0.00	0.00	-
	Others	0.01	0.01	109.5%	0.01	0.01	109.5%	0.01	0.02	44.3%	0.01	0.12	10.9%	0.01	0.01	109.5%
Field number random 12 from 63	Name															
Mineral Mass(%)	Quartz	1.05	50.90	2.1%	0.71	34.26	2.1%	1.80	51.43	3.5%	0.27	4.10	6.6%	1.53	82.67	1.8%
	Plagioclase	0.06	0.67	9.2%	0.03	1.69	1.7%	0.07	1.18	5.7%	0.27	40.05	0.7%	0.03	0.25	10.3%
	K Feldspar	0.17	7.32	2.4%	0.71	9.10	7.8%	0.36	8.96	4.0%	0.10	1.06	9.4%	0.28	2.81	10.0%
	Muscovite	0.11	1.01	11.2%	0.10	1.48	6.5%	0.06	0.80	7.1%	0.06	1.09	5.4%	0.05	0.36	13.1%
	Biotite	0.11	2.91	3.9%	0.29	9.21	3.2%	0.12	1.54	7.5%	0.29	4.59	6.3%	0.15	1.36	11.3%
	Glauconite	0.01	0.03	24.5%	0.03	0.77	3.6%	0.01	0.19	4.2%	0.00	0.02	0.0%	0.01	0.00	154.9%
	Illite	0.41	19.35	2.1%	0.55	19.07	2.9%	0.77	26.96	2.9%	0.07	5.54	1.3%	0.52	7.59	6.9%
	Kaolinite	0.13	3.35	4.0%	0.19	5.82	3.2%	0.37	4.23	8.7%	0.03	1.82	1.8%	0.13	1.11	11.8%
	Pyroxene & amphibole	0.00	0.00	-	0.00	0.00	-	0.00	0.00	-	0.23	12.68	1.8%	0.01	0.01	109.5%
	Biotite amphibole intergrowth	0.00	0.00	-	0.00	0.00	-	0.00	0.00	-	0.27	15.34	1.8%	0.00	0.00	-
	Fe-Mn oxides carbonates	0.00	0.00	244.9%	0.23	0.93	24.5%	0.07	0.12	58.7%	0.00	0.01	35.0%	0.06	0.34	17.9%
	Carbonates	0.01	0.03	36.5%	0.01	0.04	19.6%	0.01	0.07	10.5%	0.04	0.93	4.1%	0.01	0.02	63.8%
	Chlorite	0.01	0.13	8.2%	0.09	1.62	5.8%	0.10	0.60	16.0%	0.09	2.48	3.5%	0.08	1.27	6.4%
	Pyrite	0.00	0.00	-	0.01	0.01	122.5%	0.37	1.93	18.9%	0.69	2.81	24.7%	0.01	0.02	82.0%
	Titanite	0.00	0.01	0.0%	0.02	0.21	7.6%	0.04	0.42	10.2%	0.01	0.16	3.2%	0.02	0.13	18.2%
	Ilmenite/rutile	0.02	0.08	32.4%	0.01	0.08	9.2%	0.00	0.01	0.0%	0.05	0.76	6.8%	0.01	0.03	23.8%
	Apatite	0.01	0.03	36.9%	0.00	0.00	-	0.01	0.01	38.7%	0.01	0.10	8.8%	0.00	0.00	-
	Others	0.00	0.00	244.9%	0.00	0.01	49.0%	0.01	0.02	35.0%	0.01	0.12	11.1%	0.01	0.01	77.5%

Table 5.4: QEMSCAN measurement repeatability results.

Survey	Id															
	Name															
Sample	Name	RSD	AVG	RSD%	RSD	AVG	RSD%	RSD	AVG	RSD%	RSD	AVG	RSD%	RSD	AVG	RSD%
	Id	F	F	F	G	G	G	H	H	H	I	I	I	J	J	J
Field ID Number Final6	Name	LB4	LB4	LB4	LB2	LB2	LB2	LB15	LB15	LB15	LB9	LB9	LB9	LB10	LB10	LB10
Mineral Mass(%)	Quartz	1.50	17.84	8.4%	4.42	18.18	24.3%	4.54	27.28	16.6%	1.01	26.00	3.9%	0.56	25.96	2.1%
	Plagioclase	0.67	9.48	7.1%	1.27	12.23	10.4%	0.15	0.37	40.0%	1.75	7.13	24.5%	0.37	5.45	6.8%
	K Feldspar	0.81	12.40	6.5%	0.20	0.76	25.8%	2.60	28.58	9.1%	1.06	18.82	5.7%	0.62	22.98	2.7%
	Muscovite	0.05	0.67	8.0%	0.01	0.17	6.0%	3.00	11.08	27.1%	0.07	0.27	24.3%	0.03	0.28	9.1%
	Biotite	1.83	23.97	7.6%	1.50	12.53	12.0%	0.65	2.17	29.9%	1.49	6.67	22.3%	0.28	3.22	8.7%
	Glauconite	0.03	0.39	6.8%	0.05	0.32	17.1%	0.01	0.02	38.7%	0.03	0.07	44.6%	0.00	0.01	33.2%
	Illite	0.25	12.09	2.1%	0.21	2.70	7.8%	1.89	27.61	6.8%	0.94	17.51	5.4%	0.36	15.46	2.3%
	Kaolinite	1.49	9.62	15.5%	0.43	7.77	5.5%	0.14	2.09	6.8%	0.23	6.94	3.4%	0.39	3.37	11.6%
	Pyroxene & amphibole	0.00	0.00	331.7%	0.02	0.04	54.7%	0.00	0.00	-	0.01	0.01	79.3%	0.01	0.01	37.0%
	Biotite amphibole intergrowth	0.00	0.00	-	0.00	0.00	331.7%	0.00	0.00	-	0.01	0.01	77.1%	0.01	0.03	27.0%
	Fe-Mn oxides carbonates	0.44	0.73	60.0%	0.39	0.60	65.5%	0.02	0.01	219.1%	0.01	0.00	237.1%	0.01	0.00	138.7%
	Carbonates	0.05	0.05	104.1%	0.02	0.03	61.6%	0.01	0.02	50.0%	0.03	0.10	26.9%	0.06	0.33	16.8%
	Chlorite	0.91	3.46	26.3%	0.72	4.63	15.5%	0.02	0.09	24.7%	0.44	0.90	49.0%	0.51	2.71	19.0%
	Pyrite	0.99	0.42	233.0%	0.74	2.15	34.3%	0.00	0.00	-	0.00	0.00	-	0.00	0.00	-
	Titanite	0.03	0.07	35.7%	0.01	0.09	12.2%	0.01	0.01	79.3%	0.01	0.02	34.6%	0.03	0.10	26.4%
	Ilmenite/rutile	0.02	0.06	36.4%	0.03	0.16	20.2%	0.02	0.03	82.2%	0.00	0.00	-	0.00	0.00	-
	Apatite	0.00	0.00	-	0.00	0.00	-	0.03	0.04	67.5%	0.07	0.13	58.2%	0.04	0.12	33.3%
	Others	0.01	0.03	44.3%	0.01	0.02	39.8%	0.01	0.01	79.3%	0.01	0.01	108.1%	0.03	0.08	37.1%
Field number random 6 from 63	**Name**															
Mineral Mass(%)	Quartz	1.09	17.68	6.1%	3.63	17.66	20.6%	2.98	27.30	10.9%	0.83	25.98	3.2%	0.64	26.01	2.5%
	Plagioclase	0.49	9.44	5.2%	0.80	12.37	6.4%	0.15	0.36	41.7%	1.33	7.08	18.8%	0.34	5.40	6.3%
	K Feldspar	0.38	12.45	3.0%	0.30	0.77	39.2%	1.69	28.56	5.9%	0.68	18.84	3.6%	0.66	23.03	2.8%
	Muscovite	0.04	0.66	6.0%	0.01	0.17	8.3%	1.90	10.88	17.4%	0.06	0.27	21.4%	0.03	0.28	12.1%
	Biotite	1.65	23.88	6.9%	0.85	12.42	6.8%	0.54	2.18	24.8%	0.99	6.65	14.9%	0.45	3.22	13.8%
	Glauconite	0.02	0.38	5.9%	0.05	0.31	15.4%	0.01	0.02	31.6%	0.03	0.07	38.3%	0.00	0.01	0.0%
	Illite	0.26	12.03	2.2%	0.19	2.68	7.2%	1.99	27.81	7.2%	0.70	17.61	4.0%	0.29	15.46	1.9%
	Kaolinite	1.61	9.93	16.3%	0.34	7.79	4.3%	0.09	2.09	4.4%	0.28	6.94	4.0%	0.55	3.34	16.5%
	Pyroxene & amphibole	0.00	0.00	331.7%	0.02	0.04	40.3%	0.00	0.00	331.7%	0.00	0.01	64.2%	0.01	0.01	35.9%
	Biotite amphibole intergrowth	0.00	0.00	-	0.00	0.00	331.7%	0.00	0.00	-	0.01	0.01	59.3%	0.01	0.03	25.6%
	Fe-Mn oxides carbonates	0.46	0.70	65.3%	0.29	0.59	50.1%	0.02	0.01	219.1%	0.01	0.00	185.4%	0.00	0.00	222.5%
	Carbonates	0.15	0.09	159.7%	0.01	0.03	39.4%	0.01	0.02	39.8%	0.02	0.10	22.8%	0.06	0.34	17.9%
	Chlorite	0.56	3.44	16.1%	0.60	4.70	12.9%	0.02	0.09	25.2%	0.43	0.88	48.6%	0.38	2.74	13.9%
	Pyrite	0.63	0.44	141.8%	0.53	2.15	24.5%	0.00	0.00	-	0.00	0.00	-	0.00	0.00	-
	Titanite	0.03	0.07	34.5%	0.01	0.09	11.7%	0.00	0.01	64.2%	0.01	0.02	44.4%	0.03	0.10	26.9%
	Ilmenite/rutile	0.02	0.07	35.1%	0.03	0.16	17.5%	0.02	0.03	79.1%	0.00	0.00	-	0.00	0.00	-
	Apatite	0.00	0.00	-	0.00	0.00	-	0.02	0.04	39.8%	0.06	0.13	43.7%	0.05	0.12	38.9%
	Others	0.02	0.02	80.2%	0.01	0.02	50.0%	0.01	0.01	105.9%	0.01	0.01	88.9%	0.02	0.08	32.3%
Field ID Number Final12	**Name**															
Mineral Mass(%)	Quartz	0.67	17.85	3.8%	2.12	18.17	11.6%	2.97	27.29	10.9%	0.50	26.00	1.9%	0.39	25.97	1.5%
	Plagioclase	0.31	9.44	3.3%	0.62	12.24	5.1%	0.12	0.37	33.5%	1.15	7.12	16.2%	0.14	5.45	2.7%
	K Feldspar	0.23	12.38	1.8%	0.13	0.77	16.5%	1.82	28.58	6.4%	0.82	18.82	4.4%	0.30	22.98	1.3%
	Muscovite	0.03	0.67	4.5%	0.00	0.17	2.4%	1.95	11.08	17.6%	0.05	0.27	20.2%	0.01	0.28	4.2%
	Biotite	1.21	23.99	5.0%	1.17	12.53	9.3%	0.36	2.17	16.5%	1.45	6.66	21.8%	0.11	3.22	3.5%
	Glauconite	0.01	0.39	3.3%	0.02	0.32	6.6%	0.01	0.02	31.6%	0.03	0.07	37.5%	0.00	0.01	0.0%
	Illite	0.16	12.09	1.3%	0.16	2.70	6.1%	1.48	27.61	5.4%	0.61	17.51	3.5%	0.31	15.46	2.0%
	Kaolinite	0.81	9.59	8.4%	0.33	7.77	4.2%	0.12	2.08	5.6%	0.16	6.94	2.3%	0.33	3.37	9.8%
	Pyroxene & amphibole	0.00	0.00	-	0.01	0.04	19.6%	0.00	0.00	-	0.00	0.01	49.0%	0.00	0.01	0.0%
	Biotite amphibole intergrowth	0.00	0.00	-	0.00	0.00	-	0.00	0.00	-	0.00	0.01	19.4%	0.01	0.03	19.4%
	Fe-Mn oxides carbonates	0.38	0.73	52.4%	0.31	0.61	51.9%	0.02	0.01	137.3%	0.00	0.00	244.9%	0.01	0.01	109.5%
	Carbonates	0.04	0.04	85.9%	0.01	0.03	26.6%	0.00	0.02	18.8%	0.02	0.10	19.1%	0.04	0.34	10.5%
	Chlorite	0.87	3.48	25.1%	0.47	4.64	10.1%	0.02	0.09	17.4%	0.36	0.90	39.5%	0.22	2.71	8.2%
	Pyrite	0.79	0.43	184.2%	0.46	2.15	21.5%	0.00	0.00	-	0.00	0.00	-	0.00	0.00	-
	Titanite	0.01	0.07	15.4%	0.01	0.09	11.1%	0.00	0.01	49.0%	0.01	0.02	22.1%	0.02	0.10	23.6%
	Ilmenite/rutile	0.02	0.06	26.4%	0.01	0.16	7.4%	0.01	0.03	34.7%	0.00	0.00	-	0.00	0.00	-
	Apatite	0.00	0.00	-	0.00	0.00	-	0.01	0.04	35.3%	0.06	0.13	46.8%	0.01	0.12	9.9%
	Others	0.01	0.02	22.8%	0.01	0.02	31.6%	0.01	0.01	77.5%	0.00	0.01	0.0%	0.01	0.08	15.8%
Field number random 12 from 63	**Name**															
Mineral Mass(%)	Quartz	1.08	17.68	6.1%	3.46	17.68	19.6%	2.42	27.31	8.9%	0.55	25.98	2.1%	0.52	26.00	2.0%
	Plagioclase	0.51	9.44	5.5%	0.76	12.37	6.1%	0.07	0.36	20.6%	0.43	7.08	6.1%	0.20	5.41	3.8%
	K Feldspar	0.18	12.46	1.5%	0.25	0.77	33.0%	1.47	28.55	5.2%	0.37	18.84	1.9%	0.33	23.03	1.5%
	Muscovite	0.04	0.66	5.9%	0.01	0.17	7.9%	1.49	10.89	13.7%	0.03	0.27	11.4%	0.02	0.28	6.6%
	Biotite	1.68	23.87	7.0%	0.79	12.42	6.4%	0.34	2.17	15.4%	0.63	6.65	9.5%	0.31	3.22	9.7%
	Glauconite	0.02	0.38	4.7%	0.03	0.31	10.7%	0.00	0.02	18.8%	0.01	0.07	20.5%	0.00	0.01	0.0%
	Illite	0.21	12.04	1.8%	0.16	2.68	5.8%	0.95	27.80	3.4%	0.41	17.61	2.3%	0.24	15.46	1.6%
	Kaolinite	1.56	9.96	15.6%	0.29	7.79	3.7%	0.08	2.09	3.8%	0.19	6.94	2.8%	0.36	3.34	10.8%
	Pyroxene & amphibole	0.00	0.00	223.6%	0.01	0.04	27.4%	0.00	0.00	-	0.00	0.01	0.0%	0.00	0.01	35.0%
	Biotite amphibole intergrowth	0.00	0.00	-	0.00	0.00	-	0.00	0.00	-	0.00	0.01	0.0%	0.01	0.02	22.1%
	Fe-Mn oxides carbonates	0.15	0.69	22.4%	0.17	0.59	28.7%	0.02	0.01	154.9%	0.00	0.00	244.9%	0.01	0.00	154.9%
	Carbonates	0.11	0.09	125.0%	0.01	0.03	21.1%	0.01	0.02	22.1%	0.01	0.10	11.9%	0.06	0.34	17.5%
	Chlorite	0.46	3.43	13.3%	0.35	4.69	7.5%	0.02	0.09	17.4%	0.28	0.88	31.9%	0.28	2.74	10.4%
	Pyrite	0.35	0.44	80.6%	0.45	2.15	21.1%	0.00	0.00	-	0.00	0.00	-	0.00	0.00	-
	Titanite	0.02	0.07	31.1%	0.01	0.09	8.5%	0.00	0.01	0.0%	0.00	0.02	18.8%	0.01	0.10	14.1%
	Ilmenite/rutile	0.01	0.07	17.5%	0.02	0.16	13.8%	0.01	0.03	52.0%	0.00	0.00	-	0.00	0.00	-
	Apatite	0.00	0.00	-	0.00	0.00	-	0.01	0.04	31.9%	0.03	0.13	23.8%	0.02	0.12	18.3%
	Others	0.01	0.03	51.6%	0.01	0.02	22.1%	0.01	0.01	77.5%	0.00	0.01	49.0%	0.02	0.08	21.3%
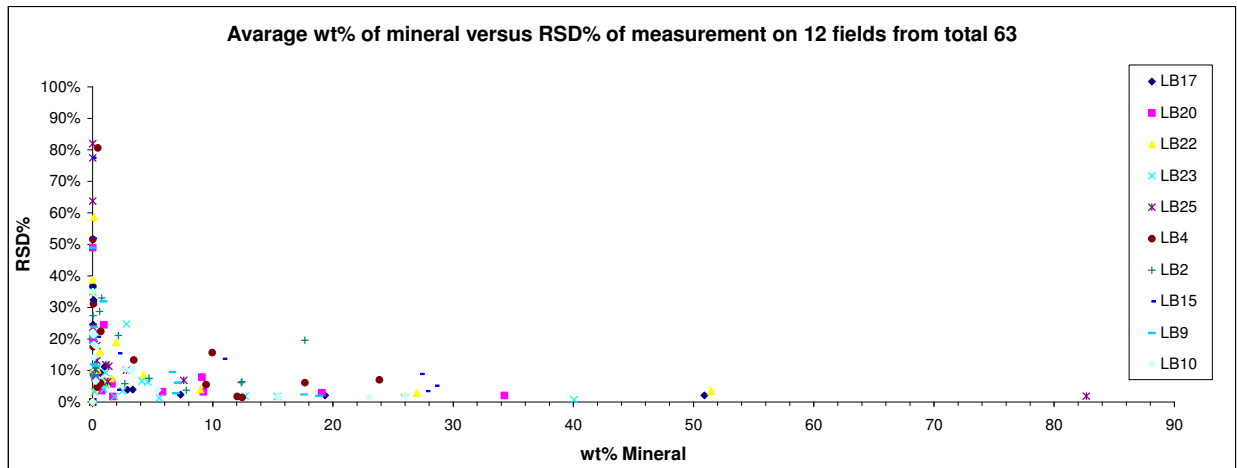
Figure 5.3: Example of RSD% for individual minerals in analyzed rock samples.

Powder diffraction analysis was used to double-check the main phases present and their relative proportions. Mineralogy established based on the XRD analysis are in good agreement with the QEMSCAN data but the unambiguous identification of sheeted silicates and clays was restricted due to the overlap of major peaks from the complex mixed samples in the interferogram. Based on the XRD no nahcolite was identified in any rock samples above the detection limits (Table 5.5).

Table 5.5: XRD data results.

Crystalline Mineral Assemblage (relative proportions based on peak height)

Sample	Major	Minor	Trace
LB2	plagioclase	muscovite/illite, biotite, kaolinite, quartz	*chlorite
LB4	quartz, plagioclase, K-feldspar, biotite	muscovite/illite	
LB9	quartz, plagioclase, K-feldspar, muscovite/illite	biotite	kaolinite
LB10	quartz, K-feldspar	plagioclase, muscovite/illite, kaolinite	
LB15	quartz, K-feldspar, muscovite/illite	plagioclase	
LB17	quartz, plagioclase	K-feldspar, muscovite/illite	
LB20	quartz, plagioclase, muscovite/illite	K-feldspar, biotite	kaolinite
LB22	quartz, muscovite/illite	plagioclase, K-feldspar	amphibole
LB23	plagioclase	quartz, biotite, kaolinite, amphibole	
LB25	quartz	plagioclase, K-feldspar, muscovite/illite	

* tentative identification due to low concentrations, diffraction line overlap or poor crystallinity

Figure 5.4: Example of the RSD% for individual minerals in analyzed rock samples. Major, minor and trace represent relative abundance in the sample while the numbers at the top of each column represent the exact modal percentage. Note that component standard deviations are proportional inversely to the square root of the number of particles available for analysis.

5.5   Discussion

Based on our results we can see that no significant Na-rich phases (Na above 5 wt. % in a mineral phase) apart from Na-plagioclase were identified through the studied samples. The only other phases identified to carry some amount of sodium were micas, clays and actinolite. Apart from sample LB22 and LB23 where the later mentioned phases account for around 14% and 6% of total Na respectively, the contribution of micas, clays and actinolite can be neglected (generally below 2 % combined). This indicates that nahcolite is not likely to be responsible for HCO_3^- rich paleofluids reported earlier at the Libčice gold deposit (Hrstka et al., 2011).

From the results on measurement repeatability we can infer that in the agreement with our previous work (Hrstka, 2008) the appropriate sampling strategy is the crucial parameter for obtaining representative quantitative data on mineralogy. Generally, RSD% for the analyzed rocks varies from 0.5 to 10% RSD for the major phases (above 5 wt %) but RSD variation is strongly dependent on the average particle size and sample texture (i.e. rock heterogeneity on a small scale). Random selection of analyzed fields from larger area of rock leads obviously to better results as it partly eliminates local in-homogeneities and gives results closer to the bulk mineral composition. In our specific case of 10 rocks from Libčice region, the area of 12 fields (size $1cm^2$ = representing single field size 2.5mm*2.5mm) seems to be sufficient for quantitative mineralogy analysis while 6 fields ($0.5cm^2$) shows quite significant decrees of reproducibility/repeatability of mineralogical analysis.

Comparison of the results to reported RSD data from thin section analysis and macarel analysis (Perring et al., 2004; Weltje et al., 2002) shows that in favorable cases and encountering relatively homogeneous fine grain rocks, the quantitative data for major phases are within 5%RSD. Nevertheless, for the accessory phases or rocks shoving different degree of heterogeneity, the analysis of thin sections to provide thoroughly quantitative data will be very costly in the term of instrument time. Similarly to the analysis of drill cuttings which is now becoming a successful technique in oil and gas wellcorrelations and reservoir evaluations more cost-effective way of analysis is thus the analysis of rock fragments with specified particle sizes (e.g. below 5mm). Such approach provides much more homogeneous and thus representative samples without the need for analyzing large area of the sample (Adamini and Hrstka, 2009; Sliwinski et al., 2009, 2010).

 We propose that QEMSCAN data measured in low resolution on an unknown sample can be used as a guide for the appropriate sample volume/area and/or required particle size in order to benefit fully from the truly quantitative modal mineralogy analysis. Minimum and maximum size of mineral grains and their mass distribution within the sample could then provide a lead for number of particles necessary to benefit fully from the truly quantitative automated mineralogy (Hrstka, 2008).

The very fine nature of analyzed rocks cause some minor issue in the mineral phase quantification both by manual and automatic means. Alteration and metamorphic reactions in rocks are also an issue especially for different degrees of alteration and the production of clay minerals (Haberlah et al., 2010, 2011; Brown and Petersen 2009).

From the point of view of textural analysis, the monomineral rock causes difficulties due to our inability to separate individual grains based on SEM-EDS spectra and established grain size and shape which are normally easily calculated from classical QEMSCAN data.

This technique provides definite advantages over classical optical microscopy because of the higher resolution of SEM and the ability to distinguished even tiny mineral grains based on their chemistry (e.g. cordierite from quartz and feldspars on a few micron scale). Also the quantitative information on the modal mineralogy which is tedious and hard to obtain by point counting or laborious optical image analysis can be obtained in a matter of minutes with precision much higher then that of classical point counting (Hrstka, 2008). The detection limits for specific minerals depends greatly on the form of occurrence and the space distribution of any phase of interest (Hrstka, 2008). Generally speaking, the fine grained rock quantities of minerals down to 0.5% can be usually recorded with good reproducibility and repeatability of data (Hrstka, 2008). The approximation of precision of modal analysis can be based on the number of analyzed particles of each mineral of interest and their size distribution. Over 1000 parties are usually enough to provide the representative data on modal composition if their minimum and maximum sizes are comparable.

Automatic comparison of mineralogical data with rock chemistry can help dramatically with evaluation of modal mineralogy and prove the validity of elemental deportment data which are routinely calculated from QEMSCAN analysis. Due to the high dependence of RSD on the form of occurrence of a specific mineral and the rock heterogeneity in general, the evaluation against independent chemical assays has remained the best available approach yet.

According to our data, the QEMSCAN provides better results on quartz content determination of shales and similar rocks than various recalculations of whole rock geochemical analysis which could lead to erroneous results due to variability in Al/Si ratios in individual clay minerals (and in other unaccounted silicates) (Ross and Bustin, 2006; Sliwinski et al., 2010).

Main interferences and comparison with optical microscopy/other techniques

The main problem associated with the analysis of rocks in thin sections is still the unambiguity in the analysis of some complex series of rock forming minerals and clays. As a matter of fact, the

current QEMSCAM system is not capable of identifying the presence of water or OH in the mineral structure and, as usual for EDS systems, its resolution in the range of light elements is restricted. Some of these problems can be easily overcome by the use of theoretical formulas obtained from book reference or independent analysis but this is not always a trivial approach especially for above-mentioned members of solid solutions (Grauch et al., 2008).

The presence of high proportion of boundary phases and the identification of mineral mixtures/fine intergrowths (below 2um) from an individual mineral phases is also limiting in some regards mainly for very fine grain rocks.

The observed mixtures include pares like:

Biotite + actinolite= pyroxene (biotitization of actinolite)

Micas = altered feldspars

Illite= feldspar + quartz

Organic compounds in shales = chamosite

It should be noted that the resolution of SEM and EDS is nevertheless much better than classical petrological investigation and can distinguish high number of mineral with ease compared to laborious polarized light practice.

An introduction of "mixture analysis routine" into the system in the future could be a possible solution. Also an integration of data from an additional technique like Raman spectroscopy or polarized light optical image analysis etc. could be considered. The limitations of such approach is unfortunately limited due to the current low level of automatization of such integrated approach.

Carbon observed as miniature inclusions in black shales and quartzite's was not unambiguously identified by QEMSCAN due to the classical problems related to epoxi resin, carbon coating and low sensitivity of EDS to light elements (Creelman and Ward, 1996). Even though the organic carbon content seems to be generally underestimated by QEMSCAN compared to optical observation (optical microscopy) there is still a good correlation between the relative carbon content while the shales and quartzite show the highest C content. For proper quantification of carbon content the adopting of a coal analysis approach with lower EV and other QEMSCAN parameter settings could be performed if required (Lui et al., 2005; Van Alphen, 2006)

It has been shown that visual or even automated comparison of data from optical microscopy and QEMSCAN could be misleading. This is due to incorporating of information from the whole thickness of the section/ specimen in the case of optical microscopy versus reflected (only real information from 2D surface of the sample) character of SEM/QEMSCAN analysis. The first

mentioned incorporates projection of information from the whole thickness (30-45um) of the section/specimen while the second represents only the information from 2D surface (2-5um) of the sample. This could lead to different modal abundances calculated based on optical and e-beam techniques especially for opaque minerals and fine-grained mixtures.

5.6   Conclusions

Fast mineralogical and petrological analysis is easily achievable with the QEMSCAN system. 2.5 to 1.5 cm thin sections were analyzed in 7h as an average with a resolution of 10um representing over 3000000 analytical points per section/block with the old platform (QEMSCAN E-series instrument fitted with 4 SIRIUS 10/SUTW detectors). This converts to probably less then 4h of analytical time with the currently available SDD fitted systems. One fourth of the whole thin section (1h measurement) seems adequate for quantitative modal analysis in studied rocks.

QEMSCAN proved to be a good method for modal mineralogy determination on the fine grained rocks and suitable technique for searching for specific minerals of interest present in low quantities in fine grained rocks.

Sodium distribution in all studied rocks was attributed almost solely to Na-plagioclase. No presence of nahcolite or other Na-rich phases was confirmed in the studied samples.

Interferences and unambiguity of recognition of very fine-grained mineral intergrowth (-1um grains in aggregates) cause the main difficulty in the precise modal mineralogy calculation.

Such interferences and boundary phase presence could be solved by SIP editing and reclassification (introducing the mixtures with average chemistries) but are generally time consuming and labor intense.

Automated expert system (computer aided SIP generator) dealing with mixtures of common rock forming mineral could be suggested as a step towers the fully automated mineralogical analysis of fine-grained rocks.

The sample heterogeneity which could be inferred from minimum and maximum grain sizes of specific mineral and their abundances plays the crucial role in estimating reproducibility of modal mineralogy. For all the studied rock samples RSD% was generally better than 10% for the main minerals. The problematic separation of touching particles/grains is the main problem for a particle counts estimations in monomineralic rocks. The combination of techniques is recommended to overcome this problem. Due to these limitations the evaluation against independent chemical assays remains the best available approach.

The random field measurements generally provide better reproducibility due to the randomization of heterogeneous samples.

It seems likely that technologies based on scanning electron microscopy with linked energy dispersive spectrometers have the potential to revolutionize the quantitative mineralogy and can be used in applied and classical geology for the rock classification and petrological analysis.

Acknowledgements

6. PRELIMINARY RESULTS ON THE REPRODUCIBILITY OF SAMPLE PREPARATION AND QEMSCAN MEASUREMENTS FOR HEAVY MINERAL SANDS SAMPLES (ARTICLE 4)

Tomáš Hrstka[1,2],

[1] *SGS Minerals Services, Advanced Mineralogical Network, (Brisbane Facility), 2/27 Mayneview Street, Milton, QLD 4064, Australia, tomas.hrstka@sgs.com*

[2] *Institute of Geology AS CR, v.v.i., Rozvojová 269, CZ-165 00 Prague 6 – Lysolaje, Czech Republic*
*E-mail: **hrstka@gli.cas.cz***

Abstract

QEMSCAN technology is a widely accepted automated e-beam technique providing quantitative and statistically robust mineralogical data to the mining industry. It uses X-ray mapping combined with BSE brightness to identify minerals in almost any type of geological material (Gottlieb et al. 2000). Besides the modal mineralogy also the liberation, associations, average grain size and other textural information can be obtained. The aim of this study is to test reproducibility of this technique by setting up and running standard tests on different QEMSCAN systems.

Multiple sample blocks were prepared by our standard operating procedure as epoxy-mounted, carbon-coated, polished blocks. The replicates were measured under the same conditions and measurement parameter settings on different QEMSCAN instruments. The relative standard deviation (RSD) for the set of measurements was calculated. Generally the reproducibility of the systems themselves was found to be excellent ranging between 0.4 - 1.5 % RSD.

The more significant change in the reproducibility was found to be caused potentially by the sample preparation and variation in the mineralogy of the replicates. The measurement parameter settings together with these variations can account for almost 15 % RSD for minerals of low abundance. Still sufficient results for the main phases present in quantities higher than 2 - 5 wt % of the total mass of the sample were confirmed.

Following the experiments the parameters having the biggest influence on the performance of the QEMSCAN and its precision are discussed in detail. The importance of the sample preparation procedures and measurement parameter settings is emphasized. It is shown that experience and excellence is necessary for getting the most from the automatic mineralogical methods like QEMSCAN.

6.1   Introduction

QEMSCAN (Quantitative Evaluation of Minerals Using Scanning Electron Microscopy) is an automatic image analysis e-beam technique combining purpose built SEM hardware and software to produce digital images of mineral phases or man-made materials. Identification of the individual phases is based on combination of X-ray spectra fingerprint, element peak ratios and BSE image brightness representing the average atomic weight of the material. The subsequent processing of the collected images provides quantitative data on the mineral compositions, proportions, distributions, associations, and liberation of the minerals present as well as an average particle and grain sizes (Latti et al., 1997; Gottlieb et al., 2000; Pirrie et al., 2000) Since the QEMSCAN distinguishes the different phases based on the correlation of X-ray spectra to a chemical composition of the mineral species it can be used to identify a wide variety of materials while the detail of information obtained could be task specific. For the purposes of specific analysis of unknown samples, mixed phases and solid solutions, the spectral database used for phase identification (SIP) can be updated and refined to cope with complex ores and unusual mineral chemistries. Additional element information can by obtained from EDX, WDS or other point analysis methods to account for elements occurring in solid solution or within a series of alteration products in trace amounts.

For quality control purposes the accuracy and reliability of the data is usually checked against independent chemical assay data and/or another independent method such as (quantitative) X-ray diffraction analysis in the case of main minerals. Assay comparison is based on automatically calculated theoretical chemical assays using the chemical composition of individual minerals, together with the results of modal analysis. This helps to check whether the appropriate chemistry was assigned to minerals based on their spectral fingerprint in the database definition (represented by X-ray peak ratios).

As quantitative mineralogical characterization is now understood to be an essential prerequisite for exploration and exploitation of mineral deposits, the QEMSCAN is now used almost routinely for the analysis of heavy mineral sand samples and plant products (Nevertheless, information on the precision and accuracy of the automated mineralogy measurements has not been widely reported. This paper describes the results of QEMSCAN test measurements on heavy mineral sand samples (standard multiple replicates and repeat measurements for heavy mineral sand samples) with the aim of calculating the repeatability and reproducibility of the measurements for specific samples. The main parameters which affect the analysis precision of QEMSCAN measurements are discussed.

6.2   Methods and Samples

Polished sections of typical heavy mineral samples were prepared by our internal procedure, which includes representative splitting by rotary riffler, mixing with fine graphite and mounting in an

epoxy block. A variety of precautions were taken to prevent the settling of the particles and ensure their homogenous distribution. The samples were finally ground, polished and carbon coated to produce polished blocks suitable for QEMSCAN analysis. For the test measurements more than 10 replicates of the same sample were prepared. The typical mineral composition and QEMSCAN chemical assays are provided in Table 6.1.

All the samples were analysed by the QEMSCAN E-series and 310-series instruments fitted with 4 or 3 Sirius series - Si(Li) detectors (SIRIUS 10/SUTW). All the test measurements were run at 25keV with 5 nA beam current.

For comparison purposes, different QEMSCAN measurement modes were used for the analysis of the samples including BMA (Bulk Mineral Analysis) and PMA (Particle Mineral Analysis).

The PMA method involves scanning of the electron beam across all the particles in the sample with selected spacing of the points which can vary from 0.2 to 25μm (Pirrie et al., 2000). This type of measurement will produce colour-coded digital particle maps representing mineral composition. Such data provide not only the modal mineralogy but also liberation and locking data and textural information. Example particle maps are presented in Table 6.1 For these measurements, a 2.5μm pixel size was selected giving more than 3 million X-ray point analyses within more than 500 mineral particles in a single sample.

The BMA analysis is a fast line scan method similar in some ways to advanced point counting. BMA uses length of intercepts within the mineral species in a regular grid. Parameters like specific pixel (point) spacing and line spacing can be varied to suit the specific requirements of the analysis. The resulting data can be used to accurately quantify the bulk mineral composition of the sample. Typically in our samples more than 0.5 million X-ray points (or about 14000 particles) per block will be analysed for a fast 30 minute measurement with a point spacing of 5μm and line spacing 150μm. This gives an excellent statistical population for subsequent processing.
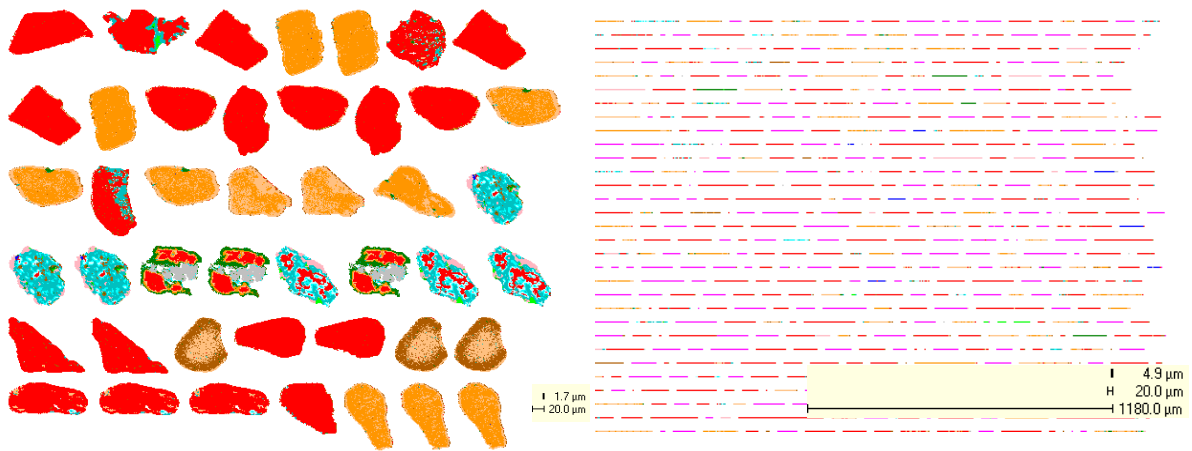
Figure 6.1: Example of the data output for multiple PMA and BMA measurements.

6.3   Results

The BMA and PMA measurements were performed on numerous samples to obtain information on "repeatability" (the variation arising when all efforts are made to keep conditions constant during a short time period) and "reproducibility" (the variation arising using the same measurement process among different instruments and operators, and over longer time periods). Relative standard deviation (RDS) for the measurements on the same QEMSCAN system and different models of QEMSCAN system was obtained. Modal mineralogy and average particle sizes were calculated from both types of measurements used for data variation validation. The results of the modal analysis and average grain size estimations are presented in the Table 6.1 and Table 6.2. Please note that not all the minerals analysed are included in the table.

The reproducibility of the whole automated mineralogy analytical process including the sample preparation and sampling of complex mineralogical sample was also studied. This was done by setting up and running standard samples prepared and measured during an extended period of time.

Table 6.1: QEMSCAN measurement repeatability results.

Replicate	Name	Block A				Block B				Block C		
	Measurement Type		BMA				BMA				BMA	
3*10 repeated analysis on the identical block	Measurement Name	average	2SD	2RSD%		average	2SD	2RSD%		average	2SD	2RSD%
	Particle Size	**128.24**	0.34	0.3%		**122.33**	0.28	0.2%		**121.77**	0.17	0.1%
Elemental Mass (%)	Al (QEMSCAN)	**1.05**	0.01	0.7%		**1.10**	0.01	0.7%		**1.16**	0.01	0.7%
	Si (QEMSCAN)	**7.04**	0.01	0.1%		**7.39**	0.01	0.1%		**7.18**	0.01	0.2%
	Ti (QEMSCAN)	**33.09**	0.01	0.0%		**32.14**	0.01	0.0%		**32.58**	0.03	0.1%
	V (QEMSCAN)	**0.04**	0.00	0.9%		**0.04**	0.00	0.9%		**0.04**	0.00	1.2%
	Cr (QEMSCAN)	**0.08**	0.00	1.4%		**0.05**	0.00	3.0%		**0.03**	0.00	4.5%
	Mn (QEMSCAN)	**0.09**	0.00	0.5%		**0.09**	0.00	0.5%		**0.09**	0.00	0.6%
	Fe (QEMSCAN)	**2.69**	0.01	0.5%		**2.71**	0.01	0.5%		**2.82**	0.01	0.4%
	Zr (QEMSCAN)	**15.47**	0.01	0.1%		**15.79**	0.01	0.1%		**15.40**	0.01	0.1%
Mineral Mass (%)	Rutile	**44.98**	0.03	0.1%		**43.18**	0.03	0.1%		**43.62**	0.06	0.1%
	Leucoxene	**6.88**	0.05	0.7%		**7.14**	0.05	0.7%		**7.27**	0.04	0.6%
	Ilmenite	**5.62**	0.04	0.7%		**5.49**	0.05	1.0%		**5.70**	0.05	1.0%
	Ti Al Fe Oxides	**2.30**	0.05	2.0%		**2.29**	0.05	2.2%		**2.27**	0.05	2.1%
	Zircon	**31.09**	0.03	0.1%		**31.73**	0.02	0.1%		**30.95**	0.02	0.1%
	Monazite	**0.75**	0.01	1.8%		**0.84**	0.01	1.7%		**0.78**	0.01	1.9%
	Chromite	**0.21**	0.00	1.1%		**0.13**	0.00	2.3%		**0.08**	0.00	2.3%
	Quartz	**2.32**	0.01	0.2%		**2.66**	0.01	0.4%		**2.44**	0.01	0.3%
	Al Silicates	**1.32**	0.01	0.5%		**1.12**	0.02	1.4%		**1.30**	0.01	0.6%
	Al Fe Silicates	**1.57**	0.01	0.5%		**2.03**	0.02	1.0%		**1.94**	0.01	0.6%
Grain Size	Rutile	**85.91**	0.56	0.7%		**79.52**	0.81	1.0%		**77.65**	0.64	0.8%
	Leucoxene	**21.09**	0.21	1.0%		**21.73**	0.27	1.2%		**20.83**	0.38	1.8%
	Ilmenite	**25.86**	0.38	1.5%		**26.35**	0.61	2.3%		**25.39**	0.63	2.5%
	Ti Al Fe Oxides	**9.68**	0.12	1.2%		**9.83**	0.12	1.2%		**9.63**	0.11	1.1%
	Zircon	**104.40**	0.48	0.5%		**99.81**	0.66	0.7%		**100.71**	0.48	0.5%
	Monazite	**60.05**	4.48	7.5%		**50.26**	3.25	6.5%		**48.29**	3.49	7.2%
	Chromite	**123.94**	12.41	10.0%		**98.09**	22.14	22.6%		**117.27**	19.94	17.0%
	Quartz	**82.24**	2.75	3.3%		**80.50**	1.72	2.1%		**72.84**	1.15	1.6%
	Al Silicates	**65.82**	2.44	3.7%		**46.64**	2.75	5.9%		**55.11**	1.64	3.0%
	Al Fe Silicates	**47.00**	1.42	3.0%		48.32	1.31	2.7%		**46.63**	1.81	3.9%

Table 6.2: QEMSCAN measurement repeatability results.

Replicate	Name	Section 1				Section 2				Section 3		
	Measurement Type		BMA				PMA				BMA	
	Measurement Name	average	2SD	2RSD%		average	2SD	2RSD%		average	2SD	2RSD%
Mineral Mass (%)	Rutile	**45.01**	0.55	1.2%		**46.57**	0.20	0.4%		**43.94**	1.58	3.6%
	Leucoxene	**6.78**	0.26	3.8%		**7.01**	0.01	0.2%		**7.09**	0.33	4.7%
	Ilmenite	**5.74**	0.20	3.5%		**4.54**	0.42	9.3%		**5.60**	0.18	3.2%
	Ti Al Fe Oxides	**2.31**	0.06	2.4%		**1.43**	0.09	6.3%		**2.29**	0.05	2.3%
	Zircon	**31.04**	0.64	2.1%		**29.39**	0.95	3.2%		**31.27**	0.69	2.2%
	Monazite	**0.76**	0.02	2.6%		**0.50**	0.23	46.9%		**0.79**	0.08	10.1%
	Chromite	**0.21**	0.01	3.3%		**0.60**	0.05	8.0%		**0.14**	0.10	74.5%
	Quartz	**2.32**	0.04	1.7%		**1.61**	1.09	67.5%		**2.47**	0.30	12.0%
	Al Silicates	**1.18**	0.21	17.3%		**2.81**	0.14	5.1%		**1.24**	0.18	14.7%
	Al Fe Silicates	**1.56**	0.05	3.3%		**2.52**	0.33	13.1%		**1.84**	0.41	22.5%
Grain Size	Rutile	**84.73**	1.82	2.1%		**63.61**	1.02	1.6%		**81.14**	7.24	8.9%
	Leucoxene	**20.88**	0.73	3.5%		**10.96**	0.74	6.7%		**21.23**	0.82	3.9%
	Ilmenite	**26.40**	1.02	3.9%		**10.70**	0.43	4.0%		**25.89**	0.95	3.7%
	Ti Al Fe Oxides	**9.60**	0.45	4.7%		**3.41**	0.04	1.1%		**9.72**	0.21	2.1%
	Zircon	**101.41**	4.98	4.9%		**90.34**	5.75	6.4%		**101.67**	4.13	4.1%
	Monazite	**57.76**	5.91	10.2%		**45.03**	2.38	5.3%		**53.02**	11.12	21.0%
	Chromite	**129.71**	27.58	21.3%		**127.73**	7.32	5.7%		**112.95**	28.86	25.5%
	Quartz	**74.08**	16.00	21.6%		**43.50**	19.39	44.6%		**78.73**	8.39	10.7%
	Al Silicates	**61.93**	5.48	8.8%		**62.39**	2.00	3.2%		**55.88**	16.41	29.4%
	Al Fe Silicates	**45.72**	2.51	5.5%		48.18	4.18	8.7%		**47.34**	2.08	4.4%

Measurements on the same system - Repeatability

Repeatability was tested on the same system by running three standard blocks 10 times each, while the measurement parameters kept constant over a one day period. The results on modal mineralogy and average particle sizes are shown in Table 6.1.

Measurement of on different systems - Reproducibility

In order to investigate the reproducibility of the systems, the same blocks were measured on two different QEMSCAN systems over a two week period and the data was compared. The sample block orientation was intentionally changed between the measurements to account for the variation within the block. The results of the measurements are presented in Section 1 of Table 6.2.

PMA measurements tests

For the comparison of PMA and BMA types of analysis, the same three blocks were measured six times each using the PMA mode of analysis. High resolution was used for the analyses, but, in order to save time, only parts of the block were analysed. The measurements were used for studying textural information and its effects on the analysis precision. As only limited numbers of particles were measured, sampling errors dominated the data validation results (Table 6.2 Section 2). The number of the particles analysed is indicated in the Figure 6.2 and Figure 6.3. All data was used to estimate the optimal number of particles analysed for the samples studied.
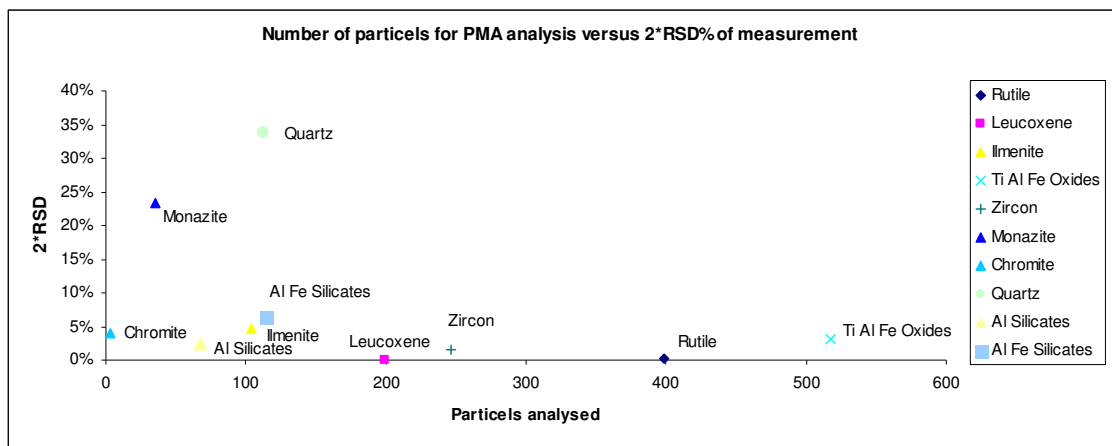

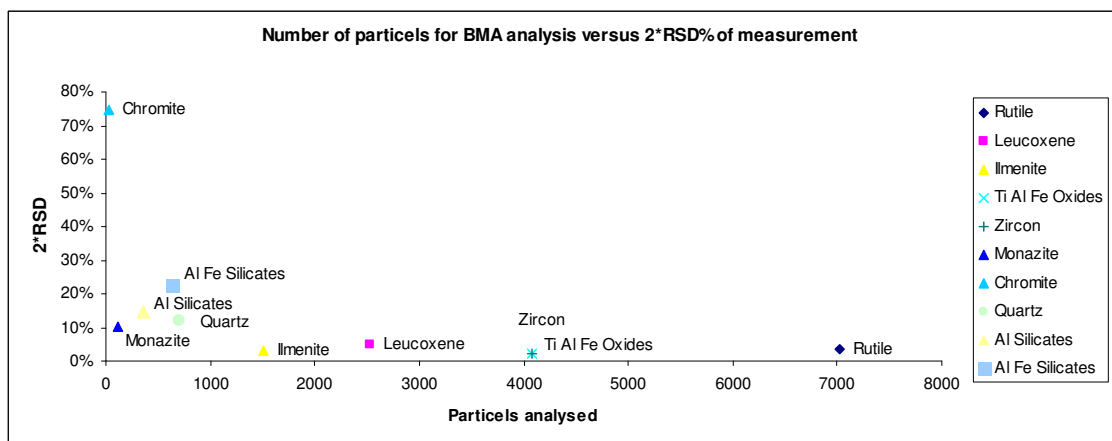**Figure 6.2:** RSD% versus number of particles analysed for QEMSCAN PMA measurement.

Figure 6.3: RSD% versus number of particles analysed for QEMSCAN BMA measurement.

Sample regrinding followed by re-analysis - Reproducibility of the whole automated mineralogy analytical process

The reproducibility of the whole automated mineralogy analytical process including the sampling (number of replicates), block preparation and measurement was performed by analyzing 10 replicates of the standard heavy mineral sections/blocks samples over an extended period of time. The overall information on the reproducibility of the sample preparation and analysis was obtained and is presented in Section 3 of Table 6.2.

For the illustrative purposes, the RSD% values for the individual minerals analysed were plotted against the number of particles containing the mineral of interest to see the effect of analysed particles on the measurement precision (Figure 6.2).

6.4   Discussion

As the precision and reproducibility of the QEMSCAN systems appears to be excellent for the selection of samples analysed, questions arise about appropriate sampling and sample preparation.

It was shown by the results of the test measurements that the amount of mineral in the sample and the particle complexity plays an important role in the precision and accuracy of the measurements as well as the repeatability and reproducibility of results. More abundant phases are essentially measured with higher confidence than minor and trace phases based simply on the presumptions of statistics and probability. This is consistent with other work done on mineral sampling (Pitard, 1993). The approach of solids sampling variance is beyond the scope of this study and the interested reader is referred to Lyman, 1998; Gy, 1979; Smith, 2001 for details on sampling errors. The rigorous amount of the sample to be analysed should also come up from the application of sampling theory (Lyman, 1998; Gy, 1979).

Our main intention was to monitor the precision of the QEMSCAN systems themselves and to identify the main sources of errors arising from the instrumentation. Still this information is valuable for comments on ideal amount of material (particles) to by analysed to take full advantage of the instrument precision.

The effect of textures on the results can be seen by comparing the results for quartz and Ti-Al-Fe oxides. In the samples analysed, quartz generally shows better results even with the same abundance in the sample due to its preferable particle size and shape. By examination of the particle maps of identical particles from different measurements, it was confirmed that the complex textures are more difficult to reproduce (less repeatable). Still the systems turn out to be excellent even for highly complex phases giving only slight variation of repeatability and reproducibility for texturally different occurring phases.

The difference between the PMA and BMA type of measurements, which is shown by the Table 6.2, represents only the advantage of analysing higher numbers of particles per sample. For the PMA analyses, only a few hundred particles for the main phases were analysed during 350 minute run compared to over 4000 particles in 25 minutes for the BMA. In other words, the reproducibility and repeatability for PMA and BMA data is identical. The big difference in the RSD calculated for the PMA, especially in case of monazite and quartz, shows the influence of big particles in the measurement similar to the nugget effect in gold analysis and leads back to the number of particles available for analysis.

Based on the Gy`s basic sampling equation (Smith 2001; Gy, 1978), the amount of the sample to be taken (number of replicates measured) to ensure the accuracy of the measurements will be controversial for our material and analysis as the amount of sample usually presented to the instrument in block mount is disputable, as well as its complexity. We can assume that requested sample weights will decrease rapidly with the decreasing maximum "top particle size" within the materials of the same complexity. The number of necessary blocks that need to be measured, to obtain a sufficient population of particles, is directly proportional to the maximum particle size and inversely proportional to the modal abundance of the minerals of interest.

 From the particle size perspective, particles in the range of less than 250μm will be preferable in terms of cost control and precision. It is worth noting that the development of robust statistical tools for the evaluation of the automated e-beam techniques like QEMSCAN will be complicated as the measurements are sample and potentially SIP dependent.

From our experiments (see Figure 6.2 and Figure 6.3) the recommended minimum number of particles that should be analysed to take advantage of the exact quantitative mineralogy is over 1000 on any mineral of interest. Still valid quantitative information can be obtained for minerals present with more than 100 particles with favourable textures and sample homogeneity.

 Apart from the sampling errors, the sample surface contamination and defects including bubbles, cracks and pluckouts can play a role in the repeatability of the sample preparation process. Nevertheless, the natural variation of composition for complex multiphase samples is more important and the sampling method and number of replicates analysed should be carefully selected for every specific task.

Sample preparation was shown to have a greater impact on the reproducibility of the data than the system stability limitations. However, the data quality is also highly dependent on the settings of the system and especially on the variations in measurement parameters or potential system instability. The recognised main parameters affecting the system performance will be appropriate SIP selection for non-routine samples, BSE calibration/stability, image focus, and X-ray detector calibration.

SIP database settings and optimization can play an important role in the quality of the data produced, and generally, SIPs that are poorly defined and/or BSE sensitive, are more prone to variation in the data produced. During our test measurements the main ambiguity in the mineral identification based on the SIP was arising from the stability and calibration of the BSE values for minerals with similar chemistry and only minor differences in BSE SIP definitions (less than 5 BSE units).

While analysing the same block more than 40 times even with the BSE sensitive SIP, no variation in mineralogy was observed if the system was closely monitored and carefully calibrated. This suggests that highly reproducible BSE data can be collected by QEMSCAN. There is also little potential danger of contamination of samples by dirt present in the SEM chamber precipitating on the sample surface exposed to the electron beam commonly found in imaging SEM microscopy which could potentially affect the BSE of mineral phases. Still, such contamination remains potential problem for BSE calibration standards. These are kept in the chamber for extensive period of time and used many times to calibrate the BSE values which mean they are exposed to the beam much more than the samples themselves. Regular renovation by polishing is recommended.

The potential stage tilt in the automatic SEM stage mechanisms and/or uneven samples and standards heights can lead to variation in analysis results for highly BSE sensitive SIPs, which can be more significant than other parameters. For measurements between different systems the BSE calibration can play an important role in the data precision if the response from different signal amplifiers is not following the same calibration curve. This potential problem is solved by system monitoring near the BSE of interest, or the software update allowing for even more precise BSE calibration with a three point calibration curve (Gottlieb, 2007). The BSE is generally more important for reproducibility of SMS/TMS (specific/trace mineral search) (Gottlieb et al., 2000) where the system is selecting the particles of interest based only on the BSE brightness.

During the test measurements, focus was monitored and identified as a potential variable causing incorrect BSE readings and inappropriate area measurements. Its effects needs to be further studied.

X-ray stability and detector health is an important parameter of measurement performance but was found to be negotiable for the test performed and the overall system performance if the standard detector health checks are performed regularly.

Monitoring of all above mentioned parameters is recommended for all analysis performed.

6.5   Conclusion

Excellent precision of both the instrument and the method was reported from the tests performed.

It was concluded that reproducibility of QEMSCAN measurements on heavy mineral samples is generally dependent on the type of sample (its distributional heterogeneity), measurement setting parameters and number of particles analysed. Appropriate sampling, measurement parameter setup and system monitoring is essential for obtaining the best results. For mineral phases with concentrations below 1% of the sample volume, the data should be considered only as indicative if the analyses are not optimised for their quantification. For accurate information on phases with low abundances, SMS/TMS measurements or high number of replicates are necessary to obtain reliable data. Extreme caution should be take for the BSE dependent measurements to ensure BSE calibration, focus and sample heights are set correctly.

The amount of the sample to be analysed to take the full advantage of system precision needs to be further examined. Improvements in understanding the precision and accuracy of automated mineralogy methods like QEMSCAN will be necessary in the future to put the appropriate quality control checks and standards in place to set up these highly valuable methods as a routine within their full potential.

Acknowledgements

7. X-RAY NANOTOMOGRAPHY IN FLUID INCLUSIONS STUDY (ARTICLE 5)

Tomáš Hrstka[1], and Jiří Zachariáš[1]

[1] *Charles University in Prague, Faculty of Science, Institute of Geochemistry, Mineralogy and Mineral Resources, Albertov 6, Praha 2, CZ-128 43, E-mail: zachar@natur.cuni.cz*

7.1 Introduction

In this preliminary study we have tested for the first time the application of the X-RAY NanoTomography as a tool for 3D visualization and volume reconstruction of aqueous and aqueous carbonic fluid inclusions. This method was tested in order to potentially provide exact volumes and fill ratios for aqueous and complex aqueous-carbonic gas bearing non-fluorescent fluid inclusions. Such data are of great importance for the PVTX thermodynamic modeling in fluid inclusion research (Bakker and Diamond, 2006; Grimmer et al., 2003; Tricart et al., 2000). As a part of this project also the potential for reconstruction of fluid inclusions trail geometry in 3D was tested.

7.2 Methods

X-RAY NanoTomography is a method, which use the combination of X-ray transmission technique with tomographical reconstruction by using the focused X-ray beam pointed on the sample, which rotates. The data are simultaneously recorded by CCD detector and transferred to the PC, which use the Cone-beam volumetric reconstruction algorithms (Feldkamp algorithm) for creation of the 3D image of the sample from the individual recorded 2D (radiography) sections (Skyscan, 1977). The great advantage of the NanoTomography is that it does not need any preparation, coating or vacuum treatment for the studied sample. The final images are a mixed combination of density and compositional information from the specimen (Baruchel et al., 2000; Skyscan, 1977). The maximal diameter of the sample is 10mm for SkyScan-2011 and about 50mm for SkyScan1172 where the resolution is about 150-250nm and 5um respectively (Skyscan, 1977).

All the measurements in this study were performed on NanoTomograph SkyScan-2011 in the SkyScan lab. Belgium.

7.3   Results

For our measurements the classical double polished thin sections prepared from the main quartz vein from the Libčice Gold deposit were used. Two Small broken chips containing numerous H_2O-CO_2-CH_4 and H_2O only inclusions were analyzed in order to obtain the accurate 3D volume reconstructions of individual fluid inclusions and the 3D space orientation and relationships of individual fluid inclusion secondary trails. The Imaris 4.0© software was used for data reduction, recalculation and 3D visualization. Some illustrative results, reconstruction images are shown on Figure 7.1 a, b. By this procedure we were able to visualize the individual fluid inclusions inside the quartz matrix and calculate their volume. In the inclusions containing two or more different phases only the difference between the host mineral and void space can be seen and no phase boundaries (H_2O liquid /H_2O vapor) were recognized. The additional tests are necessary to establish the precision of the calculation of inclusion volume and test the potential of this method for use in all other fluid inclusion host minerals
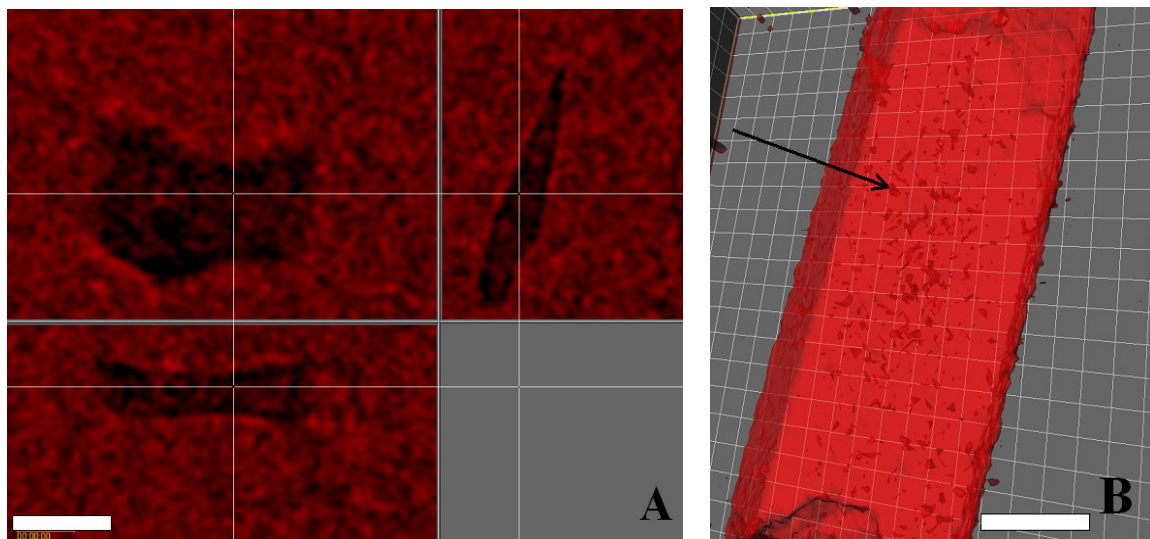
Figure 7.1: H_2O-CO_2 Fluid inclusions from the Libčice gold deposit visualized by nanoCT. A: xyz sections through H_2O-CO_2 inclusion in quartz (Scale 10um). B: 3D reconstruction of the part of thin section with numerous trapped fluid inclusions arrowed (Scale 150um).

7.4   Conclusions

We have demonstrated that the X-RAY NanoTomography is a suitable technique for 3D reconstruction and visualization of individual fluid inclusions in quartz and potentially all other inclusion host minerals including the opaque phases. There are some restrictions of its applicability so far related to its current resolution and problems related to limited use for visualization of materials with low-density difference. Nonetheless we can see the clear potential of this methodology and its applications for study of different geological samples non-destructively in 3D and on um scale (Van Geet et al., 2000; Tricart et al., 2000).

8.   GENERAL CONCLUSIONS

Multi-analytical approach was found to be invaluable for the accurate interpretation of complex paleofluids trapped in fluid inclusions from quartz gangue of Bohemian orogenic gold deposits. Besides the application of many techniques (optical microscopy, microthermometry, LA-ICP-MS, CL-SEM, SEM-EDS, QEMSCAN, CLSM and 3D nanotomography), this thesis focused on methodological developments of some of them (Raman spectrometry, automated mineral identification and inclusion volume/shape visualization).

A major improvement was achieved in the field of high-temperature Raman microspectrometry applied to the study of bicarbonate species in the aqueous phase of fluid inclusions. A new methodology is proposed for the calculation of bicarbonate and carbonate species concentrations. This allowed a later estimation of the pH of the trapped fluid phase.

We proved that Raman spectroscopy can be used for direct identification and potential quantification of bicarbonate species in natural fluid inclusions hosted in quartz.

This was demonstrated by Raman analysis of fluid inclusions from the Libčice gold deposit which revealed the presence of solid nahcolite (a daughter phase) and dissolved bicarbonate species in the aqueous phase. Bicarbonate concentrations vary from very low values up to about 20 wt. %. To best of our knowledge, our work represents the first known occurrence of bicarbonate species in natural fluid inclusions directly detected by Raman spectroscopy.

Until now, prevalence of Cl^- and other anions has been reported for hydrothermal paleofluids. Similarly, the majority of previous studies suggested acidic to neutral rather than the alkaline nature of fluids. Nevertheless, this indicates that the presence of bicarbonate ions in some environments is potentially more important than it was thought previously.

Confocal laser scanning microscopy and X-ray nanotomography were used for precise inclusion and bubble volume calculations, as well as for the visualization of non-fluorescent fluid inclusions in 3D space. Such data are necessary for the thermodynamic modeling of complex gas–aqueous mixtures (e.g., CO_2-CH_4-H_2O). The high spatial resolution of modern nano-CT systems allowed us to calculate volume for fluid inclusions down to a size of ~10 microns.

QEMSCAN technology can be used with many benefits for automated mineralogical and petrological investigations, providing data for modal mineralogy, textural analysis, rock identification and for a search for specific minerals in thin sections or rock fragments.

The case study of the Libčice orogenic gold deposit identified a globally unique example of post-entrapment modification of inclusion content by the hydrogen diffusion in fluid inclusions. This led to extreme variations in the CO_2/CH_4 ratio both at the scale of a quartz grain and at the scale of a mine. Based on Raman analysis, hydrocarbons that are present together with other organic matter

were identified as the most likely source of hydrogen. Hydrogen production was attributed to the thermal effect of the intrusion of the peripheral granite of the Central Bohemian Plutonic Complex.

9. REFERENCES:

Abbott et al., 1981. 13C nuclear magnetic resonance and Raman investigations of aqueous carbon dioxide systems

Adamini, P., Hrstka, T., 2009. Benefits of Upfront Mineralogy (QEMSCAN®) in Developing Metallurgical Testwork Programs for Uranium Ores; ALTA2009; International Nickel-Cobalt, Copper and Uranium Conference, conference proceedings.

Adamini, P., Hrstka, T., 2009. Benefits of Upfront Mineralogy (QEMSCAN®) in Developing Metallurgical Testwork Programs for Uranium Ores; ALTA2009; International Nickel-Cobalt, Copper and Uranium Conference, conference proceedings

Andersen, J.C.O., Rollinson, G.K., Snook, B., Herrington, R., Fairhurst, R.J., 2009. Use of QEMSCAN® for the characterization of Ni-rich and Ni-poor goethite in laterite ores. Minerals Engineering, 22 (13), pp. 1119-1129.

Anderson, A.J. and Bodnar, R.J., 1993. An adaptation of the spindle stage for geometric analysis of fluid inclusions: American Mineralogist, 78, 657-664.

Aplin, A.C., Mecleod, G., Larter, S. R., Pedersen, K.S, Sorensen, H., Booth, T., 1999. Combined use of Confocal Laser Scanning Microscopy and PVT simulation for estimating the composition and physical properies of petroleum in fluid inclusions. Marine and Petroleum Geology 16, 97-110.

Armitage, P.J., Worden, R.H., Faulkner, D.R., Aplin, A.C., Butcher, A.R. and Iliffe, J., 2010. Diagenetic and sedimentary controls on porosity in lower carboniferous fine-grained lithologies, Krechba field, Algeria: A petrological study of a caprock to a carbon capture site. Marine and Petroleum Geology, Volume 27, Issue 7, August 2010, Pages 1395-1410.

Azbej, T., Severs, M.J., Rusk, B.G. & Bodnar, R.J. 2007, "In situ quantitative analysis of individual H2O-CO2 fluid inclusions by laser Raman spectroscopy", Chemical Geology, vol. 237, no. 3-4, pp. 255-263.

Bakker, R. J. and Diamond L.W., 2006. Estimation of volume fractions of liquid and vapor phases in fluid inclusions, and definition of inclusion shapes; American journal of Mineralogist, volume 91, pages 635-657

Bakker, R. J., and Jansen, J. B. H., 1993. Calculated fluid evolution path versus fluid inclusion data in the COHN system as exemplified by metamorphic rocks from Rogaland, south-west Norway. Journal of Metamorphic Geology, 11: 357–370.

Bakker, R. J., and Elburg M. A., 2006. A magmatic-hydrothermal transition in Arkaroola (northern Flinders Ranges, South Australia): from diopside-titanite pegmatites to hematite-quartz growth. Contributions To Mineralogy And Petrology 152(5): 541-569.

Bakker, R.J. & Jansen J.B.H., 1994. A mechanism for preferential H_2O leakage from fluid inclusions in quartz, based on TEM observations. Contrib Mineral Petrol, 116, 7-20

Bakker, R.J. & Jansen, J.B.H., 1991. Experimental post-entrapment water loss from synthetic CO_2 - H_2O inclusions in natural quartz. Geochim. Cosmochim. Acta, 55, 2215-2230.

Bakker, R.J., 2004. Raman spectra of fluid and crystal mixtures in the systems H_2O, H_2O-NaCl and H_2O-$MgCl_2$ at low temperatures: application to fluid inclusion research. Canadian Mineralogist, v. 42, 1283-1314.

Bakker, R.J. and Diamond L.W., 2006. Estimation of volume fractions of liquid and vapor phases in fluid inclusions, and definition of inclusion shapes. American Mineralogist, 91 (4), pp. 635-657.

Bakker, R.J., 2003, Package FLUIDS 1. Computer programs for the analysis of fluid inclusion data and for modelling bulk fluid properties. Chemical Geology 194 (2003), pp. 3–23.

Bakker, R.J., 2009, Reequilibration of fluid inclusions: Bulk-diffusion. Lithos, vol.112, 277-288.

Barrie, I. J. and Touret, J. L. R., 1999. Fluid inclusion studies of gold-bearing quartz veins from the Yirisen deposit, Sula Mountains greenstone belt, Masumbiri, Sierra Leone. Ore Geology Reviews 14(3-4): 203-225.

Baruchel, J., Jean-Yves Buffière, E. Maire, P. Merle, G. Peix, (2000): X-ray tomography in Material Science, General Principles, Hermes Science Publications, Paris 2000, ISBN 2-7462-0115-1, pp 15-21

Baumgartner M. and Bakker R.J., 2009. Raman spectroscopy of pure H_2O and NaCl–H_2O containing synthetic fluid inclusions in quartz — a study of polarization effects, Miner. Petrol. 95 (2009), pp. 1–15.

Baumgartner, M. & Bakker, R.J. 2010, "Raman spectra of ice and salt hydrates in synthetic fluid inclusions", Chemical Geology, vol. 275, no. 1-2, pp. 58-66.

Beeskow, B., Treloar, P. J. et al., 2006. A reassessment of models for hydrocarbon generation in the Khibiny nepheline syenite complex, Kola Peninsula, Russia. Lithos 91(1-4): 1-18.

Bernard, J.H., and Pouba, Z., 1986. Rudní ložiska a metalogeneze čs. části Českého masívu, Vyd. 1. Praha: Academia, 320 s.

Boiron, M.C., Barakat, A., Cathelineau, M., Banks, D.A., Ďurišová, J., Morávek, P., 2001. Geometry and P-V-T-X conditions of microfissural ore fluid migration: the Mokrsko gold deposit (Bohemia). Chemical Geology 173, 207–225.

Boiron M.C., Cathelineau M., Dubessy J., Bastoul A.M. (1990): Fluids in Hercynian Au veins from the French Variscan Belt. Mineralogical Magazine 54, 231–243.

Boiron, M.C. and Dubessy, J., 1995. Determination of fluid inclusions: microanalytial technigues. In: de Vivo, B., and Frezzotti, M. L. (eds.): Fluid inclusions in minerals: Methods and applications: Blacksburg, Virginia Polytechnic Institute and State University, str. 45-71

Boiron, M.-C., Cathelineau M., Banks D.A., Forucade S., Vallance J., 2003. Mixing of metamorphic and surficial fluids during the uplift of the Hercynian upper crust: consequences for gold deposition. Chemical Geology, 194, 119-141.

Boiron, M.C., Essaraj, S., Sellier, E., Cathelineau, M., Lespinasse, M., Poty, B., 1992. Identification of fluid inclusions in relation to their host microstructural domains in quartz by cathodoluminescence. Geochim. Cosmochim. Acta 56: 175-185.

Boiron, M.C., Moissette, A., Cathelineau, M., Banks, B., Monnin, C. and Dubessy J., 1999. Detailed determination of paleofluid chemistry: an integrated study of sulphate-volatile rich brines and aquo-carbonic fluids in quartz veins from Ouro Fino, Chem. Geol. 154 , pp. 179–192.

Borisenko, A.S., 1977. Study of salt composition of fluid inclusions in minerals using cryometric technigue. Geol.Geofiz. 8, 16-27.

Botha, PWSK, Butcher, AR, Horsch, HE, Rickman, D, Wentworth, SJ, Schrader, CM, Stoeser, D, Benedictus, A, Gottlieb, P, and McKay, D., 2008. Ultrafast Phase Mapping of Thin-Sections from An Apollo 16 Drive Tube – a New Visualisation of Lunar Regolith. GSA 2008 Joint Annual Meeting, 5-9 October 2008, Houston, Texas, abstract 345-3.

Bouchot, V., Ledru, P., Lerouge, C., Lescuyer, J.L., Milesi, J.P. 2005. Late Variscan mineralizing systems related to orogenic processes: The French Massif Central, Ore geology reviews. v. 27. p. 169-197

Bray, C.J., Spooner, E.T.C., Thomas, A.V., 1991. Fluid inclusion volatile analysis by heated crushing, on-line gas chromatography; applications to Archean fluids Journal of Geochemical Exploration, 42 (1), pp. 167-193.

Brown, A. and Petersen E.U., 2009. Fast Quantitative Rock Mineralogy with QEMSCAN: The Quiet Revolution in Rock Characterization 2009 Portland GSA Annual Meeting (18-21 October 2009), Paper No. 29-40

Burke, E.A.J., 2001. Raman microspectrometry of fluid inclusions. Lithos, 55 (1-4), pp. 139-158.

Burruss, R.C., 2003. Raman spectroscopy of fluid inclusions. In: I. Samson, A. Anderson and D. Marshall, Editors, Fluid Inclusions: Analysis and Interpretation, Mineralogical Association of Canada (2003), pp. 279–289.

Chen J., Zheng H., Xiao W., Zeng Y., Weng K., 2004, "Raman spectroscopic study of CO_2-NaCl-H_2O mixtures in synthetic fluid inclusions at high temperatures." Geochimica et Cosmochimica Acta 68(6): 1355- 1360.

Coveney, Jr., R.M. and Kelly, W.C., 1971. Dawsonite as a daughter mineral in hydrothermal fluid inclusions. Contrib. Mineral. Petrol. 32, pp. 334–342.

Creelman, R.A. and Ward, C.R., 1996. Scanning Electron Microscope Method for Automated, Quantitative Analysis of Mineral Matter in Coal International Journal of Coal Geology, vol. 30, issue 3, July, pp. 249 – 269

Davis, A.R. and Oliver, B.G., 1972. A vibrational-spectroscopic study of the species present in the CO_2–H_2O system, Journal of Solution Chemistry 1 (4) (1972), pp. 329–339.

De Ronde, C.E.J., Spooner, E.T.C., De Wit, M.J. and Bray, C.J., 1992. Shear zone related, Au quartz vein deposits in the Barberton greenstone belt, South Africa: field and petrographic characteristics, fluid properties, and light stable isotope geochemistry. Economic Geology, 87, 366–402.

De Vivo, B., Frezzotti M.L., 1995. Fluid inclusions in minerals: Methods and applications: Blacksburg, Virginia Polytechnic Institute and State University, 377 str.

Derome, D., Cathelineau, M., Lhomme, T. and Curley, M., 2003. Fluid inclusion evidence of the differential migration of H-2 and O-2 in the McArthur River unconformity-type uranium deposit (Saskatchewan, Canada). Possible role on post-ore modifications of the host rocks. Journal Of Geochemical Exploration 78-9: 525-530.

Diamond, L.W., 2003. Systematics of H_2O inclusions. In Samson I., Anderson A. and Marshall D. (Eds.) "Fluid Inclusions: Analysis and Interpretation". Short Course Volume 32. Mineralogical Association of Canada. pp. 55-79.

Diamond, L.W., Tarantola, A., Stunitz, H., 2010. Modification of fluid inclusions in quartz by deviatoric stress. II: experimentally induced changes in inclusion volume and composition. Contributions to Mineralogy and Petrology 160, 845–864.

Diamond, L.W., 2003a. Introduction to gasbearing, aqueous fluid inclusions. In I. Samson, A. Anderson, & D. Marshall, eds. Fluid Inclusions: Analysis and interpretation. Mineral. Assoc. Can., Short Ser. 32,101-158.

Diamond, L.W., 1994. Salinity of multivolatile fluid inclusions determined from clathrate hydrate stability Geochim. Cosmochim. Acta, 58 (1), pp. 19-41.

Diamond, L.W., 2001. Review of the systematics of CO_2-H_2O fluid inclusions. Lithos, 55 (1-4), pp. 69-99.

Diamond, L.W., 2003b. Glossary: Terms and symbols used in fluid inclusion studies. In: I. Samson, A. Anderson, D. Marshall (Eds.): Fluid inclusions: analysis and interpretation. Short Course Series Volume 32, Mineralogical Association of Canada, Vancouver, pp. 365-374.

Dubessy J., Poty B. and Ramboz C., 1989. Advances in C-O-H-N-S fluid geochemistry based on micro-Raman spectrometric analysis of fluid inclusions. Europian Journal of Mineralogy 1, pp. 517-534.

Dubessy, J. and Poty, B., 1988. Evidence Of Chemical-Equilibrium And Disequilibrium In The C-O-H-N-S System From Microraman Analysis Of Fluid Inclusions. Chemical Geology 70(1-2): 78-78.

Dubessy, J., Audeoud D., Wilkins, R., Kosztolanyi, C., 1982. The use of the Raman microrobe MOLE in the determination of the electrolytes dissolved in the aqueous phase of fluid inclusions. Chem Geol 37:137–150

Dubessy, J., Boiron, M.-C., Moissette, A., Monnion, C. and Sretenskaya, N., 1992. Determination of water, hydrates and pH in fluid inclusions by micro-Raman spectrometry. Eur. J. Mineral. 4, pp. 885–894.

Dubessy, J., Ding, J., Leisen, M. and Robert, P., 2008. Towards pH estimation of paleofluid circulation combining Raman analysis of CO2/HCO3- bearing fluid inclusions and thermodynamic modelling below 523 K. PACROFI, (IX th) USGS, Reston, USA.

Dubessy, J., Geisler, D., Kosztolanyi, C. and Vernet, M., 1983. The determination of sulphate in fluid inclusions using the MOLE Raman microprobe. Application to a Keuper halite and geochemical consequences. Geochim. Cosmochim. Acta 47, pp. 1–10.

Dubessy, J., L'Homme T., Boiron M.C. and Rull F., 2002. Determination of chlorinity in aqueous fluids using Raman spectroscopy of the stretching band of water at room temperature: application to fluid inclusions, Applied Spectroscopy, 56 pp. 99–106.

Dubessy, J., Pagel, M., Beny, J.-M., Christensen, H., Hickel, B., Kosztolanyi, C., Poty B., 1988. Radiolysis evidenced by H2-O2 and H2-bearing fluid inclusions in three uranium deposits. Geochim. Cosmochim. Acta, 52 (5), pp. 1155-1167.

Dubessy J., Buschaert S., Lamb W., Pironon J. and Thiery R., 2001. Methane-bearing aqueous fluid inclusions: Raman analysis, thermodynamic modelling and application to petroleum basins. Chem. Geol. 173, 193–205.

Ďurišová, J., Strnad, L., Pertold, Z., Pudilova, M., Boiron, M.C., 1995. Gold bearing quartz veins in a regional shear zone: Kasperske Hory gold deposit_Bohemian Massif.. In: Pasava, J., Krıbek, B., Zak, K., Eds.., Proc. of the 3rd Biennial SGA Meeting. A.A. Balkema, pp. 109–112.

Dyni, J.R., 1996. Sodium carbonate resources of the Green River Formation. U.S. Geological Survey Open-File report, 96-729.

Frantz, J. D., 1998. Raman spectra of potassium carbonate and bicarbonate aqueous fluids at elevated temperatures and pressures: comparison with theoretical simulations. Chemical Geology 152(3-4): pp. 211–225.

Fredrich, J. T., 1999. 3D imaging of porous media using laser scanning confocal microscopy with application to microscale transport processes (in Imaging, analysing and modelling pore structure in geomaterials); Physics and Chemistry of the Earth. Part A: Solid Earth and Geodesy (1999), 24(7):551-561

Frei, D., S. Bernstein, R. McLimans & C. Knudsen, 2007. Application of CCSEM to heavy mineral deposits: Source of high-Ti ilmenite sand deposits of South Kerala beaches, SW India, Journal of Geochemical Exploration, Volume 96, Issue 1, January 2008, Pages 25-42.

Goldfarb, R.J., Baker, T., Dube, B., Groves, D.I., Hart, C.J., Gosselin, P., 2005. Distribution, character and genesis of gold deposits in metamorphic terranes. In: Hedenquist, J.W., Thompson, Goldfarb, J.F.H., R.J., Richards, J.P. (Eds.), Economic Geology 100th Anniversary Volume, pp. 407–450.

Goldfarb, R.J., Groves, D.I., Gardoll, S., 2001. Orogenic gold and geologic time: A global synthesis. Ore Geology Reviews, 18 (1-2), pp. 1-75.

Goldstein, R.H., 2003. Petrographic analysis of fluid inclusions. *In:* I. Samson, A. Anderson, D. Marshall (eds.) Fluid inclusions: analysis and interpretation. Short Course Series Vol. 32, Mineral. Assoc. Canada, 9–53.

Goldstein, R.H., Reynolds, T.J., 1994. Systematics of fluid inclusions in diagenetic minerals. Short course 31, Society of Economic Paleontologists and Mineralogists, Tulsa, 199 str.

Gottlieb, P., G. Wilkie, D. Sutherland, E. Ho-Tun, S. Suthers, K. Perera, B. Jenkins, S. Spencer, A. Butcher and Rayner J., 2000. Using Quantitative Electron Microscopy for Process Mineralogy Applications. JOM, April, 24 – 25.

Gottlieb, P. (2007): Personal communication, 01 August.

Götze, J., Plötze, M., Habermann, D., 2001. Origin, spectral characteristics and practical applications of the cathodoluminescence (CL) of quartz: a review. Mineralogy and Petrology 71: 225-250.

Graney, J.R. and Kesler, S.E., 1995. Gas composition of inclusion fluid in ore deposits: Is there a relation to magmas? In: Thompson, J.F.H., ed. Magmas, Fluids and Ore Deposits. Mineralogical Association of Canada Short Course Series 23, 221-245.

Grauch, R.I., Eberl, D.D., Butcher, A.R., and Botha, P.W.S.K., 2008. Quantitative Mineralogy of Fine-grained Sedimentary Rocks: A Preliminary Look at QEMSCAN Microscopy and Microanalysis 2008, 3rd-7th August 2008, Albuquerque, New Mexico, USA

Grimmer, J. O. W., Pironon, J., Teinturier, S., and Mutterer, J., 2003. Recognition and differentiation of gas condensates and other oil types using microthermometry of petroleum inclusions (in Proceedings of Geofluids IV); Journal of Geochemical Exploration, 78-79 (2003): 367-371

Groves, D.I., Goldfarb R.J., Gebre-Mariam M., Hagemann S.G., Robert F., 1998. Orogenic gold deposits: a proposed classification in the context of their crustal distribution and relationship to other gold deposit types, Ore Geology Reviews, 13 (1-5), pp. 7-27.

Groves, D.I., and Foster, R.P., 1991. Archaean lode gold deposits: in Foster, R.P., ed., Gold Metallogeny and Exploration, Blackie, London, p. 63-103.

Gu, M., 1996. Principles of Three-Dimensional Imaging in Confocal Microscopes By Min Gu Published 1996, World , 337 pages, ISBN 9810225504

Gunther, D., 2001. Quantitative fluid inclusion analysis using a 193 nm excimer laser-ablation system coupled to ICP-MS. In: Sylvester, P. (Ed.): Laser-ablation-ICPMS in the earth sciences principles and applications: vol. 29, Min. Assoc. Canada. str. 47-63

Gunther, D. and Heinrich, C. A. 1999. Enhanced sensitivity in laser ablation-ICP mass spectrometry using helium-argon mixtures as aerosol carrier - Plenary lecture. Journal of Analytical Atomic Spectrometry 14: 1363-1368

Gunther, D., Audetat, A., Frischknecht, R., and Heinrich, C. A. 1998. Quantitative analysis of major, minor and trace elements in fluid inclusions using laser ablation inductively coupled plasma mass spectrometry. Journal of Analytical Atomic Spectrometry 13: 263-270

Gy, P. and Marin, L., 1978. Unbiased sampling from a falling stream of particulate material International Journal of Mineral Processing, Volume 5, Issue 3, December 1978, Pages 297-315.

Gy, P.M., 1979. Sampling of particulate materials: Theory and practice, Elsevier Scientific Publishing Co., Amsterdam.

Haberlah, D., Strong, C., Pirrie, D., Rollinson, G.K., Gottlieb, P., Botha, Pieter P.W.S.K. & Butcher, A.R., 2011. Automated petrography applications in Quaternary Science. Quaternary Australasia. 28(2). 3-12.

Haberlah, D., Williams, M.A.J., Halverson, G., McTainsh, G.H., Hill, S.M., Hrstka, T., Jaime, P., Butcher, A.R. & Glasby, P. 2010, "Loess and floods: High-resolution multi-proxy data of Last Glacial Maximum (LGM) slackwater deposition in the Flinders Ranges, semi-arid South Australia", Quaternary Science Reviews, vol. 29, no. 19-20, pp. 2673-2693.

Habermann, D., 2002. Quantitative cathodoluminescence (CL) spectroscopy of minerals: possibilities and limitations. Mineral. Petrol. 76: 247-259.

Hagemann, S.G. and Cassidy, K.F., 2000. Archean orogenic lode gold deposits.In: Hagemann SG, Brown PE (eds) Gold in 2000, Reviews in economic geology, The Society of Economic Geologists, vol. 13, pp 9–68.

Hall, D.L. and Sterner, S.M., 1995. Experimental diffusion of hydrogen into synthetic fluid inclusions in quartz. J. Meta. Geol. 13, 345-355.

Halter, W. E., Pettke, T., Heinrich, Ch. A., Rutishauser, B. R. (2002): Major to trace element analysis of melt inclusions by laser-ablation ICP-MS: methods of quantification. Chemical Geology 183: 63-86

Hanley, J.J., Pettke, T., Mungall, J.E. & Spooner, E.T.C. 2005, "The solubility of platinum and gold in NaCl brines at 1.5 kbar, 600 to 800°C: A laser ablation ICP-MS pilot study of synthetic fluid inclusions", Geochimica et Cosmochimica Acta, vol. 69, no. 10, pp. 2593-2611.

Haynes, H. W., 2003. Thermodynamic solution model of trona brines. AIChE Journal, 49, 1883-1894.

Heinrich, C.A., Pettke, T., Halter, W. E., Aigner-Torres, M., Audetat, A. Gunther, D., Hattendorf, B., D. Bleiner, Guillong, M. and Horn, I., 2003. Quantitative multi-element analysis of minerals, fluid and melt inclusions by laser-ablation inductively-coupled-plasma mass-spectrometry. Geochimica et Cosmochimica Acta. vol. 67, pp. 3473-3496

Hoal, K.O., Appleby, S.K., Stammer, J.G. and Palmer, C., 2009. SEM-based quantitative mineralogical analysis of peridotite, kimberlite and concentrate. Lithos 1125, 41-46.

Holness, M.B. & Watt, G.R., 2001. Quartz recrystallization and fluid flow during contact metamorphism: a cathodoluminescence study. Geofluids 1: 215-228.

Holub, F. V., Cocherie, A., Rossi, P., 1997b. Radiometric dating of granitic rocks from the Central Bohemian Plutonic Complex (Czech Republic): constraints on the chronology of thermal and tectonic events along the Moldanubian-Barrandian boundary. Comptes Rendus de L Academie Des Sciences, Serie Ii Fascicule A-Sciences De La Terre Et Des Planetes 325, 19-26.

Holub, F., Machart, J., Manová, M., 1997a. The Central Bohemian plutonic Complex Geology, chemical composition and genetic interpretation. Sborník geologických Věd, Ložisková geologie a Mineralogie 31, Prague, 27-50.

Hoshino, K., Nagatomi, A.,Watanabe, M., Okudaira, T., Beppu, Y., 2006. Nahcolite in fluid inclusions from the Ryoke metamorphic rocks and its implication for fluid genesis. Journal Of Mineralogical And Petrological Sciences 101(5): 254-259.

Howells, D.A., 1974. The time for a significant change of pore pressure. Engineering Geology, 8 (1-2), pp. 135-138.

Hrstka, T., 2004. MSc. dissertation, Institute of Geochemistry, Mineralogy and Mineral Resources, Charles University in Prague, Faculty of Science, Prague, Použití laserové ablace a hmotnostní spektrometrie (LA-ICP-MS) ke studiu chemizmu paleofluid. 81pp, (in Czech)

Hrstka, T., Dubessy, J., Zachariáš, J., 2011. Bicarbonate-rich fluid inclusions and hydrogen diffusion in quartz from the Libčice orogenic gold deposit, Bohemian Massif. Chemical Geology, Volume 281, Issues 3-4, 24 February 2011, Pages 317-332

Hrstka, T., Dubessy, J., Zachariáš, J., 2011. Potential Concentration Measurements of HCO_3^- and pH Estimates in Natural Fluid Inclusions by Raman Spectroscopy: A Case Study from Libčice Gold Deposit, European Current Research on Fluid Inclusions (ECROFI-XXI), Montanuniversität Leoben, Austria, 9–11 August, 2011. Abstract Volume, p. 104

Hrstka, T., 2008. Preliminary Results on the Reproducibility of Sample Preparation and QEMSCAN® Measurements for Heavy Mineral Sands Samples; ICAM2008; Ninth International Congress for Applied Mineralogy, congress proceedings, ISBN: 9781920806866

Hrstka, T., 2010. Potential Concentration Measurements of HCO_3^- and pH Estimates in Natural Fluid Inclusions by Raman Spectroscopy: A Case Study from Libčice Gold Deposit. In preparation, unpublished data.

Hrstka, T., 2006a. X-Ray Nanotomography in Fluid Inclusions Study - poster; 1st.Central European Mineralogical Conference, Vysna Boca 2006, Slovak Republic

Hrstka, T., 2006b. Confocal Microscopy in Geoscience; MDSG 2006 (The 29th Annual Winter Conference of the Mineral Deposits Studies Group, London).

Hrstka, T., Zachariáš, J., Mihaljevic, M., Herrington, R., Willkinson, J., 2006. Paleofluid chemistry and mineralogical variations of orogenic gold deposits in the Bohemian Massif; Fermor 2006 (Minerals, Magmas and Megastructures) London Natural History Museum

Huff, T. A. and Nabelek, P.I., 2007. Production of carbonic fluids during metamorphism of graphitic pelites in a collisional orogen – An assessment from fluid inclusions. Geochim. Cosmochim. Acta., 71(20), pp. 4997-5015.

Huizenga, J. M., 2001. Thermodynamic modelling of C-O-H fluids. Lithos 55(1-4): 101-114.

Huizenga, J.M., 2005. COH, an Excel spreadsheet for composition calculations in the C–O–H fluid system. Computers & Geosciences 31, pp. 797–800.

Huraiova, M., Hurai, V., Slobodnik, M., 2002. Základy štúdia fluidných inklúzií v mineráloch (Fundamentals of investigation of fluid inclusions in minerals). Vyd. 1. Brno : MU Brno, UK Bratislava, 2002. 120 pp. NMU, 1. ISBN 80-210-2889-0. (in Czech)

ICDD. JCPDS PDF-2 database. Newton Square, PA USA. ICDD; 2002

Jia, Y., Li, X. and Kerrich, R., 2000. A fluid inclusion study of Au-bearing quartz vein systems in the Central and North Deborah deposits of the Bendigo gold field, central Victoria, Australia: Economic Geology, v. 95, p. 467–496.

Kats, A., Haven, Y., and Stevels J. M., 1962. Hydroxyl groups in alpha quartz. Phys. Chem. Glasses 3, 69-75.

Kerrich, R., and Cassidy, K.F., 1994. Temporal relationships of lode gold mineralization to accretion, magmatism, metamorphism and deformation - Archean to present: A review. Ore Geology Reviews, 9 (4), pp. 263-310.

Klein, E L., Fuzikawa K., 2010. Origin of the CO2-only fluid inclusions in the Palaeoproterozoic Carara vein-quartz gold deposit, Ipitinga Auriferous District, SE-Guiana Shield, Brazil: Implications for orogenic gold mineralisation. Ore Geology Reviews, Volume 37, Issue 1, Pages 31-40.

Klein, E. L., Fuzikawa K., and Koppe J. C., 2000, Fluid inclusion studies on Caxias and Areal gold mineralizations, São Luís Craton, northern Brazil. Journal of Geochemical Exploration, 71, p. 51–72.

Klemd, R., Hunken, U., Olesch, M.O., 2002. Metamorphism of the country rocks hosting gold-sulfide-bearing quartz veins in the Paleoproterozoic southern Kibi-Winneba belt (SE-Ghana). Journal of African Earth Sciences, 35 (2), pp. 199-211.

Kogan, V.B., Ogorodnikov, S.K. and Kafarov, V.V., 1969 Handbook of Solubility, 2, Izd. Akad. Nauka, Leningrad, Russia, 1170 pp. (in Russian).

Krishnamurti, D., 1958. The Raman spectrum of quartz and its interpretation, Indian Academy of Sciences, Proceedings of the Indian Academy of Sciences A, 47, 276, 1958

Kruger, Y. and Diamond L. W., 2001. Unexpected behaviour of fluid inclusions synthesized from silver oxalate and an aqueous NaCl solution. Chemical Geology 173(1-3): 159.

Kruse, R. and Franck, E.U., 1982. Raman spectra of hydrothermal solutions of CO_2 and HCO_3 at high temperatures and pressures. Ber. Bunsenges Phys. Chem. 86, pp. 1036–1038.

Kurosawa, M., Ishii, S. & Sasa, K., 2008. "Quantitative PIXE analyses of single fluid inclusions in quartz crystals with a 1.92-MeV tandetron", Nuclear Instruments and Methods in Physics

Research, Section B: Beam Interactions with Materials and Atoms, vol. 266, no. 16, pp. 3633-3642.

Kurosawa, M., Shimano, S., Ishii, S., Shima, K. & Kato, T. 2003a. "Quantitative trace element analysis of single fluid inclusions by proton-induced X-ray emission (PIXE): Application to fluid inclusions in hydrothermal quartz", Geochimica et Cosmochimica Acta, vol. 67, no. 22, pp. 4337-4352.

Kurosawa, M., Shimano, S., Ishii, S., Shima, K., Nakajima, T. & Kato, T., 2003b, "Quantitative PIXE analysis of single fluid inclusions in quartz vein: Chemical composition of hydrothermal fluids related to granite", Nuclear Instruments and Methods in Physics Research, Section B: Beam Interactions with Materials and Atoms, vol. 210, pp. 464-467.

Lambrecht, G., Diamond, L.W. & Pettke, T. 2008, "Modification of gas speciation in quartz-hosted fluid inclusions by stray laser radiation during LA-ICPMS analysis", American Mineralogist, vol. 93, no. 7, pp. 1187-1190.

Lang, J.R., and Baker, T., 2001. Intrusion-related gold systems: the present level of understandin, Mineralium Deposita, 36 (6). pp. 477-489. ISSN 1432-1866

Latti, A.D., 1997. The application of QEM*SEM to the Quelimane Heavy Mineral Deposit, Mozambique. Heavy Minerals, Johannesburg, South African Institute of Mining and Metallurgy, 1997.pp. 197-202.

Latti, A.D., 1997. The application of QEM*SEM to the Quelimane Heavy Mineral Deposit, Mozambique. Heavy Minerals, Johannesburg, South African Institute of Mining and Metallurgy, 1997.pp. 197-202.

Litochleb, J. - Šrein, V., 1994. Minerály bismutu a telluru z ložisek a výskytů zlata v České republice. - Bull. min.-petr. odd. NM v Praze, 2, 89-105. Praha. (in Czech).

Liu, Xi and Fleet, M. E., 2009. Phase relations of nahcolite and trona at high P-T conditions. Journal of Mineralogical and Petrological Sciences, Vol. 104, 25-36.

Longrich, H. P., Jackson, S. E., Gunther, D., 1996. Laser Ablation Inductively Coupled Plasma Mass Spectrometric Transient Signal Data Acquisition and Analyte Concentration Calculation. Journal of Analytical Atomic Spectrometry, vol.11, str. 899-904

Loucks, R.R., 2000. Precise geothermometry on fluid inclusion populations that trapped mixtures of immiscible fluids. Am. J. Sci. 300, 23-59.

Loucks, R.R. and Mavrogenes, J.A., 1999. Gold solubility in supercritical hydrothermal brines measured in synthetic fluid inclusions; Science, v.284, p.2159-2163.

Lui, Y., Gupta, R., Sharma, A., Wall, T., Butcher, A.R., Miller, G., Gottlieb, P. & French, D., 2005. Mineral matter-organic matter association characterisation by QEMSCAN and applications in coal utilization Fuel, Volume 84, Issue 10, 1259-1267

Lyman, G. J., 1998. The influence of segregation of particulates on sampling variance — the question of distributional heterogeneity; International Journal of Mineral Processing, Volume 55, Issue 2, December 1998, Pages 95-112.

Marshall, D.J., 1988. Cathodoluminescence of geological materials. Allen & Unwin Inc., Winchester/Mass., 146p.

Martinez, I., Sanchez-Valle, C., Daniel, I., and Reynard, B., 2004. High-pressure and high-temperature Raman spectroscopy of carbonate ions in aqueous solution, Chemical Geology 207 (1–2), pp. 47–58.

Mavrogenes, J. A. and Bodnar, R. J. 1994. Hydrogen Movement Into And Out Of Fluid Inclusions In Quartz - Experimental-Evidence And Geologic Implications. Geochim. Cosmochim. Acta 58(1): 141-148.

McCollom, T.M., and Bach, W., 2009. Thermodynamic constraints on hydrogen generation during serpentinization of ultramafic rocks, Geochim. Cosmochim. Acta 73 (3), pp. 856-875.

Mernagh, T.P. & Witt, W.K., 1994. Early, methane-rich fluids and their role in Archaean gold mineralization at the Sand King and Missouri deposits, Eastern Goldfields Province, Western Australia. AGSO J. Aust. Geol. Geophys. 15, 297-312.

Mernagh, T.P. and Wilde, A.R., 1989. The use of the laser Raman microprobe for the determination of salinity in fluid inclusions. Geochim. Cosmochim. Acta 53, pp. 765–771.

Mernagh, T.P. and Witt, W.K., 1994. Early, methane-rich fluids and their role in Archaean gold mineralisation at the Sand King and Missouri deposits, Eastern Goldfields Province, Western Australia. AGSO Journal of Australian Geology and Geophysics 15, pp. 297–312

Mernagh, T.P., Heinrich, C.A. & Mikucki, E.J. 2004. Temperature gradients recorded by fluid inclusions and hydrothermal alteration at the Mount Charlotte gold deposit, Kalgoorlie, Australia. Can. Mineral. 42, 1383–1403.

Moissette, A., Shepherd, T. J. and Chenery, S. R., 1996. Calibration strategies for the elemental analysis of individual aqueous fluid inclusions by laser ablation inductively coupled plasma mass spectrometry. Journal of Analytical Atomic Spectrometry 11: 177-185

Morávek, P., 1985. Evaluation of the gold potential in the BohemianMassif, Czechoslovakia. MS Geofond Praha, 172 pp. in Czech.

Morávek, P., Janatka, J., Pertoldová, J., Straka, E., Ďurišová, J., Pudilová, M., (1989): Mokrsko gold deposit - the largest gold deposit in the Bohemian Massif, Czechoslovakia: Economic Geology Monograph, v. 6, 252–259.

Morávek P., Pouba Z., 1990. L'or dans la metallogenie du massif de Boheme: Mineralium Deposita 25, S90–S98.

Morávek, P., 1971. Ore-deposits structure and mineralization of the Jilove gold-mining district (in Czech with extensive English summary). Journal of Geological Sciences: Economic Geology, Mineralogy, Prague, 13, 1 –170.

Morávek, P., Janatka, J., Pertoldova, J., Straka, E., Ďurišová, J. and Pudilova, M., 1989. Mokrsko gold deposit – the largest gold deposit in the Bohemian Massif, Czechoslovak ia. Economic Geology Monograph, 6, 252 –259.

Morgan, G. B., Chou, I. M. et al., 1992. Speciation In Experimental C-O-H Fluids Produced By The Thermal-Dissociation Of Oxalic-Acid Dihydrate. Geochim. Cosmochim. Acta 56(1): 281-294.

Morgan, VI, G.B., Chou, I.-M., Pasteris, J.D. and Olsen, S.N., 1993. Re-equilibration of CO2 fluid inclusions at controlled hydrogen fugacities. Journal of Metamorphic Geology 11, pp. 155–164

Müller, A., Armstrong, R., Herrington, R., Seltmann, R., 2003. Characterisation of quartz textures in porphyry copper ore deposits by scanning electron microscope-cathodoluminescence (SEM-CL). Mongolian Geoscientist, 21, 32–35.

Nechayeva, O. L., 1968. Hydrogen in Gases Dissolved in Water of the West Siberian Plain," Doklady. Akad. Navk, Vol. 179, No. 4, pp. 961-962.

Němec, I., 2009 Personal communication, May 2009

Neumayer, P. and S. G., Hagemann, 2002. Hydrothermal fluid evolution within the Cadillac tectonic zone, Abitibi greenstone belt, Canada: Relationship to auriferous fluids in adjacent second- and third-order shear zones. Economic Geology And The Bulletin of The Society of Economic Geologists 97(6): 1203-1225.

Oliver, B.G. and Davis, A.R., 1973. Vibrational spectroscopic studies of aqueous alkali metal bicarbonate and carbonate solutions. Can. J. Chem. 51, pp. 698–702

Pagel, M., Barbin, V., Blanc, P., Ohnenstetter, D., (eds.) 2000. Cathodoluminescence in geosciences. Springer Verlag, Berlin Heidelberg New York, 514 p.

Papineau, D., Mojzsis, S.J., Karhu, J.A., Marty, B., 2005. Nitrogen isotopic composition of ammoniated phyllosilicates: Case studies from Precambrian metamorphosed sedimentary rocks, Chemical Geology, 216 (1-2), pp. 37-58.

Pawley, J.B., (editor) 2006. Handbook of Biological Confocal Microscopy (3rd ed.). Berlin: Springer. ISBN 038725921X.

Peretti, A., Dubessy, J., Mullis, J., Frost, R., Trommsdorff, V., 1992. Highly reducing conditions during alpine metamorphism of the Maleno peridotite (Sondrio, northern italy) indicated by mineral paragenesis and H2 in fluid inclusions. Contrib. Mineral. Petrol., 112, 329-340.

Perring, C.S., Barnes, S.J., Verrall, M., Hill R.E.T., 2004. Using automated digital image analysis to provide quantitative petrographic data on olivine-phyric basalts Computers and Geosciences, 30 (2), pp. 183-195.

Petford, N. & Miller, J.A. & Rankin, A.H., 1994 Preliminary confocal scanning laser microscopy of fluid inclusions in quartz. Journal of Microscopy 178, 37-41.

Petford, N. & Miller, J.A., 1993. Three-dimensional imaging of fission tracks using confocal scanning laser microscopy. J.Microsc. 170, 201-212.

Petford, N., and Miller J. A., 1992. Three-dimensional imaging of fission tracks using confocal scanning laser microscopy; American Mineralogist, (Jun 1992); 77: 529 - 533.

Petford, N., Davidson G., and Miller, J. A., 2001. Investigation of the petrophysical properties of a porous sandstone sample using confocal scanning laser microscopy; Petroleum Geoscience (May 2001), 7(2):99-105

Pettke, T., Diamond, L.W. and Kramers, J.D., 2000. Mesothermal gold lodes in the north-western Alps: A review of genetic constraints from radiogenic isotopes. Eur. J. Mineral. 12, (1) 213-230.

Phillips, G.N., Powell R., 2009. Formation of gold deposits: Review and evaluation of the continuum model , Earth-Science Reviews, 94 (1-4), pp. 1-21.

Pironon, J., Canals, M., Dubessy, J., Walgenwitz, F., and Corinne Laplace-Builhe. 1998. Volumetric reconstruction of individual oil inclusions by confocal scanning laser microscopy (in ECROFI XIV (European Current Research on Fluid Inclusions) symposium) European Journal of Mineralogy, 10(6):1143-1150

Pironon, J., Thiery, R., Teinturier, S., Walgenwitz, F., 2000. Water in petroleum inclusions: evidence from Raman and FTIR measurements, PVT consequences. Journal of Geochemical Exploration, 69-70, 663-668.

Pirrie, D., Butcher, A.R. & Power, M.R., 2000. Automated SEM-based quantitative mineral analysis; applications in sediment provenance studies in terrane analysis

Pirrie, D. & Rollinson, G.K., 2011. Unlocking the applications of automated mineral analysis. Geology Today. 27(6). 235-244.

Pitard, F.F., 1993. Pierre Gy`s sampling theory and sampling practice-heterogenity, Sampling correctness, and statistical process control, 2nd edition.

Polito, P.A., Bone, Y., Clarke, J.D.A. and Mernagh T.P., 2001. Compositional zoning of fluid inclusions in the Archaean Junction gold deposit, Western Australia: a process of fluid-wall–rock interaction?, Australian Journal of Earth Sciences 48, pp. 833–855

Potter, J., Rankin, A.H., Treloar, P.J., 2004. Abiogenic Fischer–Tropsch synthesis of hydrocarbons in alkaline igneous rocks; fluid inclusion, textural and isotopic evidence from the Lovozero complex, N.W. Russia. Lithos 75, 311–330.

Reitsema, R.H., 1980. Dolomite and nahcolite formation in organic rich sediments: isotopically heavy carbonates. Geochim. Cosmochim. Acta, 44 (12), pp. 2045-2049.

Ridley, J. and Hagemann, S. G., 1999. Interpretation of post-entrapment fluid-inclusion re-equilibration at the Three Mile Hill, Marvel Loch and Griffins Find high-temperature lode-gold deposits, Yilgarn Craton, Western Australia. Chemical Geology 154(1-4): 257-278.

Ridley, J.R. and Diamond, L.W., 2000. Fluid chemistry of lode-gold deposits, and implications for genetic models. In: S.G. Hagemann and P. Brown (Editors), Gold in 2000. Reviews in Economic Geology. Society of Economic Geologists, Inc., pp. 141-162.

Robert, F, Boullier, A-M, Firdaous, K., 1995. Gold-quartz veins in metamorphic terranes and their bearing on the role of fluids in faulting. J Geophys Res 100:12861–12879

Roedder, E., 1984. Fluid inclusions. Reviews in Mineralogy, vol. 12, Mineralogical Society of America, Washington, pp. 646

Rosasco, G. J. and Roedder E., 1979. "Application of a new Raman microprobe spectrometer to nondestructive analysis of sulfate and other ions in individual phases in fluid inclusions in minerals." Geochimica et Cosmochimica Acta 43(12): 1907.

Ross, Daniel J.K., and Bustin R. Marc, 2006, Sediment geochemistry of the Lower Jurassic Gordondale Member, northeastern British Columbia: Bulletin of Canadian Petroleum Geology, 54(4), 337-365

Rusk, B. and Reed, M. 2002. Scanning electron microscopecathodoluminescence analysis of quartz reveals complex growth histories in veins from the Butte porphyry copper deposit, Montana. Geology, 30, 727–730.

Samson, I., Anderson, A., Marshall, D., (eds). 2003. Fluid Inclusions: Analysis and Interpretation Mineralogical Association of Canada, Short Course Series, vol. 32, 374 pp. US45 (outside Canada), Can45(outsideCanada),Can 45 (in Canada). ISBN 0–921294–32–8

Sejkora, J., Litochleb J., Plášil, J., Bureš, B., 2009. Tsumoite and associated tellurides from the Au deposit Libčice near Nový Knín, Czech Republic: mineralogy and genetic significance. Journal of Geosciences, 54, 1, 73 – 82

Shepherd, T. J. and Chenery, S. R., 1995. Laser ablation ICP-MS elemental analysis of individual fluid inclusions: An evaluation study. Geochimica et Cosmochimica Acta 59: 3997-4007

Shepherd, T.J., Rankin, A.H., Alderton, D.H.M., 1985. A Practical Guide to Fluid Inclusion Studies. Blackie & Son, Glasgow. Distributed in the USA by Chapman and Hall (Glasgow, New York), English, 239 pages

Sheppard, C. J. R., Hotton, D. M., Shotton, D., 1997. Confocal Laser Scanning Microscopy Paperback: 106 pages Publisher: BIOS Scientific Publishers (September 1997) language: English ISBN-10: 0387915141 ISBN-13: 978-0387915142

Sibson, R.H., Robert, F., Poulsen, K.H., 1988. High angle reverse faults, fluid-pressure cycling, and mesothermal gold quartz deposits. Geology 16, 551–555.

Sillitoe, R.H., Thompson, J.F.H., 1998. Intrusion-related vein gold deposits: Types, tectono-magmatic settings and difficulties of distinction from orogenic gold deposits. Resour. Geol. 48, 237–250.

Skyscan, 1977, Skyscan 1072 Desktop Microscope-microtomograph: instruction manual. Skyscan, Aartselaar, 43 pp.

SkyScan, 1072, X-ray Microscope Instruction Manual, 60 p. SkyScan., 2005. Aartselaar, Belgium, viewed 7 June, 2005, <http://www. skyscan.be>.

Sleep, N.H., Meibom, A., Fridriksson, Th., Coleman, R.G., Bird, D.K., 2004. H2-rich fluids from serpentinization: Geochemical and biotic implications. Proceedings of the National Academy of Sciences of the United States of America, 101 (35), pp. 12818-12823.

Sliwinski, J., Le Strat, M., and Dublonko, M., 2009. A new quantitative method for analysis of drill cuttings and core for geologic, diagenetic, and reservoir evaluation 2009 AAPG Annual Convention and Exhibition, Denver, Colorado, June 7-10, 2009, p.197

Sliwinski, J., Harrington, J., Power, M., Hughes, P., and Yeung, B. 2010. A High Definition Mineralogical Examination of Potential Gas Shales AAPG 2010, New Orleans (11-14 April 2010), Abstract Volume, p. 239

Smith, P.L., 2001. A primer of sampling solids, liquids, and gases: based on seven sampling errors of Pierre Gy, Asa-Siam Series on Statistics and Applied Probability, Soc for industrial & Applied Maths, 96.

Spring, K.R. and Davidson, M.W., Introduction to Fluorescence Microscopy, http://www.microscopyu.com/articles/fluorescence/fluorescenceintro.html, (23.5.2005)

Šrein, V., Pivec, E., Langrová, A., 1995. Petrology and mineralogy of the gold-bearing deposit Libčice near Nový Knín. Bull mineral-petrolog Odd Nár Muz (Praha) 3: 188-195 (in Czech)

Sterner, S.M., Hall, D.L., Keppler, H., 1995. Compositional re-equilibration of fluid inclusions in quartz. Mineralogy and Petrology 119, 1–15.

Stoller, P., Kruger, Y., Ricka, J., Frenz, M., 2007. Femtosecond lasers in fluid inclusion analysis: Three-dimensional imaging and determination of inclusion volume in quartz using second harmonic generation microscopy. Earth and Planetary Science Letters, 253 (3-4), pp. 359-368.

Stumm, W. and Morgan, J.J., 1996. Aquatic Chemistry: Chemical Equilibria and Rates in Natural Waters. , Wiley-Interscience publication, New York.

Suchý, V., 1992. Lecice black shale (Barrandian Upper Proterozoic, Central Czechoslovakia): Euxenic facies of starved preflysch basin. In: Kribek B. (ed.): Metallogeny and anoxic environments, Proceedings of the IVth Czech and Slovak working group of the IGCP, Project 254., pp.11-12.

Suchý, V., Sýkorová, I., Melka, K., Filip, J., Machovič, V., 2007. Illite „crystallinite" coalification of organic matter and microstructural development associated with lowest-grade metamorphism of Neoproterozoic sediments in the Teplá-Barrandian unit, Czech Republic. - Clay Minerals, 42, 415-438.

Tarantola, A., Diamond, L.W., Stunitz, H., 2010. Modification of fluid inclusions in quartz by deviatoric stress I: experimentally induced changes in inclusion shapes and microstructures. Contributions to Mineralogy and Petrology 160, 825–843.

Thiery, R., Pironon, J.,Walgenwitz, F., Montel, F., 2000. PIT: a new modeling tool for the characterization of hydrocarbon fluid inclusions from volumetric and microthermometric measurements. Journal of Geochemical Exploration 69-70, 701-704.

Thompson J.F.H., Sillitoe R.H., Baker T., Lang J.R., Mortensen J.K., 1999. Intrusion related gold deposits associated with tungsten-tin provinces. Mineralium Deposita 34, 323–334.

Timofeeff, M.N., Lowenstein, T.K. & Blackburn, W.H., 2000. "ESEM-EDS: An improved technique for major element chemical analysis of fluid inclusions", Chemical Geology, vol. 164, no. 3-4, pp. 171-182.

Tissot, B.P. and Welte, D.H., 1987. Petroleum Formation and Occurrence. A New Approach to Oil and Gas Exploration. Springer-Verlag.

Tricart, J.P., Van Geet, M. and Sasov, A., 2000. Using Micro-CT for 3D characterisation of geological materials. Microscopy and analysis, May 2000, 65, pp. 31

Tsunogae, T. and Dubessy, J., 2009. Ethane- and hydrogen-bearing carbonic fluid inclusions in a high-grade metamorphic rock. Journal of Mineralogical and Petrological Sciences, Vol. 104, 324-329

Van Alphen, C., 2006. Automated Mineralogical Analysis of Coal and Ash Products – Challenges and Requirements. Minerals Engineering, Vol 20, No. 5, December, 2003, Brisbane, Australia

Van den Kerkhof, A.M., 1990. Isochoric phase diagrams in the systems CO_2CH4 and CO_2N_2: Application to fluid inclusions. Geochim. Cosmochim. Acta, 54 (3), pp. 621-629.

Van Geet, M., Swennen, R. and Wevers, M., 2000. Quantitative analysis of reservoir rocks by microfocus X-ray computerised tomography. Sed. Geol., 132, pp. 25-36

Vapnik, Ye. and Moroz, I., 2002. Composition and formation conditions of fluid inclusions in emerald from Maria deposit (Mozambique). Mineralogical Magazine, 66, 201–213

Wang, J., Zhang, Y., Yang, Q., Zhou, J., MA, X., 1991. The geological characterization and origin of the Anpeng alkali deposit. Geological Review, 37, 42-50.

Weltje, G.J., 2002. Quantitative analysis of detrital modes: statistically rigorous confidence regions in ternary diagrams and their use in sedimentary petrology. Earth-Sci. Rev. 57, 211 – 253.

Whiticar, M.J., 1999. Carbon and hydrogen isotope systematics of bacterial formation and oxidation of methane. Chem. Geo. 161:291–314

Wilkinson, J.J., 2001, "Fluid inclusions in hydrothermal ore deposits", Lithos, vol. 55, no. 1-4, pp. 229-272.

Wopenka, B. and Pasteris, J.D., 1986. Limitations to quantitative-analysis of fluid inclusions in geological samples by laser Raman microprobe spectroscopy, Applied Spectroscopy 40 (2) (1986), pp. 144–151.

Wopenka, B. and Pasteris, J.D., 1987. Raman intensities and detection limits of geochemically relevant gas mixtures for a laser Raman microprobe. Anal. Chem. 59, pp. 2165–2170.

Wopenka, B. and Pasteris, J. D. 1993. Structural characterization of kerogens to granulite-facies graphite; applicability of Raman microprobe spectroscopy. American Mineralogist 78(5-6), 533-557.

Wu, J., and Zheng, H., 2010. Quantitative measurement of the concentration of sodium carbonate in the system of $Na_2CO_3-H_2O$ by Raman spectroscopy. Chemical Geology, 273, 267-271.

Yao Y., Murphy, P.J. and Robb, L.J., 2001. Fluid characteristics of granitoid-hosted gold deposits in the Birimian Terrane of Ghana: a fluid inclusion microthermometric and Raman spectroscopic study. Economic Geology 96 (2001), pp. 1611–1643.

Zachariáš, J., Hrstka, T., Dubessy, J., 2011. Bicarbonate-rich fluid inclusions and hydrogen diffusion in quartz gangue from the Libčice orogenic gold deposit, Bohemian Massif, European Current Research on Fluid Inclusions (ECROFI-XXI), Montanuniversität Leoben, Austria, 9–11 August, 2011. Abstract Volume, p. 208

Zachariáš, J., Paterová, B., Pudilová, M. 2009a. Mineralogy, fluid inclusion, and stable isotope constraints on the genesis of the Roudný Au-Ag deposit, Bohemian Massif. Economic Geology 104, 53–72.

Zachariáš, J., Pudilová, M., Žák, K., Morávek, P., Litochleb, J., Váňa T., Pertold Z., 1997. P-T conditions, fluid inclusions and O, C, S isotope characteristics of gold-bearing mineralizations within the Central Bohemian Metallogenic Zone. - Acta Univ. Carolinae – Geologica 41, 167–178.

Zachariáš, J., Stein, H., 2001. Re-Os ages of Variscan hydrothermal gold mineralisations, Central Bohemian metallogenetic zone, Czech Republic. *In:* Piestrzyński et al. (eds.): Mineral Deposits at the Beginning of the 21st Century, 851–854, Swets & Zeitlinger Publishers Lisse.

Zachariáš, J., 2002. Interpretation of bidimensional fluid inclusion microthermometric data in terms of pressure and compositional variations in gold-bearing fluids: An example from the Libčice and Kasejovice deposits, Czech Republic, Journal of the Czech Geological Society, volume 47, issue 3-4,123 – 132.

Zachariáš, J., Pertold, Z., Pudilová, M., Žák, K., Pertoldová, J., Stein, M., Markey, R., 2001. Geology and genesis of Variscan porphyry-style gold mineralization, Petráčkova hora deposit, Bohemian Massif, Czech Republic. Miner Depos 36: 517-541.

Zachariáš, J., Pudilová, M., Žák, K., Morávek, P., Litochleb, J., Váňa, T., Pertold, Z., 1997. P-T conditions, fluid inclusions and O, C, S isotope characteristics of gold-bearing mineralizations within the Central Bohemian Metallogenic Zone. Acta Univ Carol, Geol 41: 167-178.

Zaitsev, A.N. and Keller, J., 2006. Mineralogical and chemical transformation of Oldoinyo Lengai natrocarbonatites, Tanzania. Lithos 91, 191-207.

Ziegenbein, D. and Johannes, W., 1980. Graphite in C–H–O fluids; an unsuitable compound to buffer fluid compositions at temperatures to 700 °C. Neues Jahrbuch für Mineralogie, Monatshefte 7, pp. 289–305

Zoheir, B., Akawy, A., and Hassan, I., 2008. Role of fluid mixing and wallrock sulfidation in gold mineralization at the Semna mine area, central Eastern Desert of Egypt: Evidence from

hydrothermal alteration, fluid inclusions and stable isotope data. Ore Geology Reviews, 34 (4), pp. 580-596.

Appendix A : Authors Related Conference Abstracts:

Appendix A.1 Potential Concentration Measurements of HCO_3^- and pH Estimates in Natural Fluid Inclusions by Raman Spectroscopy: A Case Study from Libčice Gold Deposit

Presented at: ECROFI 2011 (European Current Research on Fluid Inclusions (ECROFI-XXI), Montanuniversität Leoben, Austria, 9-11 August, 2011).

Hrstka T., Dubessy J., Zachariáš J. (2011): Potential Concentration Measurements of HCO_3^- and pH Estimates in Natural Fluid Inclusions by Raman Spectroscopy: A Case Study from Libčice Gold Deposit,European Current Research on Fluid Inclusions (ECROFI-XXI), Montanuniversität Leoben, Austria, 9-11 August, 2011. Abstract Volume, p. 104

Potential Concentration Measurements of HCO_3^- and pH Estimates in Natural Fluid Inclusions by Raman Spectroscopy: A Case Study from Libcice Gold Deposit

Hrstka, Tomas.*, Dubessy, Jean** and Zacharias, Jiri***

* Institute of Geology AS CR, v.v.i., Rozvojová 269, CZ-165 00 Prague 6 – Lysolaje, Czech Republic
E-mail: hrstka@gli.cas.cz
** G2R(UMR 7566), Faculté des Sciences, Université Henri Poincaré-Nancy Université, BP-70239, 54506-Vandoeuvre-les Nancy Cedex France, E-mail: Jean.Dubessy@g2r.uhp-nancy.fr
*** Charles University in Prague, Faculty of Science, Institute of Geochemistry, Mineralogy and Mineral Resources, Albertov 6, Praha 2, CZ-128 43, E-mail: zachar@natur.cuni.cz

Unusual fluid inclusion composition has been reported earlier at the Libcice orogenic gold deposit. (Zacharias, 2002 and Hrstka et al., 2011). Bicarbonate (HCO_3^-) rich H_2O-CO_2 (CH_4 N_2 H_2S + C_2H_6) and H_2O fluids were recorded by this earlier study. Based on the high variability of FIA and expected variable HCO_3^- content these fluids has been identified as ideal candidate for HCO_3^- qunatification in natural fluid inclusions. Quantitative calculations of the concentration of Raman active ions such as: HCO_3^-; CO_3^{2-}; SO_4; PO_4^{3-}; HS^-, can lead us to important information about pH, f_{O2}, f_S fugacity as well as other parameters of the paleofluid (Dubessy et al., 1989, 2008). While the concentration of SO_4; HS^- polyatomic species in natural paleofluids was measured and even quantified for some species (Dubessy et al., 2002), not many data have ever been reported for the HCO_3^-.

This paper reports on high temperature Raman measurements made in order to confirm the abnormally high concentrations of bicarbonate in Libcice paleofluids and also on the first attempts to validate the individual Raman peaks for future quantitative analysis of HCO_3^- in aqueous-carbonic paleofluids. The pH calculation in quartz hosted natural fluid inclusions based on the pH controlled equilibria of (HCO_3^-)/(CO_3^{2-}) (with main Raman peaks at about 1017 cm^{-1} and 1064 cm^{-1}, respectively) were also evaluated. The high concentration of HCO_3^- in the fluids was confirmed by the presence of a peak at 1014cm^{-1} and at 1360cm^{-1} even at the temperatures above total homogenization (Th tot). Proportions of the IR peak integrated areas were measured in order to

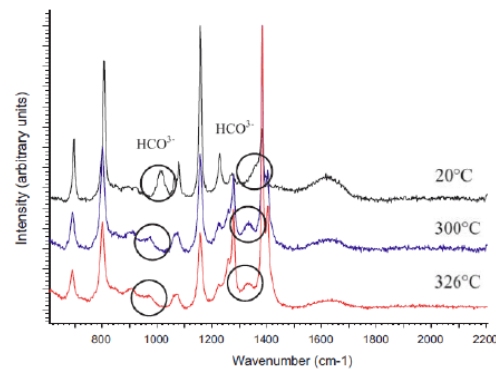receive the relative concentration of HCO_3^- in the aqueous solution.

Fig. 1. Example spectra of bicarbonate-rich aqueous phase present in H_2O-CO_2 fluid inclusions at variable temperatures. Two major areas used for HCO_3^- identification and quantification are highlighted. Note the Raman peak shift with temperature.

For the low temperature measurements the peak area ratio:

RC_{HCO3}=A_{1014}(HCO_3^-)/((A_{1640}(H_2O)-A_{1620} (Quartz)) formula was suggested as the most practical while the peak height ratio (RC_{HCO3}=I_{1360}(HCO_3^-)/((I_{1640}(H_2O)-I_{1620} (Quartz))) seems more applicable for temperatures above 100°C. The behavior of quartz matrix and the possibility of spectral subtraction of quartz from solution spectra were tested to overcome the peak overlap of quartz and CO_3^{2-} at around 1066 cm^{-1}. Based on our results, the Libcice paleofluids were estimated to pH 7 - 8.5. The extremely high variation in relative peak intensity of the monitored part of quartz spectrum was confirmed even within

a single grain. Other peak parameters were tested to establish the best potential calibration strategies for quantitative Raman measurement of bicarbonate in natural fluid inclusions both at room and at elevated temperatures. This research is important for the future pH calculation development and high temperature Raman spectroscopic study of fluid inclusions/paleofluids.

Acknowledgement
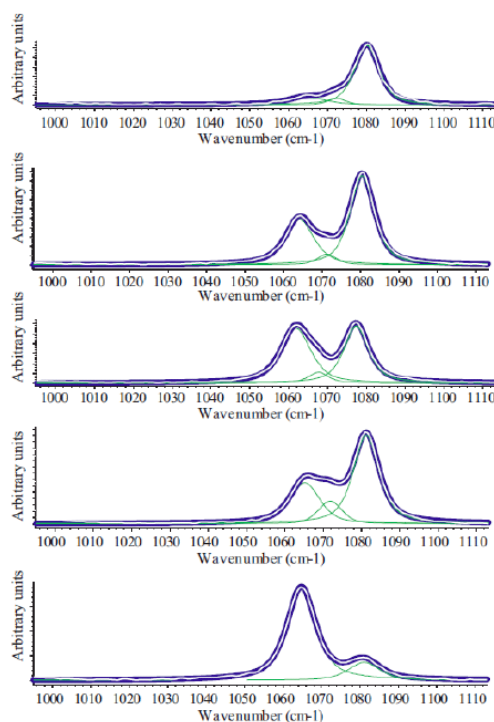
Fig. 2. Example Raman spectra of the quartz matrix showing variation in the region of interest for CO_3^{2-} quantification and potential pH calculation of paleofluids. Note the presence of variable matrix peak intensities in the area of 1064 cm^{-1} which is also an area of major CO_3^{2-} peak.

REFERENCES

Hrstka T., Dubessy J., Zacharias J. (2011): Bicarbonate-rich fluid inclusions and hydrogen diffusion in quartz from the Libčice orogenic gold deposit, Bohemian Massif, Chemical Geology-Volume 281, Issues 3-4, 24 February 2011, Pages 317-332

Dubessy J., Poty B., Ramboz C., 1989. Advances in C-O-H-N-S fluid geochemistry based on micro-Raman spectrometric analysis of fluid inclusions. Europian Journal of Mineralogy 1, pp. 517-534.

Dubessy, J., Ding, J., Leisen, M. and Robert, P., 2008. Towards pH estimation of paleofluid circulation combining Raman analysis of CO_2/HCO_3^- bearing fluid inclusions and thermodynamic modelling below 523 K. PACROFI, (IX th) USGS, Reston, USA.

Zachariáš, J., 2002. Interpretation of bidimensional fluid inclusion microthermometric data in terms of pressure and compositional variations in gold-bearing fluids: An example from the Libcice and Kasejovice deposits, Czech Republic, Journal of the Czech Geological Society, volume 47, issue 3-4,123 – 132

2

Appendix A.2 Bicarbonate-rich Fluid Inclusions and Hydrogen Diffusion in Quartz Gangue from the Libčice Orogenic Gold Deposit, Bohemian Massif

Presented at: ECROFI 2011 (European Current Research on Fluid Inclusions (ECROFI-XXI), Montanuniversität Leoben, Austria, 9-11 August, 2011).

Zachariáš J., Hrstka T., Dubessy J. (2011): Bicarbonate-rich fluid inclusions and hydrogen diffusion in quartz gangue from the Libčice orogenic gold deposit, Bohemian Massif, European Current Research on Fluid Inclusions (ECROFI-XXI), Montanuniversität Leoben, Austria, 9-11 August, 2011. Abstract Volume, p. 208

Bicarbonate-rich fluid inclusions and hydrogen diffusion in quartz gangue from the Libcice orogenic gold deposit, Bohemian Massif

Zacharias, Jiri*, Hrstka, Tomas* and Dubessy, Jean**

*Institute of Geochemistry, Mineralogy and Mineral Resources, Faculty of Science, Charles University in Prague, Albertov 6, Prague, Czech Republic
**G2R(UMR 7566), Faculté des Sciences, Université Henri Poincaré-Nancy Université, Vandoeuvre-les-Nancy Cedex, France

Unusual paleofluid composition is reported for the Libčice orogenic-type gold deposit located in a contact zone of the Central Bohemian Plutonic Complex, Czech Republic. Unexpected bicarbonate-rich fluids and their complex chemistry variations characterize primary fluid inclusions from the main gold-bearing quartz vein. A detailed microthermometry, Laser Raman Micro Spectroscopy and SEM cathodoluminescence study was used in order to decipher fluid history. The results (Zacharias, 2002; Hrstka et al., 2011) indicate the presence of H_2O and $H_2O– CO_2–CH_4$ ($\pm N_2$; H_2S) fluids, the latter displaying variations of the CO_2/CH_4 ratio in the gaseous phase from 6.8 to 0.06. Variation of the CH_4 content across single grains and between different levels of the mine was recorded. The presence of nahcolite, H_2 (up to 6 mole%) and ethane (0–0.2 mole%) in the fluids were also discovered by Raman probe. Potential models for the formation of different types of fluids present in the deposit are discussed, including the genesis of HCO_3^- rich fluids as well as H_2 and C_2H_6 presence in the primary fluid inclusions. The potential influence of organic matter-bearing sediments, as well as the impact of the intrusion of CBPC, re-equilibration and/or re-speciation of fluid inclusions during the post-entrapment history is considered to have the main impact on the complex paleofluid chemistry. Based on the thermodynamic modelling, H_2 diffusion into the fluid inclusions was shown to be the main reason for the CH_4 variation on the scale of a single grain, as well as across the whole vein. Although the exact processes of production/formation of HCO_3^- and H_2 at the Libčice deposit remain open to discussion, reactions in the C–O–H system are considered to be a possible formation mechanism.

This work also contributes to our understanding of the importance of post-entrapment modifications and reactions in the C–O–H system on interpretation/ deciphering the processes in orogenic-type deposits.

REFERENCES

Zacharias J. (2002): J. Czech Geol. Society, 47: 123-132.

Hrstka T., Dubessy J., Zacharias J. (2011): *Chem. Geol.* 281: 313-332.

Appendix A.3 Applications of Confocal Microscopy in Geosciences

Presented at: MDSG 2006 (The 29th Annual Winter Conference of the Mineral Deposits Studies Group, London (UK), 2006).

Applications of confocal microscopy in geosciences

Presenting Author: Tomas Hrstka

Affiliations
Charles University in Prague, Faculty of Science Institute of Geochemistry, Mineralogy and Mineral Resources,
Albertov 6, Prague 2, CZ-128 43, hrstka@natur.cuni.cz
Current address: Natural History Museum, Department of Mineralogy, Cromwell Road, London SW7 5BD, UK

Confocal laser scanning microscopy CLSM is a microscopic technique providing 3D or 4D visualization of microscopic samples specimens on an um scale by alignment of 2D confocal sections in computer. In spite of the fact that CLSM techniques are nowadays almost routine in biology and medicine, until now there have not been many articles presented on the use of this method in geosciences. This presentation shows examples of use of CLSM in our lab on specific topics and also reviews some applications of CLSM for geosciences in general. The details of instrumentation, methodology, suitable software and the main advantages of this technique and its limitations are also presented.

Applications for CLSM: a) Fluid inclusion 3D analysis, visualization and location[1,7,4] ; b) Rock porosity and crack network connectivity measurements [3,6] ; c) Fission tracks mapping [5], d) Crystal defect study [5], and e) Palaeontological 3D reconstructions [2]. Our attempt was to test the CLSM reflected mode confocal scanning for the visualization of non-fluorescent fluid inclusions, visualization of their 3D geometry, volume calculation and FIA space relationships mapping. Due to the fact that these tests were not very successful we also used SKY SCAN NanoTomograph and the first preliminary data for this X-ray non-destructive method are also presented. This method was tested in order to potentially provide exact fill ratios for complex aqueous and aqueous-carbonic gas bearing non-fluorescent fluid inclusions. The comparison between this technique and CLSM technique results is discussed.

A new method of visualization and measurements of 3D laser ablation craters, their shape and volumes is presented as well. This includes both reflected mode scanning and classical fluorescence CLSM carried by the infilling of the LA craters by fluorescent fill prior to analysis. Such measurements can provide calculation of ablated mass and crater shape development for different materials and ablation parameters. All these information could be used to improve the methodology for quantitative multi-element analysis of single fluid inclusions.

References:
1. C. Aplin, G. Macleod, S. R. Larter, K. S. Pedersen, H. Sorensen, and T. Booth ; Combined use of confocal laser scanning microscopy and PVT simulation for estimating the composition and physical properties of petroleum in fluid inclusions; Marine and Petroleum Geology (March 1999), 16(2):97-110
2. Harry Birkmann and Robert F. Lundin; Confocal microscopy; potential applications in micropaleontology; Journal of Paleontology, (Nov 1996); 70: 1084 - 1087.
3. J. T. Fredrich ; 3D imaging of porous media using laser scanning confocal microscopy with application to microscale transport processes (in Imaging, analysing and modelling pore structure in geomaterials); Physics and Chemistry of the Earth. Part A: Solid Earth and Geodesy (1999), 24(7):551-561

4. Joerg O. W. Grimmer, Jacques Pironon, Stephane Teinturier, and Jerome Mutterer; Recognition and differentiation of gas condensates and other oil types using microthermometry of petroleum inclusions (in Proceedings of Geofluids IV); Journal of Geochemical Exploration (May 2003), 78-79(2003):367-371

5. N. Petford and J. A. Miller; Three-dimensional imaging of fission tracks using confocal scanning laser microscopy; American Mineralogist, (Jun 1992); 77: 529 - 533.

6. N. Petford, G. Davidson, and J. A. Miller ; Investigation of the petrophysical properties of a porous sandstone sample using confocal scanning laser microscopy;Petroleum Geoscience (May 2001), 7(2):99-105

7. Jacques Pironon, Martin Canals, Jean Dubessy, Frederic Walgenwitz, and Corinne Laplace-Builhe: Volumetric reconstruction of individual oil inclusions by confocal scanning laser microscopy (in ECROFI XIV (European Current Research on Fluid Inclusions) symposium) European Journal of Mineralogy (December 1998), 10(6):1143-1150

Appendix A.4 Paleofluid Chemistry and Mineralogical Variation of Orogenic Gold Deposits in the Bohemian Massif

Presented at: Fermor Meeting of the Geological Society: Minerals, Magmas and Megastructures, London Natural History Museum, 13-15.09. London (United Kingdom), 2006

Paleofluid chemistry and mineralogical variation of Orogenic gold deposits in the Bohemian Massif

TOMAS HRSTKA[1], J. ZACHARIÁŠ[1], M. MIHALJEVIC[1], R. HERRINGTON[2], J. WILLKINSON[3]
[1]Charles University in Prague, Faculty of Science Institute of Geochemistry, Mineralogy and Mineral Resources, Albertov 6, Prague 2, CZ-128 43, hrstka@natur.cuni.cz
[2]Natural History Museum, Department of Mineralogy, Cromwell Road, London, SW7 5BD, UK [3]Department of Earth Science & Engineering Imperial College London, SW7 2AZ, UK

Orogenic gold mineralizations are a typical feature of the metallogeny of Variscan Europe. Numerous examples are known from the Bohemian Massif (BM) Czech Republic, the Massif Central and the Armorican Massif in France and the Iberian Massif in Spain/Portugal (Boiron et al., 2001; Morávek et al., 1995; Zachariáš et al., 2001and Zachariáš et al., in prep). Based on mineralogical criteria the orogenic style gold deposits in the BM could be distinguished to:

1.High fineness Au deposits with W-Mo-Bi-Te-S phases (Mokrsko, Kašperské Hory, Kasejovice)

2.High fineness Au-Sb deposits (Krásná Hora)

3.Low fineness Au (electrum) deposits without W-Mo-Bi-Te-S-Sb phases (Roudný, Dobrá Voda)

Mineralogy and paleofluid chemistry inferred from complex microthemometry, Raman analysis, LA-ICP-MS individual inclusion analysis and classical mineralogical study is presented here for the Kasejovice (high fineness Au) and Roudný (low fineness Au) deposits.

Main ore minerals at Roudný deposit include pyrite, arsenopyrite. Gold is 658-665 fine. Three main mineralization stages were distinguished with two different types of fluids: low salinity H_2O-$CO_2 \pm CH_4 \pm N_2$ (2-4wt.% NaCl eq.) and moderate-salinity H_2O-only fluids (7-9wt% NaCl eq). The aqueous-carbonic fluids represent the barren pre-ore stage and beginning of the main ore stage as well. The majority of the ore stage, however, precipitated from aqueous fluid at around 250 to 350°C. Both fluids representing the main and the late ore stages show no significant differences in cation ratios and LA-ICP-MS detected elements (Li, Na, Mg, K, Ca, Mn, As, Rb, Sr, Ba).

For the Kasejovice deposit pyrrhotine and arsenopyrite represent major ore minerals and gold (900-950) is frequently associated with W-Mo-Bi-Te-S phases. Both $H_2O-CO_2\pm CH_4\pm N_2$ low salinity (2,5wt% NaCl eq.) and H_2O low to moderate salinity fluids were recognized. The salinity of aqueous fluids increases from ~2 wt% to ~8wt% NaCl eq. towards the late mineralization stage. Entrapment from heterogeneous fluid is proposed for the late aqueous fluids at temperatures around 150-200°C. The proposed temperatures for the main ore stage are about 280 to 350°C. The LA-ICP-MS inclusion analysis revealed presence of Li, Na, Mg, K, Ca, Mn, Rb, Sr and Ba in both fluid types.

As we can see some fundamental differences in the mineralogy of the low and high fineness orogenic style deposits within the BM, the differences are less discernible with respect to cation fluid chemistry, fluid types and formation temperatures. The role of complex $H_2O-CO_2\pm CH_4\pm N_2$ fluids was probably more important at the high fineness group of deposits than at the low fineness one.

Boiron, M.C., Barakat, A., Cathelineau, M., Banks, D.A., Ďurisova, J., and Morávek, P., 2001, Geometry and P-V-T-X conditions of microfissural ore fluid migration: the Mokrsko gold deposit (Bohemia): Chemical Geology, v. 173, p. 207–225

Morávek, P., 1995a, Gold deposits of the Central and SW part of the Bohemian Massif: Third Biennial SGA Meeting (August 28-31, 1995, Prague, Czech Republic) – Excursion Guide, Prague, Czech Geological Survey, p. 1–17.

Zachariáš, J., Pertold, Z., Pudilova, M., Žak, K., Pertoldova, J., Stein, H., and Markey, R., 2001a, Geology and genesis of Variscan porphyry-style gold mineralization, Petrackova hora deposit, Bohemian Massif, Czech Republic: Mineralium Deposita, v. 36, p. 517–541